

AD-A250 989



DTIC
S ELECTE D
JUN 1 1992
C



**The Influence of a Free Surface on the Development
of Turbulence in a Submerged Jet**

Douglas G. Anthony
Department of Aerospace Engineering

Contract Number N00014-86-K-0684
Technical Report No. 90-2

October, 1990

DISTRIBUTION STATEMENT A

Approved for public release;
Distribution Unlimited

92 5 26 019

92-13793



**THE INFLUENCE OF A FREE SURFACE ON THE DEVELOPMENT
OF TURBULENCE IN A SUBMERGED JET**

by

Douglas G. Anthony

A dissertation submitted in partial fulfillment
of the requirements for the degree of
Doctor of Philosophy
(Aerospace Engineering)
in The University of Michigan
1990

Doctoral Committee:

Professor William W. Willmarth, Chair
Professor Robert F. Beck
Associate Professor Luis P. Bernal
Assistant Professor David T. Walker

Statement A per telecon
Dr. Edwin Rood ONR/Code 1132
Arlington, VA 22217-5000

NWW 6/1/92

Accession For	
NTIS GRA&I	<input checked="checked" type="checkbox"/>
DTIC TAB	<input type="checkbox"/>
Unannounced	<input type="checkbox"/>
Justification	
By	
Distribution/	
Availability Codes	
Dist	Avail and/or Special
A-1	

ABSTRACT

THE INFLUENCE OF A FREE SURFACE ON THE DEVELOPMENT OF TURBULENCE IN A SUBMERGED JET

by

Douglas G. Anthony

Chair: William W. Willmarth

Radar images of the ocean surface made when surface ships are moving within the imaged area reveal distinctive surface signatures attributed to the interaction of the turbulent wake of the ship with the free surface. In order to study the behavior of turbulence near a free surface, the flow in a round, turbulent jet issuing beneath and parallel to a clean free surface was investigated experimentally. A three-component Laser Doppler Velocimeter (LDV) was used to make detailed measurements of the mean flow velocity and Reynolds stress tensor throughout the flowfield. Surface shadowgraphs and Laser Induced Fluorescence (LIF) were used to visualize features of the free surface deformations and the subsurface flowfield.

The jet Reynolds number, $U_j d/\nu=12,700$, and Froude number, $U_j/(gh)^{1/2}=5.66$, were comparable to those of the jet flow investigation of Bernal and Madnia, 1988. Large-scale turbulent structures within the jet generated surface waves that were

observed to propagate nearly perpendicular to the jet axis. Measurements of the wavelength and wave speed from shadowgraph images showed these waves to be gravity-capillary waves.

The LDV measurements revealed that near the jet centerline, the RMS velocity fluctuations become anisotropic as the free surface is approached: The fluctuations normal to the surface are diminished, while those parallel to the surface are enhanced. Measurements made near the surface on either side of the jet revealed the existence of a shallow surface current much wider than the primary jet flow. Within this current, the magnitudes of the cross-stream and vertical RMS velocity fluctuations are approximately the same, but are greater than that of the streamwise fluctuations. This is attributed to motions arising from surface waves propagating perpendicular to the jet axis and superposed on the surface current.

LIF images of the surface current show it to consist largely of fluid emitted from the jet. Beneath a clean free surface, these emissions propagate to considerable distance under the influence of their images above the surface. When a surfactant is placed on to the water surface, vortical fluid ejected from the jet interacts with secondary vorticity generated beneath the surfactant covered surface, and the surface current is suppressed.

For my Father, who insists that all projects undertaken be
carried out as if, once finished, they are required to fly.

ACKNOWLEDGMENTS

I wish to acknowledge first the financial support of the David Taylor Research Center, initially through their Extended-Term Training Program, which allowed me to complete the required coursework and preliminary examinations in a timely manner, and later through the ONR-sponsored Surface Ship Wake Consortium, which kept me afloat at Michigan during the course of this investigation.

I do not know how to acknowledge properly the considerable efforts and many hours of work of my advisor, Prof. William W. Willmarth, both in the design of the LDV and in time spent actually in the laboratory. His insistence that an understanding of complex physical phenomena is not gained until the details of each contributing part are first fully understood taught me a valuable lesson that I learned only slowly. For his patience, too, I am deeply grateful.

I wish to thank the other members of my thesis committee, Profs. Robert F. Beck, Luis P. Bernal, and David T. Walker, for their critical review of this work and for their many helpful suggestions, corrections, and clarifications.

I wish to acknowledge and thank Amir Hirsu for his help, especially with the flow visualizations performed in the later stages of this investigation.

And to my family and many friends, who offered me both encouragement and criticism when I most needed them, I wish to say thanks.

TABLE OF CONTENTS

DEDICATION	ii
ACKNOWLEDGMENTS	iii
LIST OF FIGURES	vi
NOMENCLATURE	xiii
CHAPTER	
I. INTRODUCTION	1
II. EXPERIMENTAL APPARATUS	5
2.1 Laser Doppler Velocimeter	5
2.2 Experimental Facility and Jet Nozzle Design	9
2.3 Signal Processing	11
2.4 Software	12
III. EXPERIMENTAL PROCEDURES	13
3.1 LDV Alignment	13
3.2 LDV Calibration	14
3.3 Coordinate Conventions	18
3.4 Jet Alignment	18
3.5 Seeding and Surface Contamination	19
3.6 Data Acquisition	21
3.7 Data Reduction and Bias Correction	24
3.8 Flow Visualization	25
IV. RESULTS AND DISCUSSION	27
4.1 Deep Jet Measurements	27
4.2 Shallow Jet Measurements	30
4.3 Surface Current Measurements	36
4.4 Flow Visualization	45
V. CONCLUSIONS	49

APPENDIX	52
REFERENCES	56
FIGURES	60

LIST OF FIGURES

Figure	Caption	Page
1.1.	Schematic of the jet and image model of Bernal and Madnia, 1988, for the free surface jet. The jet depth is h , and the exit momentum flux is J_0 . U_m denotes the maximum streamwise mean velocity in the profile.	61
1.2.	Schematic of the flow geometry. The coordinate x is defined as positive downstream, and z is defined as positive toward the free surface. The remaining coordinate, y , is defined so as to give a right-handed system.	62
2.1.	Plan and side views of the LDV probe and jet nozzle. The LDV rotates about its axis and translates perpendicular to the jet; the jet translates on its axis.	63
2.2.	Schematic of the single-component underwater LDV module, showing the transmitting and receiving optics.	64
2.3.	Schematic of the towing tank, LDV probe, and jet nozzle.	65
2.4.	Schematic of the flow loop, showing both the jet circuit and the filter circuit.	66
2.5.	Schematic of the jet nozzle and settling chamber. The nozzle profile is a fifth-degree polynomial, having specified diameter and both zero slope and curvature at entry and exit.	67
4.1.	Variation of streamwise mean velocity U_c on jet centerline for the deep jet, $h/d=50$. Open symbols are data of the present investigation; solid symbols are data of Wagnanski and Fiedler, 1969.	68
4.2.	Variation of RMS velocity fluctuations on jet centerline for the deep jet, $h/d=50$. Open symbols are data of the present investigation; solid symbols are data of Wagnanski and Fiedler, 1969.	69

4.3a.	Horizontal profiles of the streamwise mean velocity U/U_c for the deep jet, $h/d=50$, $z/d=0$. Solid curve is the theoretical solution of Tollmien.	70
4.3b.	Horizontal profiles of the horizontal mean velocity V/U_c for the deep jet, $h/d=50$, $z/d=0$.	71
4.3c.	Horizontal profiles of the vertical mean velocity W/U_c for the deep jet, $h/d=50$, $z/d=0$.	72
4.3d.	Horizontal profiles of the streamwise RMS velocity fluctuations u'/U_c for the deep jet, $h/d=50$, $z/d=0$.	73
4.3e.	Horizontal profiles of the horizontal RMS velocity fluctuations v'/U_c for the deep jet, $h/d=50$, $z/d=0$.	74
4.3f.	Horizontal profiles of the vertical RMS velocity fluctuations w'/U_c for the deep jet, $h/d=50$, $z/d=0$.	75
4.3g.	Horizontal profiles of the Reynolds stress \overline{uv}/U_c^2 for the deep jet, $h/d=50$, $z/d=0$.	76
4.3h.	Horizontal profiles of the Reynolds stress \overline{vw}/U_c^2 for the deep jet, $h/d=50$, $z/d=0$.	77
4.3i.	Horizontal profiles of the Reynolds stress \overline{uw}/U_c^2 for the deep jet, $h/d=50$, $z/d=0$.	78
4.4a.	Vertical profiles of the streamwise mean velocity U/U_c for the deep jet, $h/d=50$, $y/d=0$. Solid curve is the theoretical solution of Tollmien.	79
4.4b.	Vertical profiles of the horizontal mean velocity V/U_c for the deep jet, $h/d=50$, $y/d=0$.	80
4.4c.	Vertical profiles of the vertical mean velocity W/U_c for the deep jet, $h/d=50$, $y/d=0$.	81
4.4d.	Vertical profiles of the streamwise RMS velocity fluctuations u'/U_c for the deep jet, $h/d=50$, $y/d=0$.	82
4.4e.	Vertical profiles of the horizontal RMS velocity fluctuations v'/U_c for the deep jet, $h/d=50$, $y/d=0$.	83
4.4f.	Vertical profiles of the vertical RMS velocity fluctuations w'/U_c	84

for the deep jet, $h/d=50$, $y/d=0$.

4.4g.	Vertical profiles of the Reynolds stress \overline{uv}/U_c^2 for the deep jet, $h/d=50$, $y/d=0$.	85
4.4h.	Vertical profiles of the Reynolds stress \overline{vw}/U_c^2 for the deep jet, $h/d=50$, $y/d=0$.	86
4.4i.	Vertical profiles of the Reynolds stress \overline{uw}/U_c^2 for the deep jet, $h/d=50$, $y/d=0$.	87
4.5a.	Vertical profile of the streamwise mean velocity at $x/d=32$ for the deep jet, $h/d=50$, $y/d=0$. Solid curve is the theoretical solution of Tollmien.	88
4.5b.	Vertical profiles of the horizontal and vertical mean velocities at $x/d=32$ for the deep jet, $h/d=50$, $y/d=0$.	89
4.5c.	Vertical profiles of the RMS velocity fluctuations at $x/d=32$ for the deep jet, $h/d=50$, $y/d=0$.	90
4.5d.	Vertical profiles of the Reynolds stresses at $x/d=32$ for the deep jet, $h/d=50$, $y/d=0$.	91
4.6a.	Vertical profile of the streamwise mean velocity at $x/d=16$ for the shallow jet, $h/d=2$, $y/d=0$. Solid curve is the theoretical free jet solution of Tollmien.	92
4.6b.	Vertical profiles of the horizontal and vertical mean velocities at $x/d=16$ for the shallow jet, $h/d=2$, $y/d=0$.	93
4.6c.	Vertical profiles of the RMS velocity fluctuations at $x/d=16$ for the shallow jet, $h/d=2$, $y/d=0$.	94
4.6d.	Vertical profiles of the Reynolds stresses at $x/d=16$ for the shallow jet, $h/d=2$, $y/d=0$.	95
4.7a.	Vertical profile of the streamwise mean velocity at $x/d=32$ for the shallow jet, $h/d=2$, $y/d=0$. Solid curve is the theoretical free jet solution of Tollmien.	96
4.7b.	Vertical profiles of the horizontal and vertical mean velocities at $x/d=32$ for the shallow jet, $h/d=2$, $y/d=0$.	97
4.7c.	Vertical profiles of the RMS velocity fluctuations at $x/d=32$ for	98

the shallow jet, $h/d=2$, $y/d=0$.

4.7d.	Vertical profiles of the Reynolds stresses at $x/d=32$ for the shallow jet, $h/d=2$, $y/d=0$.	99
4.8a.	Vertical profile of the streamwise mean velocity above the jet centerline at $x/d=32$ for the shallow jet, $h/d=2$, $y/d=0$.	100
4.8b.	Vertical profiles of the horizontal and vertical mean velocities above the jet centerline at $x/d=32$ for the shallow jet, $h/d=2$, $y/d=0$.	101
4.8c.	Vertical profiles of the RMS velocity fluctuations above the jet centerline at $x/d=32$ for the shallow jet, $h/d=2$, $y/d=0$.	102
4.8d.	Vertical profiles of the Reynolds stresses above the jet centerline at $x/d=32$ for the shallow jet, $h/d=2$, $y/d=0$.	103
4.9a.	Horizontal profiles of the streamwise mean velocity U/U_c at $x/d=32$ for the shallow jet, $h/d=2$.	104
4.9b.	Horizontal profiles of the horizontal mean velocity V/U_c at $x/d=32$ for the shallow jet, $h/d=2$.	105
4.9c.	Horizontal profiles of the vertical mean velocity W/U_c at $x/d=32$ for the shallow jet, $h/d=2$.	106
4.9d.	Horizontal profiles of the streamwise RMS velocity fluctuations u'/U_c at $x/d=32$ for the shallow jet, $h/d=2$.	107
4.9e.	Horizontal profiles of the horizontal RMS velocity fluctuations v'/U_c at $x/d=32$ for the shallow jet, $h/d=2$.	108
4.9f.	Horizontal profiles of the vertical RMS velocity fluctuations w'/U_c at $x/d=32$ for the shallow jet, $h/d=2$.	109
4.9g.	Horizontal profiles of the Reynolds stress \overline{uv}/U_c^2 at $x/d=32$ for the shallow jet, $h/d=2$.	110
4.9h.	Horizontal profiles of the Reynolds stress \overline{vw}/U_c^2 at $x/d=32$ for the shallow jet, $h/d=2$.	111
4.9i.	Horizontal profiles of the Reynolds stress \overline{uw}/U_c^2 at $x/d=32$ for the shallow jet, $h/d=2$.	112

4.10	Shadowgraph and sketch showing surface deformations above the shallow jet, $h/d=2$, beneath a clean free surface. The inset on the left is a shadowgraph, inverted so as to show the crests of waves as dark rather than light. The sketch indicates a region of intense jet/free-surface interaction with higher amplitude but rather incoherent waves being generated near the jet centerline. These waves are observed to coalesce into more coherent, smaller amplitude waves propagating away from the jet centerline. The wavelength and wave speed of these waves are observed from video images to be approximately 1 to 4 cm and 25 cm/s, respectively. Also indicated are the closely spaced hair-like disturbances which are observed in the video images but were not resolved in the inset shadowgraph.	113
4.11a.	Horizontal profiles of the streamwise mean velocity U/U_c at $x/d=24$ for the shallow jet, $h/d=2$.	114
4.11b.	Horizontal profiles of the horizontal mean velocity V/U_c at $x/d=24$ for the shallow jet, $h/d=2$.	115
4.11c.	Horizontal profiles of the vertical mean velocity W/U_c at $x/d=24$ for the shallow jet, $h/d=2$.	116
4.11d.	Horizontal profiles of the streamwise RMS velocity fluctuations u'/U_c at $x/d=24$ for the shallow jet, $h/d=2$.	117
4.11e.	Horizontal profiles of the horizontal RMS velocity fluctuations v'/U_c at $x/d=24$ for the shallow jet, $h/d=2$.	118
4.11f.	Horizontal profiles of the vertical RMS velocity fluctuations w'/U_c at $x/d=24$ for the shallow jet, $h/d=2$.	119
4.11g.	Horizontal profiles of the Reynolds stress \overline{uv}/U_c^2 at $x/d=24$ for the shallow jet, $h/d=2$.	120
4.11h.	Horizontal profiles of the Reynolds stress \overline{vw}/U_c^2 at $x/d=24$ for the shallow jet, $h/d=2$.	121
4.11i.	Horizontal profiles of the Reynolds stress \overline{uw}/U_c^2 at $x/d=24$ for the shallow jet, $h/d=2$.	122
4.12a.	Horizontal profiles of the streamwise mean velocity U/U_c at $x/d=16$ for the shallow jet, $h/d=2$.	123
4.12b.	Horizontal profiles of the horizontal mean velocity V/U_c at	124

$x/d=16$ for the shallow jet, $h/d=2$.	
4.12c. Horizontal profiles of the vertical mean velocity W/U_c at $x/d=16$ for the shallow jet, $h/d=2$.	125
4.12d. Horizontal profiles of the streamwise RMS velocity fluctuations u'/U_c at $x/d=16$ for the shallow jet, $h/d=2$.	126
4.12e. Horizontal profiles of the horizontal RMS velocity fluctuations v'/U_c at $x/d=16$ for the shallow jet, $h/d=2$.	127
4.12f. Horizontal profiles of the vertical RMS velocity fluctuations w'/U_c at $x/d=16$ for the shallow jet, $h/d=2$.	128
4.12g. Horizontal profiles of the Reynolds stress \overline{uv}/U_c^2 at $x/d=16$ for the shallow jet, $h/d=2$.	129
4.12h. Horizontal profiles of the Reynolds stress \overline{vw}/U_c^2 at $x/d=16$ for the shallow jet, $h/d=2$.	130
4.12i. Horizontal profiles of the Reynolds stress \overline{uw}/U_c^2 at $x/d=16$ for the shallow jet, $h/d=2$.	131
4.13a. Contours of the streamwise mean velocity U/U_c at $x/d=16$ for the shallow jet, $h/d=2$.	132
4.13b. Contours of the streamwise mean velocity U/U_c at $x/d=24$ for the shallow jet, $h/d=2$.	133
4.13c. Contours of the streamwise mean velocity U/U_c at $x/d=32$ for the shallow jet, $h/d=2$.	134
4.13d. Contours of the streamwise mean velocity U/U_c at $x/d=48$ for the shallow jet, $h/d=2$.	135
4.13e. Contours of the streamwise mean velocity U/U_c at $x/d=64$ for the shallow jet, $h/d=2$.	136
4.14a. Vector plot of the horizontal and vertical mean velocities at $x/d=16$ for the shallow jet, $h/d=2$.	137
4.14b. Vector plot of the horizontal and vertical mean velocities at $x/d=24$ for the shallow jet, $h/d=2$.	138
4.14c. Vector plot of the horizontal and vertical mean velocities at	139

$x/d=32$ for the shallow jet, $h/d=2$.	
4.14d. Vector plot of the horizontal and vertical mean velocities at $x/d=48$ for the shallow jet, $h/d=2$.	140
4.14e. Vector plot of the horizontal and vertical mean velocities at $x/d=64$ for the shallow jet, $h/d=2$.	141
4.15a. LIF photographs of the shallow jet, $h/d=2$, issuing beneath a clean free surface. The laser light sheet was positioned in a vertical plane at $x/d=32$. Exposure times are 1/125 s (top) and 1/2 s (bottom).	142
4.15b. LIF photographs of the shallow jet, $h/d=2$, issuing beneath a free surface contaminated with oleyl alcohol. The laser light sheet was positioned in a vertical plane at $x/d=32$. Exposure times are 1/125 s (top) and 1/2 s (bottom).	143
4.16a. LIF photograph of the surface current produced by the shallow jet, $h/d=2$. The laser light sheet was positioned in a horizontal plane approximately .3 cm below the free surface.	144
4.16b. LIF photograph of the surface current produced by the shallow jet, $h/d=2$. The laser light sheet was positioned in a horizontal plane through the jet centerline.	145
A.1. Sketch showing transformation of velocity components between optical and probe coordinate systems.	146
A.2. Sketch showing coordinate rotation between probe and jet coordinate systems.	147

NOMENCLATURE

Symbol	Meaning
x	Streamwise coordinate, positive downstream
y	Horizontal coordinate, positive for right-handed system
z	Vertical coordinate, positive upwards
U	Streamwise mean velocity component
V	Horizontal mean velocity component
W	Vertical mean velocity component
u'	Streamwise RMS velocity fluctuation
v'	Horizontal RMS velocity fluctuation
w'	Vertical RMS velocity fluctuation
\overline{uv}	Reynolds stress component
\overline{uw}	Reynolds stress component
\overline{vw}	Reynolds stress component
d	Jet diameter
f	Frequency
g	Acceleration of gravity
h	Jet depth
R	Probe standoff radius
α	Angle between optical axis and LDV perpendicular
ζ	Wave amplitude
κ	Included angle between laser beam pair
λ	Wavelength
θ	Probe lookup angle
ν	Kinematic viscosity of water
ω	Angular frequency
Re	Reynolds number
Fr	Froude number
b	(subscript) Blue
g	(subscript) Green
v	(subscript) Violet
c	(subscript) Centerline
e	(subscript) Exit
m	(subscript) Maximum
D	(subscript) Doppler

CHAPTER I

INTRODUCTION

The behavior of turbulence near a free surface is of considerable interest to the remote detection of the wakes of surface ships. Synthetic Aperture Radar (SAR) images of the ocean surface taken when surface ships are moving within the imaged area reveal distinctive wake phenomena attributed both to surface waves generated by the ship and to turbulent wakes shed from the hull and propulsors. Certain aspects of the Kelvin wave wake system are sometimes visible in SAR images, but observations of ship wakes from space do not generally show the classical pattern. Under quiet wind conditions, the wake appears as a bright, narrow 'V' of half-angle typically around 3 degrees. An analysis of the SAR images shows that the Kelvin wake components cannot correctly account for the observed narrow 'V' and suggests that SAR is actually sensing short-wavelength, ship generated surface waves, as if produced by a sequence of incoherent point sources (Munk, *et al.*, 1987). Turbulent wake phenomena are characterized in their SAR images by a dark, narrow band along the ship track, persisting for tens of kilometers behind the ship. The dark band is attributed to the absence of a radar return in a region of interaction between turbulent surface currents and ambient waves (Lyden, *et al.*, 1988).

These wake phenomena raise fundamental questions as to the nature of turbulent flows near a free boundary and illustrate the complex nature of interactions

among turbulence, surface waves, and surface currents. The present study investigates the behavior of a submerged turbulent jet issuing beneath a free surface in aid of understanding the fundamental hydrodynamic mechanisms that govern these interactions.

A three-component underwater Laser Doppler Velocimeter (LDV) was designed for obtaining measurements in the wakes of ship models in a towing tank (Willmarth, 1987). The LDV allows non-intrusive measurements of the flow velocity very near the free surface, and by requiring simultaneity among measurements on all three components allows determination of turbulence quantities, including all components of the Reynolds stress tensor, throughout the flowfield.

There is considerable literature devoted to the characteristics of axisymmetric, turbulent free jets; Abramovich, 1963 and Rajaratnam, 1976 offer comprehensive reviews. A thin-layer approximation to the governing equations admits a similarity scaling applicable in the far-field of the free jet, and extensive measurements in this self-similar or self-preserving region have been reported by Wygnanski and Fiedler, 1969. Their measurements show that the axisymmetric jet achieves a self-similar mean velocity profile in as few as 20 diameters downstream, but that it becomes fully self-similar in its turbulence quantities only beyond about 80 diameters downstream. Near-field measurements in a free axisymmetric jet document the role of large scale structures on the development of the jet (e.g. Browand and Laufer, 1975), and more recent measurements suggest that even the far-field is dominated by such structures (Dimotakis, *et al.*, 1983).

Investigations of turbulent jet flows near free surfaces, until recently, have been

concerned primarily with flows of relevance to civil and hydraulic engineering, e.g. fluid discharges into lakes and streams, where the effects of buoyancy are often significant. Rajaratnam and Humphries, 1984, investigated turbulent non-buoyant surface jets, and Rajaratnam and Subramanyan, 1985, investigated planar buoyant surface jets to determine the scaling behavior of the mean flowfields.

An experimental investigation of the interaction of a circular turbulent jet and a free surface was reported by Bernal and Madnia, 1988 (see also Madnia, 1989; Anthony, *et al.*, 1990). Mean flow and turbulence measurements were made beneath the free surface using a hot-film anemometer, and a simple model was shown to describe correctly the scaling of the mean flowfield. This simple model considers the flowfield of a jet issuing beneath a free surface as equivalent to that of a jet issuing beneath an identical image jet, the free surface being regarded as a plane of symmetry for sufficiently low Froude numbers (Figure 1.1). Three regions can be identified, the scaling behavior of each determined from the ratio of downstream distance to jet depth: A deep jet region, a surface jet region, and an interaction region in which the jet depth h is the dominant length scale. The researchers showed that the surface jet scales like the deep jet, but with twice the momentum flux to account for the effect of the image jet, and they found a family of self-similar profiles scaling with the jet depth applicable within the interaction region. A recent investigation by Liepmann, 1990 showed that instabilities in the near-field region of a round jet are strongly influenced by the presence of a free surface, and that the geometrical nature of the jet is altered through changes in the entrainment field near the free surface.

Measurements of turbulence quantities beneath a free surface have recently

been reported. Komori, *et al.*, 1982, measured the turbulent fluctuations and Reynolds stress beneath a free surface in an open channel flow using a single component LDV. Their measurements show that the velocity fluctuations become anisotropic as the free surface is approached, those normal to the surface becoming diminished while those parallel to the surface are enhanced. Rashidi and Banerjee, 1988 used data obtained in flow visualization experiments using bubble streaks to reach the same conclusion: near a free surface, the turbulent energy is redistributed from the normal to the parallel fluctuations. Ramberg, *et al.*, 1989, made turbulence measurements with hot film anemometers in a developing planar jet issuing at a free surface. Their flow conditions were chosen to minimize free surface deflections, isolating the kinematic effect of the free surface on the turbulence, and again the turbulent fluctuations were shown to become anisotropic as the surface was approached.

The channel flow and planar jet flow experiments just described consider inherently two-dimensional flows without surface waves; by contrast, the interaction of a circular jet with a free surface is highly three-dimensional, giving rise to considerable free surface deformations and to the generation of surface waves (Bernal and Madnia, 1988). Because of its inherent simplicity and the large body of supporting experimental data, the axisymmetric jet provides an excellent basic flow to which to add the complications of a free surface (Figure 1.2). Detailed LDV measurements of the mean flowfield and turbulence quantities, including all components of the Reynolds stress tensor, in an initially circular jet issuing beneath and parallel to a free surface are presented.

CHAPTER II

EXPERIMENTAL APPARATUS

2.1 Laser Doppler Velocimeter

In order to determine the instantaneous velocity of an unsteady flow, it is necessary to measure the velocity components in three directions simultaneously. To measure velocities very near a free surface requires a non-intrusive technique; the Laser Doppler Velocimeter (LDV) is ideally suited to the task. A three-component underwater LDV was designed and built for taking measurements in a towing tank (Willmarth, 1987); fundamental to the design of this instrument was that both the last optical component that transmits laser light to the measuring volume and the first optical component that receives scattered light from the volume be completely submerged. Optical fibers were used to carry light between the underwater probes and the above-water optics.

The LDV used the three strongest lines of an argon-ion laser in a three-color, six-beam, differential-Doppler configuration to measure three non-orthogonal velocity components (Figure 2.1). One beam of each beam pair incorporated frequency shifting to discriminate between forward and reversed flow.

A Coherent, Inc. Innova 90-6 argon-ion laser was operated with all lines lasing and without an etalon. Its aperture was stopped down sufficiently to guarantee that the three strongest lines, green (514.5 nm), blue (488.0 nm), and violet (476.5)

lased in their TEM₀₀ (gaussian) modes only.

The beam emanating from the laser was collimated to be parallel over approximately two meters (2 m) as required for efficient coupling into the optical fibers. The beam was then separated into its component colors, and all but the three strongest beams were blocked. Each of these three beams was passed through a half-wave polarization rotator plate so its axis of polarization could be oriented correctly with respect to its corresponding prism beamsplitter; this is necessary so that the beamsplitter separates the incident beam into two beams of approximately equal intensity. Of the three laser beams, the violet is the weakest, having only about half of the power of the green and blue beams. Because the optical fibers are known to degrade with use, especially at the blue wavelength, it was desirable to attenuate the blue and green beams so that their power was comparable to that of the violet beam. To do this, polarization prisms were added to the optical paths of the blue and green beams between their polarization rotators and beamsplitters; the combination of polarization rotator and polarization prism acted as an attenuator, allowing the beam power to be controlled. The beamsplitters separated each beam into a pair of beams of approximately equal intensity, and the stronger beam of each beam pair was frequency shifted using an acousto-optic Bragg cell driven at 40 MHz. The six beams were then coupled into six single-mode, polarization-preserving optical fibers for transmission to the underwater optics. The above-water optical components were obtained from TSI, Inc.

The underwater optics were housed in two watertight modules, each consisting of a stainless steel can and an optical glass window. The optical fibers carried the

laser light to the underwater modules, and each fiber terminated at a collimating lens within its respective module. One of the modules used the two green and two violet beams to measure two orthogonal velocity components; the other used the two blue beams to measure a single velocity component. The re-collimated beams within each module were brought to a crossing by a lens of focal length approximately two meters (2 m) underwater. The beam diameters at their crossings were approximately .020 cm and the half-angle between the beams was approximately 2.4 degrees, yielding a measurement volume approximately .47 cm in length. When the measurement volumes from the two modules overlap, the effective length is reduced to approximately .050 cm.

Also contained within the underwater modules were the receiving optics. Within each module, the lens used to focus the transmitted beams acted also as a receiving lens for the scattered light, and a second lens inside each module brought the scattered light to a focus at the optical coupler of a multimode receiving fiber. The compact nature of the probe design required the use of two mirrors in the receiving optics. All optical surfaces in contact with air were anti-reflection coated, whereas those in contact with water were uncoated. The transmitting and receiving fibers were jacketed in two 10 m waterproof cables. A schematic of the single component probe showing the internal optics is given in Figure 2.2.

The receiving fibers carried the scattered light to three photodetectors. Each fiber was terminated at a collimating lens, one at the blue photodetector and the other at a dichroic mirror and the green and violet photodetectors. Each photodetector used a narrow-band optical filter to pass only the appropriate wavelength, and the filtered,

collimated beam was directly incident on the photomultiplier tube. Either return fiber could be connected to either the blue or the green and violet photodetectors, allowing the modules to be operated in either direct backscatter or off-axis backscatter. Because of the improved signal to noise ratio obtained by collecting off-axis, all measurements reported used off-axis collection.

The two optical modules were mounted oppositely in a 20.3 cm diameter cylindrical housing, and a pair of underwater second-surface mirrors folded the six beams to a crossing approximately 1.25 m from the axis of the housing. The green and blue beam pairs measured two non-orthogonal velocity components in a plane, while the violet measured a third component perpendicular to that plane. Orthogonal components were obtained by appropriate linear combinations; these transformations are given in the Appendix. The LDV modules, housing, and mirrors were designed by Prof. W. W. Willmarth (Willmarth, 1987) in consultation with TSI, Inc., and were manufactured by TSI. A stepping motor and 100:1 harmonic drive gear reducer attached to the end of the underwater housing and contained inside a watertight can allowed the LDV to be rotated about its axis. The LDV was suspended from a carriage that allowed translation in a direction perpendicular to the housing axis. Through a combination of translation and rotation, any point within a plane could be reached. By rotating the LDV rather than translating it vertically, the weight and complexity of the required traverse was kept to a minimum. More importantly, the measurement volume could be positioned to locations just beneath a free surface without any of the beams becoming interrupted by the surface itself. A schematic of the LDV and its traverse is given in Figure 2.1.

2.2 Experimental Facility and Jet Nozzle Design

The LDV was operated in a 2400-gallon glass-walled towing tank at The University of Michigan, designed specifically to allow measurements in the wakes of small towed bodies. For a description of the design and construction of the towing tank, refer to Hirs, 1990. For the jet experiment, an underwater jet nozzle was suspended from the facility's towing carriage, and the carriage was manually translated along its rails using a leadscrew and flexure. The jet was mounted to a bracket fastened to the facility's towing carriage by a small machinist's vise, and the jet depth was altered by changing the position of the bracket in the vise. The carriage from which the LDV was suspended was traversed along a pair of rails aligned perpendicular to those of the towing carriage and was positioned under computer control. A schematic showing the towing facility, the LDV, and the jet is given in Figure 2.3.

The towing facility was filled with tap water, and a standpipe allowed the free surface to be mechanically cleaned of surfactants prior to taking measurements. The water in the facility was continuously filtered through a canister-type filter to which diatomaceous earth had been added. The filtering had two effects: First, the water was cleaned of suspended rust and dirt, down to about 1 micron in size, greatly reducing contributions to the LDV noise from scattering particles too small to generate measurable signals. Second, the water was continuously circulated, maintaining a uniform temperature throughout the facility. This was necessary as slight temperature non-uniformities caused local variations in the index of refraction, allowing the laser beams to wander from their crossing point. The filter circuit was bypassed when

taking measurements to limit the effects of recirculation within the facility to those of the jet flow itself. The effects of recirculation and confinement by facility walls have been shown to diminish the jet momentum flux with distance downstream (Schneider, 1985; Swean, *et al.*, 1989).

The filter circuit and jet delivery circuit are shown in Figure 2.4. A submersible pump drew water from the floor of the towing tank. When the filter was being used, the flow from the pump passed through the filter and then discharged back into the tank. When the filter was not being used, the flow from the pump passed through a compression closure valve and precision bore flowmeter to a reservoir tank above the towing facility. The water level in the reservoir tank was maintained by a standpipe, the overflow from which discharged back into the towing tank. Water from the reservoir flowed under the action of gravity through a valve and flowmeter to the jet nozzle. By drawing from and discharging into the towing facility, seeding uniformity between jet fluid and ambient fluid could be assured (see Section 3.5, Seeding and Surface Contamination, below).

The turbulent jet issued from a brass nozzle attached to a settling chamber constructed of two lengths of concentric PVC pipe. The smaller diameter pipe was machined to fit inside the larger diameter pipe and was cut into sections, the sections serving as spacers between the inlet, honeycomb, screens, and nozzle. This modular approach made it very easy to disassemble the jet to change screens, etc. The flow entered the settling chamber through a length of garden hose and was diverted around a brass plate within the inlet section. It then passed through a coarse screen, a honeycomb made from cocktail straws, and two fine screens before entering the nozzle

contraction. The nozzle contour was a fifth degree polynomial having specified diameter at inlet and exit, and both zero slope and zero curvature at inlet and exit. The inlet diameter was 5.90 cm and the exit diameter was .635 cm, giving an area contraction ratio of 86:1. The settling chamber and nozzle are shown in Figure 2.5.

2.3 Signal Processing

The signals from the three photodetectors were downmixed against reference frequencies derived from the 40 MHz signals used to drive their respective Bragg cells. The downmixing frequencies on each component were chosen to allow measurement of reversed flow and to eliminate the effects of fringe-biasing. Fringe biasing occurs when scattering particles pass through the measurement volume along trajectories that do not cross a sufficient number of fringes to generate a valid measurement. Provided that the shift frequency corresponds to a velocity at least twice as great as the largest reversed component encountered in the flow, there will be no orientations of the velocity vector that are outside of the measurable range (Whiffen, 1976). The downmixing frequencies were chosen so that stationary scattering particles generated frequencies of .2 MHz, .2 MHz, and .5 MHz on the green, blue, and violet components, respectively, and moving scatterers having positive velocity components in the coordinate system of the jet generated frequencies in excess of these selected shift frequencies.

Because the low- and high-limit filters on the TSI signal processors did not allow sufficient variability to limit high frequency noise, the downmixed signals from the green and blue photodetectors were first filtered using Krohn-Hite Model 3103A band-pass filters, and the filtered signals were input to TSI Model 1980B counter-

type signal processors. The violet signal was passed directly to its signal processor. The digital outputs of the three burst processors were passed to a data interface which allowed a simultaneity criterion to be placed on the data: all three processors must report valid Doppler information within a specified time window, or else the data would be ignored. A thumbwheel switch was used to set a timeout period approximately equal to the time required for a scattering particle travelling with the measured mean velocity to traverse the measurement volume. The interface also allowed the time between data points to be recorded. The interface was designed by Prof. L. P. Bernal and was built at the university. The data from the three processors and the interface timer was transferred to a LeCroy MM8206A dual port memory housed in a LeCroy 8013A CAMAC chassis. The data was then transferred to an IBM PC-AT computer using a LeCroy 8901A GPIB interface and a National Instruments GPIB-PC-III interface controller. Finally, the data was stored on 20 Mb Bernoulli removable cartridge disks.

2.4 Software

The software for data acquisition and subsequent reduction and analysis was written by the author for the IBM PC in FORTRAN and was compiled using the Microsoft FORTRAN Optimizing Compiler, Version 4.1. Subroutine libraries for EGA graphics, RS-232 communications, GPIB communications, and interfacing the Microsoft Mouse were purchased off-the-shelf. These libraries were used within a data acquisition program that featured automated control of probe positioning and handling of data files, a hierarchy of mouse-driven menus, and a graphical interface with real-time velocity histograms and statistical information.

CHAPTER III

EXPERIMENTAL PROCEDURES

3.1 LDV Alignment

The design of the LDV is such that the six transmitted laser beams must cross at the same point in space, and the receiving optics must image this crossing point in order that a single scattering particle can generate a signal on the three photodetectors simultaneously. The optical fibers could be individually adjusted from within their watertight housings, and the overall crossing could be achieved by adjustments to the second surface mirrors. The receiving fibers could also be adjusted from within the probes to place their ends at the focal point of the receiving optics.

After several months of use, it was found that the LDV had become misaligned, most likely because of temperature cycling from repeated immersions in water much colder than the room temperature. Rather than disassemble the watertight modules to realign the beams, external beamsteering modules consisting of a pair of wedge prisms were added to each beam ahead of the second surface mirrors. The wedges could be independently rotated, allowing angular adjustment of each beam within a cone of half-angle approximately $1/4$ degree. To use a pair of wedge prisms as a beamsteerer requires that the index of refraction of the medium on either side of each wedge be the same. Because the steerers were to be used underwater, they were designed to contain water between their optical components.

Although the individual beams could be externally steered, there was no way to incorporate an external adjustment to the receiving optics. The individual beams were therefore steered to have their intersection at the spot imaged by the receiving optics as follows: a laser beam was coupled into the receiving fiber of each module, in effect operating the receiving optics 'in reverse'. The spot to which the optics brought the reverse-coupled light to a focus is the volume imaged by the receiving optics. While viewing the receiving spot through an underwater microscope objective, the transmitted beams from the same probe were steered to cross within the spot. Adjustments to the second surface mirrors were made to bring the receiving spots of the two modules into coincidence, and final adjustments were then made to assure that the six individual beams crossed at this same point.

Because of the large angle between the optical axes of the two probes (approximately 53 deg.), it was difficult to verify with a microscope objective that all six beams actually crossed. When in doubt, the beam crossings were viewed directly using a Wild 60X Zoom microscope. The LDV housing was rotated so that the beam crossings were positioned within a few inches of the water surface, and a screen was placed underwater at the crossings. The microscope could then be made to image the point on the screen where the beams crossed without requiring that any part of the microscope itself be underwater.

3.2 LDV Calibration

In a two-beam differential Doppler system, the frequency of the Doppler signals is in direct proportion to that component of the velocity vector lying in the plane of the two beams and at right angles to their bisector or optical axis (Drain,

1980; Adrian, 1983). The constant of proportionality may be found from the wavelength λ of the incident light beams and the angle κ between the beams according to

$$\frac{U}{f_D} = \frac{\lambda}{2 \sin(\kappa/2)} .$$

As the wavelength λ is known precisely, a measurement of the angle κ allows calibration of the system. Such a measurement was not easily implemented underwater, and instead a direct measurement of the Doppler signal off of the periphery of a wheel rotating with known speed was used to calibrate the system. The proportionality constant between velocity and frequency, expressed in (m/s)/MHz, is numerically equal to the fringe spacing in microns, so that determining this constant is equivalent to determining the spacing between the fringes.

A series of fine grooves were left in the edge of the wheel when it was machined on a lathe. These grooves acted to diffract the laser light striking the wheel, resulting in a pair of light sheets reflected from the wheel's edge. The wheel could be positioned so that the reflected light sheets were symmetric about the incident beams that produced them, meaning that the center of the wheel lay on the bisector of the incident beam pair (the optical axis of the module). The wheel was then moved along the optical axis so that the edge of the wheel passed through the measurement volume and produced Doppler bursts when rotating. The radius of the wheel was known, and the rate of rotation was determined by measuring the average time between Doppler bursts from an isolated scatterer attached to the wheel. The time between bursts was

measured using a Hewlett-Packard counter. From the known velocity of a point on the wheel's edge and the measured Doppler frequency, the proportionality constants between velocity and frequency were determined for the green and blue beam pairs directly. A direct measurement of the proportionality constant for the violet beams was not made; instead, the value of this constant was determined from that of the green beams. Because both beam pairs are brought to a focus by the same lens, the angle κ is taken to be the same for both pairs. The proportionality constants between green and violet then vary inversely as their wavelengths.

Though the three calibration constants (or fringe spacings) as determined above are sufficient to calculate velocity components from Doppler frequencies, several geometrical constants are required to resolve those components into an orthogonal set, to relate those to corresponding velocity components in a coordinate system fixed at the jet nozzle, and to traverse the LDV measurement volume to specific locations relative to the jet. The required constants are the optical angles α_g and α_b (refer to Figure A.1 in the Appendix), defined as the angles formed between the optical axes of the green and blue beams, respectively, and a line perpendicular to the probe axis and passing through the measurement volume; the probe standoff radius R , defined as the distance from the axis of the LDV probe to the measurement volume; the location (x, y, z) of the measurement volume in the jet coordinate system; and the lookup angle θ , defined as the angle between the plane of the green and blue beams and the horizontal.

The optical angles were determined from direct measurements of the lengths of the individual beams from the beam crossing to a line parallel to the probe housing,

and the standoff radius was determined by direct measurement of the distance between the probe housing and the beam crossings. These measurements were made only when the beam crossings were adjusted. The position of the measurement volume in the jet coordinate system and the lookup angle were calculated from the positions reported by the stepping motors, provided that the position and lookup angle were known when power was applied to the motors. This 'home' position was determined at the start of each day, or each time the jet was repositioned. The procedure for determination of 'home' was as follows: a pointer was placed on the floor of the test facility, its height having been adjusted so that when the measurement volume was positioned at the tip of the pointer, the green and blue beams were horizontal. With the measurement volume at this point, the pulse counters on the stepping motor controllers were reset to zero. The measurement volume was then positioned to another pointer attached to the jet nozzle, and the position of this pointer, relative to that on the tank floor, was determined from the pulse counters. The coordinates (x , y , z) of the pointer relative to the jet nozzle were known *a priori*, and the lookup angle θ was calculated from the position information. The pulse counters were then reset to zero, and the current position was taken to be 'home'. All subsequent probe motions were made with respect to this 'home' position.

In using the above calibration technique, it was assumed that the green and blue beam pairs lay in the same plane, and that the violet beams lay in a perpendicular plane. Deviations from these assumptions were so small as to be difficult to measure and were disregarded. The transformations between the velocity components measured by the individual beam pairs and those in an orthogonal system fixed in the probe are

developed in the Appendix, as are the coordinate transformations between the probe-fixed and jet-fixed coordinates.

3.3 Coordinate Conventions

Three coordinate systems were used in converting Doppler frequency measurements into jet velocity components: an 'optical' coordinate system, whose non-orthogonal components lie in the directions in which the three beam pairs actually measure velocity, a 'probe' coordinate system, having orthogonal components that rotate with the LDV probe, and a 'jet' coordinate system, having orthogonal components fixed to the jet nozzle. The definition of the optical and probe coordinate systems is postponed until the Appendix, where the transformations among the three coordinate systems are developed.

The jet coordinate system (x, y, z) was defined as follows: the axis of the jet defined the x coordinate, positive downstream, the z component was defined as positive toward the free surface, and the y component was defined to make (x, y, z) right-handed. The origin of the coordinate system was taken at the jet exit.

3.4 Jet Alignment

The rails on which the LDV traversed were first leveled and then aligned, as follows: one of the rails was leveled using a gunsight level and was aligned perpendicular to the facility's towing rails using a carpenter's square. The second rail was also leveled and was then made parallel to the first rail by measuring the separation between the two rails at their ends using a tape measure. Having aligned the rails on which the LDV carriage traversed, the LDV was then leveled and aligned with respect to its carriage, ensuring that the probe axis was then parallel to the

facility's towing rails. The alignment was verified by measuring the distances between the two ends of the LDV probe and one of the facility's towing rails.

The jet then had to be aligned on its towing carriage to be parallel to the facility's towing rails. At first this was done rather imprecisely by measuring the distance from the two ends of the bracket supporting the jet to the towing rails, and angular misalignments of approximately $1/2$ deg. were revealed in LDV measurements of jet profiles (see the discussion of Figure 4.3a). A more accurate alignment technique was adopted for subsequent measurements. A line was scribed on the jet settling chamber parallel to the centerline of the jet, and a pointer was attached to one of the tank walls. This allowed the jet to be aligned by judging visually the amount of runout between the scribe line and the pointer as the jet was traversed the length of the settling chamber (approximately 30 cm). Adjustments to the bracket holding the jet to the carriage were made until there was no runout observable to the eye, and the jet was therefore brought parallel to the towing rails. The 'home' position was then re-established by the procedure outlined in Sec. 3.2. Changes in the jet depth between deep and shallow required that the jet be realigned using this method, as did removing the jet to purge it of trapped air. Small changes in the jet depth were made by adding or siphoning water from the tank, and the jet depth was accurately measured by positioning the LDV measurement volume first to its 'home' position on the jet centerline and then to the undisturbed free surface, recording the vertical coordinate reported by the stepping motors. The jet was turned off during this measurement.

3.5 Seeding and Surface Contamination

The towing tank was filled with filtered tap water through a 9 kilowatt electric

heater that raised the temperature of the water to room temperature; this was done to minimize the possibility of probe misalignment because of thermal cycling. The facility water was continuously filtered as described above to remove rust and dirt particles down to about one micron in size. Prior to measuring, titanium dioxide (TiO_2) particles of the rutile crystalline form were added to the facility water as LDV scatterers. The particles were approximately 3 microns in size, and approximately 4 g of seed was added to the 2400-gallon facility. Through trial and error, it was found that the addition of more seed did not noticeably improve the data rate, serving only to diminish the signal to noise ratio of the Doppler signals. The seed was first added to a small quantity of tap water and was stirred into suspension. To this suspension was added a trace amount of Darvan-C, a polyelectrolyte, as an anti-flocculent. The mixture was then added to the towing tank near the pump intake and was circulated throughout the tank until it was dispersed (refer to Figure 2.4 for the pump circuit). The degree to which the seed was dispersed throughout the tank was judged by eye from the scattering of the LDV laser beams. When the measurement volume was placed in the jet flow very near the free surface, the surface deformations caused the internally reflected beams to form crude light sheets. These light sheets illuminated the suspended seed, and gradients in seed concentration were easily discerned. Generally, about twenty minutes was required before the seed was sufficiently dispersed that gradients were no longer visible. Because the jet reservoir was supplied from the towing tank, seeding uniformity between the jet fluid and the entrained fluid was achieved, eliminating a possible source of measurement bias.

A standpipe in the towing facility allowed the free surface to be mechanically

skimmed of surface-active agents. At the start of each day, the water level in the tank was adjusted to compensate for evaporation, and the free surface was drawn off through the standpipe. A fan positioned at the end of the towing tank opposite the standpipe served to generate a surface motion toward the standpipe. The water level in the tank was then adjusted by siphoning off water as necessary. For the flow visualization experiments, a small electric pump adapted from an automobile windshield washer was used to skim fluid from the surface in order to maintain the clean surface condition.

The condition of the free surface could be judged from the behavior of small surface waves. When the surface was clean, it appeared very active, and small waves would propagate almost without attenuation. When the surface was not clean, either because of dirt deposited on the surface over a period of days or because of the deliberate addition of insoluble surfactants, the small waves were quickly damped by the surface film or surfactant monolayer.

Oleyl alcohol, an insoluble surfactant, was used to contaminate an otherwise clean free surface. The state relationship between surface pressure or surface tension and surfactant concentration is well established (Gaines, 1966; Hirs, 1990). A quantity of oleyl alcohol was dissolved in benzene, and the solution was added to the surface with a pipette, giving the desired reduction in surface tension once the benzene had evaporated.

3.6 Data Acquisition

Data acquisition tasks included setting of the band-pass filters and the input conditioner and timer modules on the burst processors, adjusting the simultaneity

window for differing conditions encountered in the flowfield, and monitoring the incoming data. The tasks were somewhat iterative, a change in one often requiring a change in the others.

Certain operating parameters were set once and were not changed. These included the downmix frequencies and directions on the frequency shifters, and the mode, cycles/burst, and comparator settings on the signal processors. As already discussed, the downmix frequencies were chosen to allow measurement of flow reversals and to minimize the effects of fringe biasing; the shift directions were chosen in accordance with the sign convention for each component. The burst processors were operated in the Single Measurement per Burst (SM/B) mode, meaning that once a burst was validated as having the required minimum number of cycles, the processor was inhibited from taking another measurements until all cycles of the burst were completed. This is in contrast to the Continuous mode of operation where the processor can generate several valid measurements per burst. SM/B mode was chosen as this eliminated the possibility of velocity biasing from multiple measurements per burst. The minimum number of cycles per burst to constitute a valid measurement was set to 16. Bursts typically had many more than 16 cycles, and the data rate showed no significant difference between using 8 and 16 cycles. The timing measurements made on 16 cycles were less likely to be in error than those made on 8. The burst processors applied a '5/8' comparison to every burst timing measurement, requiring that the ratio of the time for 10 cycles to that for 16 be 5/8 to within a specified percentage. A 1% criterion for the '5/8' comparison was used on all three burst processors to minimize the possibility of erroneous measurements from noisy

signals.

Computer generated histograms of the frequency data were continuously updated as the data were taken. From the histograms, the band-pass filters were set, narrow enough to eliminate noise (especially at higher frequencies), but wide enough so that the filters did not introduce a bias to the data. The residence time within the measurement volume of a scattering particle travelling with the mean speed was calculated, and the simultaneity window on the LDV interface was set to approximately this value. Because this residence time could vary over almost two orders of magnitude in going from the high speed flow on the jet centerline to the very low speed flow in the entrainment field, it was important that the time window be continually updated. With the filters and simultaneity window set, the incoming data were then written to a disk file. The velocity histograms and statistics were used to determine the number of data points required for acceptably converged averages. Typically, at least 1000 points were taken at each measuring location, as this provided well converged statistics and smooth histograms. The probe was then traversed to another measurement position, and the process was repeated.

The Doppler bursts were displayed on an oscilloscope during the data acquisition, allowing monitoring of the signal quality and simultaneity. This was helpful in setting the filter bandwidth, and gave a good indication of the percentage of Doppler bursts that were simultaneous among the three channels. With the LDV in its best alignment, about one in four or five validated bursts on each processor was accepted as simultaneous. The data rate was highest when the water had been filtered to remove small particles and diminished over time as the water became dirty.

Simultaneous data rates typically varied between about 5 and 30 Hz.

3.7 Data Reduction and Bias Correction

Because of the low data rates, it was not possible to recreate the velocity signal in time. Instead, ensemble averages of individual velocity realizations had to be used to determine the mean velocities and Reynolds stresses, introducing the possibility that particle arrival statistics could influence the averaged results. Because higher speed fluid carries more scattering particles through the measurement volume in unit time than lower speed fluid, the probability of making an individual velocity measurement is biased toward higher velocities. Various bias corrections have been suggested to compensate for this effect (e.g., McLaughlin and Tiederman, 1969; Dimotakis, 1976), but there is considerable argument over which correction to use (Edwards, *et al.*, 1989). Because simultaneous three-component measurements yield the instantaneous magnitude of the velocity vector, a McLaughlin-Tiederman type correction was used, weighting each individual velocity measurement with the reciprocal of its magnitude. This bias correction was observed to reduce the streamwise mean velocity approximately 4 percent in comparison to uncorrected measurements. The Reynolds stresses were also corrected in this manner.

Individual velocity measurements having any component lying outside of four standard deviations from its mean were discarded, and mean velocities and Reynolds stresses were calculated from the remaining data. The averaged data was written to computer disk files for later analysis and plotting.

3.8 Flow Visualization

Flow visualization using Laser Induced Fluorescence (LIF) was used near the

end of the investigation to reveal the structure of the surface current discovered in the course of LDV measurements. The jet reservoir was filled with a 3 ppm solution of fluorescein dye, and a laser light sheet made with a plano-cylindrical lens was used to excite the dye. Still photographs of the illuminated dye were taken with a Nikon FM-2 camera with either a 135 mm f2.8 Nikkor telephoto lens and Kodak T-Max 400 film or a 50 mm f1.4 Nikkor lens and T-Max 3200 film.

The deformations of the free surface were visualized using a shadowgraph technique, and images of the free surface deformations were recorded on video tape so that estimates of surface wave properties such as wavelength and wave speed could be obtained. When collimated light is incident on a free surface from below, the refraction of light rays at the water-air interface causes the rays to converge where the surface is convex (elevations) and to diverge where it is concave (depressions). A screen placed above the free surface will therefore show regions of light and dark illustrating the curvature of the free surface (see, for example, Walker, 1988). A mercury vapor lamp was used as a light source, and by placing the source at the focal point of a spherical mirror, the light was collimated. The collimated light was made incident on the free surface from below by reflecting it off of a flat mirror beneath the towing tank and passing it through the glass bottom of the tank. A piece of ground glass was used as the imaging screen, and the screen was positioned at various heights above the free surface so that sharp images of regions of the free surface having characteristically different curvatures could be obtained. To record surface deformations in the highly active jet/free-surface interaction region, the ground glass screen was placed approximately 2 cm from the free surface; to capture the smaller

amplitude surface deformations associated with wave motions to the sides of the jet,
the screen was positioned further from the surface, approximately 10 cm.

CHAPTER IV

RESULTS AND DISCUSSION

Simultaneous three-component LDV measurements of the flowfield of a round turbulent jet were made for both a deep jet ($h/d=50$) and a shallow jet ($h/d=2$) to quantify the effects of the free surface on the jet's development, both in its mean flow and turbulence characteristics. The jet exit diameter was .635 cm, and the exit velocity was 200 cm/s, giving a Reynolds number $Re \equiv U_e d / \nu$ of approximately 12,700. The Froude number based on the jet exit velocity and depth, $Fr \equiv U_e / (gh)^{1/2}$, was 5.66 for the shallow case.

4.1 Deep Jet Measurements

Measurements of the deep jet were made as a baseline from which to judge the effects of the free surface on the development of the shallow jet. Shown in Figure 4.1 is the streamwise mean velocity component on the jet centerline plotted so as to reveal its inverse dependence on the downstream coordinate x , as expected from similarity considerations. For comparison, the results of Wygnanski and Fiedler, 1969, are included in Figure 4.1. The streamwise mean velocity U_c on the jet centerline and the streamwise coordinate x are taken as the appropriate velocity and length scales for showing self-similarity in the velocity and turbulence profiles. Elsewhere, the jet diameter d is used as the length scale for nondimensionalization, as for example, in normalizing the depth h .

Figure 4.2 shows the centerline variation of the turbulence fluctuations, the primes denoting RMS quantities. The fluctuations are scaled by the streamwise mean velocity on centerline at the same downstream location, taken from Figure 4.1. The effects of the potential flow in the core region of the jet can be seen to about 10 diameters downstream, after which the turbulent character of the jet becomes fairly well established. It should be noted that even at 32 diameters downstream, the turbulence quantities have not yet become fully self-preserving; Wygnanski and Fiedler, 1969, have shown that self-similarity in the turbulent fluctuations and higher moments does not occur until beyond about 80 diameters downstream. Finally, the turbulent fluctuations are not isotropic, the streamwise fluctuations being some 10 percent more intense than the horizontal (cross-stream) and vertical fluctuations; this is characteristic of turbulent flows having a dominant streamwise mean velocity component.

Velocity measurements in horizontal and vertical profiles through the jet centerline were made at downstream stations of 16, 24, and 32 diameters. At each measuring location, at least 1000 individual simultaneous three-component velocity measurements were recorded, this number being sufficient that accumulated statistics (mean and standard deviation) vary over time less than one percent. In addition, the velocity histograms recorded on each LDV component appear visibly converged, not changing noticeably with further measurements. The nine plots comprising Figure 4.3 show the horizontal data, and those of Figure 4.4 show the vertical.

Figure 4.3a shows profiles of the streamwise mean velocity component U , normalized by their respective centerline velocities, U_c . The solid line represents the

one-parameter theoretical (mixing length) profile of Tollmien (see Rajaratnam, 1976). The three profiles are indeed self-similar, even by as few as 16 diameters downstream. The velocity data is clearly not centered about $y=0$; this is the result of a misalignment of the jet of approximately $1/2$ degree. On the basis of this observation, a more accurate jet alignment method was adopted (see Sec. 3.4, Jet Alignment, above). Figure 4.3b shows a horizontal profile of the horizontal mean velocity component V . The profile is seen to be antisymmetric about the jet centerline, and near the jet centerline, the flow is outward, corresponding to the outward growth of the shear flow, whereas near the jet edges, the flow is inward, corresponding to entrainment. The vertical mean velocity component W is shown in Figure 4.3c. By symmetry, there should be no vertical mean velocity component across the horizontal plane $z=0$; the observed scatter in the data is too great to be accounted for by random or statistical error alone, but the cause of the scatter is not known.

Profiles of the RMS velocity fluctuations appear as Figures 4.3d-f. The data show the most variability near the jet centerline, where vestiges of the potential flow at the core of the jet may still influence the data. The profile maxima are still some 10 percent below those reported by Wygnanski and Fiedler for the fully developed jet; reference to Figure 4.2 shows that the fluctuations are still tending towards higher values with increasing distance downstream.

The off-diagonal terms of the Reynolds stress tensor are presented in Figures 4.3g-i; the diagonal terms are of course the squares of the RMS velocity fluctuations just shown. The Reynolds stress \overline{uv} , shown in Figure 4.3g, is in good agreement with that reported by Wygnanski and Fiedler. The other two stresses, \overline{vw} and \overline{uw} , should be

zero, as the vertical fluctuations across a horizontal plane of symmetry should yield zero in the mean.

The vertical profiles corresponding to the horizontal profiles of Figure 4.3 are shown in Figure 4.4; they could, in fact, have been plotted together (provided that the data of Fig. 4.3 were corrected for the misalignment of the jet), with y or z the radial axis, and V or W the corresponding radial velocity. The agreement between the two sets of profiles is very good, indicating that the jet is indeed axisymmetric.

It is interesting to note that the V profile of Fig. 4.4b shows the same degree of scatter as the W profile of Fig. 4.3c, yet the V and W profiles of Figs 4.3b and 4.4c, respectively, show well defined profiles. The scatter in the data of Figs. 4.4b and 4.3c is too large to be simply statistical error, but the cause of the scatter is not known. It is not, however, the result of a limitation on the accuracy of the LDV in measuring any particular velocity component. Many three-component LDV systems determine their third component as the small difference of two large quantities, and there has often been a much larger error associated with this third component than with the other two.

Vertical profiles of the deep jet data at $x/d=32$ are replotted in Figures 4.5a-d to simplify comparison with the shallow jet data that follows.

4.2 Shallow Jet Measurements

Having both verified the accuracy of the LDV and established the behavior of the deep jet between 16 and 32 diameters downstream, the jet was repositioned to its shallow setting, $h/d=2$. At this depth, the first indication of free surface activity occurs at around 8 to 10 diameters downstream, and by 16 diameters, there is

considerable free surface deformation and wave generation. By 32 diameters, the free surface activity has calmed considerably near the jet centerline, though there is still wave activity and occasionally surface dimples nearer the jet edges. The region between 16 and 32 diameters was the focus of the present investigation.

The near-surface measurements reported herein were taken beneath a free surface that was cleaned of surfactants as described in Sec. 3.5, Seeding and Surface Contamination. Surfactants were shown by Bernal, *et al.*, 1989, and Hirs, 1990 to play a significant role in the interaction of discrete vortices with the free surface, both in their trajectories and in the behavior of surface waves generated as a result of the interaction. As is discussed later, the surface condition is extremely important to the observation of certain features of the jet/free-surface interaction. Because all naturally occurring water samples contain surface-active agents to some degree, it is suspected that measurements reported previously by others in the literature might show effects of surface contamination.

Measurements of vertical profiles were first made at 16 and 32 diameters to investigate the most significant effects of the free surface on the jet development. Figure 4.6a shows the streamwise mean velocity component U at $x/d=16$, plotted using the same similarity variables as used in Figures 4.3 and 4.4. This choice is simply to make comparison among the figures convenient; Bernal and Madnia, 1988, showed that the similarity scaling appropriate to the interaction region of the jet and free surface involves the jet depth h ; however, as all the near-surface data reported in this text were taken at the same depth, scaling the data with h does not reveal anything of the data's dependence on depth. At this downstream location, the effect of the free

surface on the streamwise mean velocity is to shift the profile toward the surface and make the profile slightly fuller above the centerline. The profile otherwise retains its shape, except just beneath the surface. The solid line in the figure indicates the position of the undisturbed free surface, and the last point in the profile is actually above this position. LDV data may still be obtained above the position of the undisturbed surface, but such data are subject to a bias that arises from obtaining measurements beneath surface elevations but not depressions. The measurement points were spaced more closely above the jet centerline than below it.

Figure 4.6b shows the horizontal mean velocity component V and the vertical mean velocity component W , at $x/d=16$. The effect of the free surface is restrict entrainment from above, reducing the vertical mean velocity to zero as the surface is approached. Below the jet centerline, the jet again behaves like its deep counterpart.

The RMS velocity fluctuations are shown in Figure 4.6c. Again, the behavior of the jet above the centerline is like that below it; however, the maximum in each of the profiles appears to occur below the jet centerline. Although this could be simply an artifact of random error, it is plausible on physical grounds. From consideration of the model of the jet merging with an identical image jet above the free surface (see Introduction, above), there is a region of potential flow between the two jets, upstream of the point where they merge. As the jets merge, this potential 'core' must become mixed with the jet turbulence, diminishing the intensity of the jet fluctuations on average.

Figure 4.6d shows the Reynolds stress components. The stress \overline{uw} is diminished to zero as the free surface is approached, but still shows little deviation from its

behavior below the jet or from that of the deep jet. The remaining off-diagonal stress components should be zero by symmetry; the small systematic deviation from zero evident in the \overline{uv} component may be the result of a slight lateral misalignment of the jet.

Vertical profiles at 32 diameters downstream are shown in Figure 4.7. The streamwise mean velocity component, shown in Figure 4.7a, clearly demonstrates the effect of the free surface on the behavior of the jet above its centerline. The centerline velocity is no longer the maximum velocity in the profile; with increasing distance downstream, the location of the profile maximum will change from the jet centerline to the free surface. Bernal and Madnia, 1988, showed that a family of similarity profiles, characterized by the value of x/h , exists in the interaction region of the jet and the free surface; within this interaction region, the mean velocity profiles have their maxima occurring above the jet centerline but below the free surface. The profile of Figure 4.7a, having $x/h=16$, is certainly within this interaction region. Although the mean velocity on the jet centerline is not the profile maximum, it is still used to normalize the velocity data; there is a practical reason for this, i.e., it is necessary to measure only a single point and not an entire profile to determine a velocity scale. As the difference between the centerline and profile maximum velocities is quite small, this difference is of little consequence.

Figure 4.7b shows the horizontal and vertical mean velocity components. Near the free surface, the vertical mean velocity is diminished toward zero, although it does not appear to reach zero, indicating an upward velocity at the free surface. Also, the entrainment velocity beneath the jet is higher than that for either the $x/d=16$ data or

the deep jet data. These somewhat unsettling results suggest a systematic error in the measurements, which is believed to be a consequence of fringe biasing on the violet component, indicative of a shift frequency set too low (see below).

The influence of the free surface on the turbulent fluctuations is made extremely clear by Figure 4.7c. Very near the free surface, the energy of the turbulent fluctuations is redistributed from the fluctuations normal to the surface to those parallel to it. The vertical fluctuations are diminished just beneath the free surface, while the streamwise and horizontal (cross-stream) fluctuations are enhanced. Measurements of turbulence beneath free surfaces in inherently two-dimensional flows (e.g. Komori, *et al.*, 1982; Rashidi and Banerjee, 1988; Ramberg, *et al.*, 1989) have shown similar results. Beneath a shear-free plane surface, as is strictly appropriate to the image model discussed above, both the vertical velocity and vertical fluctuations must go to zero as a consequence of the plane boundary condition; however, the interaction of the jet with a free surface shows considerable surface activity, and the vertical fluctuations need not go to zero as the surface is approached. The vortex ring experiments of Bernal and Kwon, 1988 (also Kwon, 1989; Song, *et al.*, 1990) revealed a process of vortex reconnection to the free surface. It is suggested that the physical mechanism acting to redistribute the energy from the vertical to the streamwise and horizontal fluctuations is a process whereby vortex filaments in turbulent flow become attached to the free surface. This mechanism, fundamental to the interaction of discrete, laminar vortices with a free surface, could be equally fundamental to the interaction of turbulence with a free surface.

The Reynolds stress components are shown in Figure 4.7d, the stress \overline{uw} again

tending toward zero as the free surface is approached. Comparison of this profile to the mean velocity profile shown in Figure 4.7a reveals that the product $-\overline{uw}(\partial U/\partial z)$, corresponding to the rate of production of turbulent kinetic energy per unit mass, is always positive, indicating a transfer of energy from the mean flow to the turbulence.

The vertical mean velocity W of Figure 4.7b appears to show a systematic bias toward positive values, possibly as a consequence of fringe biasing on the violet component. What was discovered was that the mean velocity component on the violet channel was slightly different at different downmix frequencies. This behavior is suggestive of fringe biasing, a measurement bias toward certain orientations of the velocity vector (Whiffen, 1976). Data obtained at $x/d=16$ and shown in Figures 4.6a-d used shift frequencies of .2 MHz, .2 MHz, and .5 MHz on green, blue, and violet, respectively, whereas those at $x/d=32$, shown in Figures 4.7a-d, used .1 MHz, .1 MHz, and .2 MHz. It was decided to adopt the higher shift frequencies for all subsequent measurements, and a detailed vertical profile between the jet centerline and the free surface at $x/d=32$ was taken again. This profile is shown in Figures 4.8a-d. Unfortunately, measurements were not made beneath the jet centerline using the higher shift frequencies; this was an oversight.

From the position of the free surface as indicated on the figures, it is apparent that the last several measurements in each profile were taken at positions actually above the location of the undisturbed free surface. The measurements show a bias attributable to the interruption of the measurement volume by the free surface deformations. These surface deformations allow measurements to be obtained, for example, in the crests of waves but not in the troughs. The streamwise mean velocity

profile of Figure 4.8a again shows that the maximum velocity in the profile does not occur at the jet centerline but above it, nearer the free surface. The vertical mean velocity, shown in Figure 4.8b is shifted downwards from that of Figure 4.7b and becomes zero at the free surface. The data above the free surface show that the effect of biasing is to indicate a downward vertical velocity component. Figure 4.8c shows the RMS velocity fluctuations; again, the magnitude of the normal fluctuations is diminished near the free surface while the magnitudes of the parallel fluctuations are enhanced. Above the location of the undisturbed free surface, the streamwise fluctuations appear diminished, rather than enhanced, and the difference between the vertical and horizontal fluctuations is apparently increased over that shown in Figure 4.7c. However, these also are most likely the effects of bias.

4.3 Surface Current Measurements

The vertical profiles of Figures 4.6, 4.7, and 4.8 revealed differences in both the mean flow and the turbulence quantities between measurements made above the jet centerline and below it. To investigate more completely the nature of these differences and to characterize the jet behavior in planes not passing through the centerline of the jet, measurements were made in a series of horizontal profiles at varying distances above and below the jet centerline. Measurements were recorded at 16, 24, and 32 diameters downstream.

Recall that the coordinate origin lies on the jet centerline, and z is defined as positive toward the free surface. The profiles having positive z/d are therefore between the jet centerline and the free surface, and those having negative values are below the jet centerline. The profiles were taken for negative values of y rather than

positive, and are therefore shown this way, although this may lead to slight temporary confusion in interpreting the signs of the horizontal velocity data. The complete profiles can be inferred from considerations of symmetry (or antisymmetry) about $y=0$.

The water level in the tank was adjusted so that the position of the undisturbed free surface was approximately .075 cm above $z/d=2$; this was done in order that surface deformations interrupted the LDV measurement volume only infrequently, thereby reducing the possibility of biasing the velocity measurements (see discussion of Figs. 4.8a-d, above).

At 32 diameters downstream, considerable differences develop among the profiles as the free surface is approached. Evident in Figure 4.9a, showing the streamwise mean velocity, is that the jet becomes much wider as the free surface is approached, and that this widening is confined to a very shallow layer. The profile at $z/d=1$ is little different from that on the jet centerline $z/d=0$, yet the tails of the profile at $z/d=2$ extend to beyond twice the width of the jet at $z/d=0$. Comparison of the profiles at $y/x=0$ shows the maximum streamwise mean velocity to occur below the free surface (in agreement with the previous vertical profile), but beyond $y/x=-.10$, this maximum velocity occurs at the surface itself. The horizontal mean velocity is shown in Figure 4.9b, positive values corresponding to entrainment inward from the sides and negative corresponding to lateral growth of the shear flow outward. It is only in the two profiles taken nearest the surface that the data differ distinctly from those taken elsewhere throughout the jet, and the tails of these two profiles show the flow to be outward, away from the jet centerline. The vertical mean velocity profiles of Figure 4.9c show that there is little or no vertical component to the flow in this thin layer

near the surface; the slight deviation from zero velocity in the tail of the profile at $z/d=2$ is not judged to be significant.

The mean flow data at this distance downstream show that in close proximity to a clean free surface, there exists a shallow layer of fluid moving predominantly downstream and away from the jet centerline. The lateral extent of this layer is far greater than that of the turbulent jet flow beneath it. This layer is referred to as the surface current, and the discussion that follows is concerned primarily with the character of this surface current.

The existence of a surface current, much wider than the jet flow that produces it, does not obviously follow from earlier considerations of a jet merging with its image above the surface. Measurements of a jet issuing near a solid wall, reported by Davis and Winarto, 1980, show the jet to become increasingly oblate with distance downstream, its horizontal extent becoming significantly greater than its vertical. But the comparison between the free surface jet and the wall jet made by Bernal and Madnia, 1988, showed the two flows to be fundamentally different, attributing this to the differing dynamics of vorticity at solid and free surfaces. The jet measurements of Bernal and Madnia did not reveal a surface current, although this could be the result of two factors: either measurements were not taken close enough to the free surface to resolve the shallow current layer, or surface contaminants inhibited the development of the layer.

The RMS turbulent fluctuations are plotted in Figures 4.9d-f. Near $y/x=0$, the magnitude of the vertical velocity fluctuations w' is diminished well below those of the streamwise and horizontal fluctuations, in agreement with the earlier result of Figures

4.7c and 4.8c. However, within the surface current layer (beyond $y/x = -0.15$), the magnitudes of the horizontal and vertical fluctuations become almost equal, while that of the streamwise fluctuations continues to diminish. The Reynolds stress \overline{uv} , shown in Figure 4.9g, is seen to diminish toward zero within the current layer, but indicates that the current contains turbulent fluid. Examination of Figures 4.9h and 4.9i shows the remaining Reynolds stresses to be very nearly zero throughout the current. The observed behavior of the RMS fluctuations in a region of small or vanishing Reynolds stress suggests that appreciable contributions to the velocity fluctuations may arise from orbital motions in the flow beneath surface waves travelling perpendicular to the jet centerline. Such a wave motion contributes to the horizontal and vertical velocity fluctuations, but not to the streamwise fluctuations or to the off-diagonal Reynolds stress components.

Visual observations of the free surface for the present configuration ($Re=12,700$, $h/d=2$) indicate that the wave fronts propagate in a direction very nearly perpendicular to the downstream direction. Figure 4.10 shows a shadowgraph and sketch of the free surface deformations above the shallow jet, $h/d=2$, issuing beneath a clean free surface. There is considerable surface activity near the jet centerline where large-scale structures within the jet interact with the free surface, and it is only near the edges of this active region that the surface disturbances become identifiable as outward travelling waves. These waves appear to arise from an accumulation or coalescence of waves generated by incoherent, random surface disturbances throughout the interaction region. The inset on the left is a shadowgraph, inverted black for white to show the wave crests as dark rather than light. Also indicated are closely spaced

hair-like disturbances aligned at about 40 deg. to the jet axis; these disturbances are observed in video images of the free surface but were not resolved in the inset shadowgraph.

From video recordings of the surface shadowgraphs, the wavelengths of the outward travelling waves were found to be approximately 1 to 4 cm, indicating that the effects of both gravity and surface tension are important, and the wave speed was approximately 25 cm/s, very nearly the minimum wave speed for such waves moving on deep water (Lighthill, 1978). An estimate of the surface wave contribution to the RMS horizontal and vertical velocity fluctuations within the surface current may be obtained from the orbital velocities beneath linear free surface waves on deep water having the measured wavelengths and wave speed, provided a reasonable estimate of the amplitude ζ of these waves is available. Such an estimate is provided by the depth of the LDV measurement volume beneath the undisturbed free surface, as surface deformations were sometimes, though infrequently, observed to interrupt the measurement volume. The measurement volume was approximately .075 cm beneath the free surface, and for waves having the minimum wave speed on deep water, $\lambda=1.7$ cm and $c=23$ cm/s. From the orbital velocity, one finds $v' = w' = \omega\zeta/\sqrt{2}$, or approximately 4.4 cm/s. At $x/d=32$, the centerline velocity is $U_c=45$ cm/s, giving approximately .098 for the normalized RMS cross-stream and vertical velocity fluctuations. This value is in reasonable agreement with those measured by the LDV (as shown in Figs 4.9e and 4.9f), indicating that much of the RMS fluctuations within the surface current can be attributed to surface waves.

Bernal and Madnia, 1988, investigated the behavior of surface waves generated

in the interaction region of the jet with the free surface and found that the angle of wave propagation, measured with respect to the downstream direction, increased with increasing jet exit velocity. They reported a propagation angle of 39 degrees for a jet Reynolds number $Re=8900$ and depth $h/d=1$, increasing to about 60 degrees by $Re=13,000$ at the same depth. The degree of surface contamination was not reported, however, and it is likely that their observations were of waves on a contaminated surface. Surface waves, especially of smaller wavelengths, are attenuated by the presence of surfactants, and the surface observations of Bernal and Madnia appear to be only of the larger disturbances.

Figures 4.11a-i show the behavior of the surface current at $x/d=24$, revealing qualitatively the same features as in Figures 4.9a-i. The streamwise and horizontal mean velocity components (Figures 4.11a and 4.11b) show the beginnings of the surface current. The vertical velocity, Figure 4.11c, is negative at the free surface, indicating a downward component to the flow. However, the free surface at $x/d=24$ shows considerable activity, and free surface deformations often interrupt the measurement volume. This results in a measurement bias, as described in the discussion of Figures 4.8a-d. Figures 4.11d-f again show that the magnitude of the RMS vertical fluctuations becomes smaller than those of the streamwise and horizontal fluctuations as the free surface is approached near the jet centerline, but that the magnitudes of the horizontal and vertical fluctuations become nearly equal in the surface current. The Reynolds stresses also diminish to zero within the current layer. Some mention of the behavior of the \overline{uw} Reynolds stress near $y/x=0$ should be made. Below the location of maximum streamwise mean velocity, \overline{uw} should be (and is)

negative, whereas above it, \overline{uw} is positive; in the deep jet, \overline{uw} is in fact antisymmetric about $z=0$. The behavior observed in Figure 4.11i, negative on $z=0$, positive above $z=0$, and diminishing to zero at the free surface is therefore as expected and is not a dramatic effect of the free surface.

The data taken in horizontal planes above and below the jet centerline at $x/d=16$ are shown in Figures 4.12a-i. Comparison of the streamwise mean velocity U at $z/d=1$ and -1 (Figure 4.12a) shows that the jet profile is slightly fuller towards the free surface, but there otherwise appears to be little difference between these profiles, indicating that the free surface has not significantly distorted the jet at this location downstream. Figure 4.12b shows the horizontal mean velocity, entraining inward near $y/x=-.20$. There is no indication yet of the existence of a surface current, although measurements at the surface $z/d=2$ were not made. Figures 4.12d-f show the turbulent fluctuations, revealing the behavior at one diameter above and below the jet centerline to be almost identical (compare the outlined and filled triangles). The Reynolds stress \overline{uv} , shown in Figure 4.12g also shows close agreement between the behavior above and below centerline and shows this stress to diminish as the free surface is approached. It is somewhat surprising that the jet shows little effect of the free surface at this distance downstream, because the surface shows considerable activity beyond about $x/d=12$, especially in the generation of surface waves.

The evolution of the surface current with increasing distance downstream was studied from measurements of the mean flowfield in planes at $x/d=16, 24, 32, 48$, and 64 . The LDV was operated without requiring simultaneity among the three components; this allowed determination of the mean velocities, but sacrificed

determination of turbulence quantities in favor of a higher data acquisition rate.

Contour plots of the streamwise mean velocity are shown in Figures 4.13a-e, and vector plots of the horizontal and vertical mean velocities are shown in Figures 4.14a-e. The data shown are averages of at least 2000 individual velocity realizations per channel at each measurement location, and are not corrected for velocity bias. The jet depth was $h/d=2$, and the location of the jet nozzle is indicated on the figures by the shaded circle.

The data taken at $x/d=16$ show that the jet profile is somewhat fuller above its centerline than below it (Figure 4.13a), and the flow near the jet edges is primarily directed inward, indicating entrainment, except at the free surface itself (Figure 4.14a) where it shows a small outward component.

At $x/d=24$, the surface current is beginning to become apparent, both in the streamwise velocity (Figure 4.13b) and the horizontal and vertical velocities (Figure 4.14b). Note that the surface current is visible only within a very shallow layer near the free surface. The data of Figure 4.13b show the $U/U_c=.05$ profile at the surface to extend to about twice its lateral extent on the jet centerline $z/d=0$. From Figure 4.14b, the flow just beneath the surface ($z/d=1.5$) is seen to have a small outward component, while that at the surface is significantly greater. The indicated downward velocity in the data taken at the surface is most likely the result of a velocity bias attributable to surface deformations (see the discussion of Figures 4.9c and 4.11c). Except within the surface current, the flow at the edges of the jet is seen to be inward, showing entrainment.

By 32 diameters downstream, the surface current is well established (Figures

4.13c and 4.14c). The surface current extends laterally to beyond twice the width of the jet flow just beneath it, and its thickness has increased to about twice that at $x/d=24$. The horizontal component V is seen to be greatest at the surface, and the vertical component W within the current layer is essentially zero. Just beneath the current layer, the flow near the jet edges is entraining fluid, and within the current layer, the strong outward flow causes the velocity vectors to be turned outward. This turning of the flow is suggestive of the action of a streamwise vortex lying toward the outboard edge of the jet. A similar pattern appears in wake data taken behind surface ships and is sometimes attributed to the action of large streamwise vortices shed from the stern of the ship (Lugt, 1981). Stretching of ring-like or helical vortex structures within the jet could lead to streamwise vortices in the mean; Liepmann, 1990, has shown that the effect of the free surface on the initial instabilities within the jet is to cause a stable configuration of streamwise vorticity just beneath the free surface. This feature might be characteristic of the interaction between more general three-dimensional turbulent shear flows and a free surface.

At $x/d=48$, the surface current is seen to be the dominant feature of the cross-stream flow, the cross-stream components elsewhere in the flowfield having diminished with distance downstream, as seen in Figure 4.14d. From Figure 4.13d, the surface current is seen to have grown in depth sufficiently that the overall flow less resembles a shallow current superposed on a circular jet and more suggests an oblate jet, reminiscent of the flowfield of a jet issuing above a solid wall (Davis and Winarto, 1980). An obvious difference between the two flows occurs at the solid or free boundary; in the former case, the flow velocity must of course be zero, while the

free surface data indicate that the velocities are actually greatest at the free boundary. Correlation measurements made by Davis and Winarto showed that large-scale motions normal to the solid surface give rise to strong outflow motions along the surface, much like the flow at a stagnation point in the cross-flow plane. These motions were found to yield much greater turbulent mixing in planes parallel to the solid surface than normal to it.

The data obtained at $x/d=64$ are qualitatively similar to those at $x/d=48$, but the surface current has grown sufficiently deep that measurements on the jet centerline show both a widening of the horizontal profile and a component of outward flow (Figures 4.13e and 4.14e). From the mean velocity measurements at $z/d=2$, the angle at which the surface current spreads, measured from the jet centerline, is found to increase from approximately 35 deg. at $y/d=12$ to approximately 44 deg. at $y/d=24$.

Bernal and Madnia, 1988, did not report a surface current, but their measurements were limited to profiles through the jet centerline. Their shallow jet measurements did not extend downstream beyond $x/d=40$, and they measured only the streamwise velocity component. It is possible that although their jet formed a surface current, they did not make measurements that revealed it.

4.4 Flow Visualization

In order to understand the origin of the surface current, flow visualization studies using Laser Induced Fluorescence (LIF) were performed. Fluorescein dye was added to the jet reservoir tank and the flow issuing from the jet was illuminated with a laser light sheet (Sec. 3.7, Flow Visualization). The light sheet was oriented either vertically to illuminate cross-stream planes or horizontally to illuminate planes parallel

to the free surface.

With the light sheet oriented vertically, the boundaries of the jet were observed to be very uneven and unsteady, emitting puffs of dyed, vortical fluid in random directions; these puffs initially propagated outward, away from the jet. The puffs that were emitted downward into the entraining flow were rapidly slowed and were rarely observed to propagate far from the jet boundary. However, those puffs that were ejected near a clean free surface, having little downward velocity, were observed to continue to move parallel to the surface away from the jet boundary. These emissions propagated to several jet half-widths in a thin layer just below the surface. The average of many such emissions and their subsequent propagation outward gives rise to a mean outward flow which is observed as the surface current.

Figure 4.15a shows an LIF photograph in a cross-stream plane at $x/d=32$ beneath a clean free surface, illustrating the ejected fluid that forms the surface current. Dyed fluid is ejected from the jet and propagates beneath the free surface under the influence of its corresponding image fluid above the free surface.

Figure 4.15b shows an LIF photograph in the same plane beneath a free surface contaminated with oleyl alcohol, an insoluble surfactant. The concentration was $1.3 \times 10^{-7} \text{ cm}^3$ of surfactant per cm^2 of free surface, chosen to give a surface pressure (or reduction in surface tension) of 9 dynes/cm. This concentration was sufficient that the surface motions were considerably damped by the surfactant. When oleyl alcohol was present, the surface current was not observed to form, and fluid ejected from the jet was laterally confined. This confinement is attributed to the interaction of ejected vortical structures with secondary vorticity of opposite sign generated beneath the

contaminated surface. The effects of free surface contamination on the trajectories of laminar vortex pairs is discussed in Hirs, 1990. When the free surface is clean, the vortices are observed to propagate laterally beneath the surface in the manner of point vortices interacting with their images beneath a plane of symmetry (Lamb, 1932); however, when the surface is contaminated, interactions between the primary vortices comprising the pair and secondary vortices generated beneath the surfactant covered surface cause the vortices to rebound, limiting their propagation outward. It is suggested that the same mechanism is effective in restricting the lateral propagation of vortical structures ejected from the jet beneath a contaminated free surface.

It is difficult to characterize the nature of the ejections from the jet on the basis of visualizations in vertical planes alone. This is because the ejected structures move through the light sheet. What appears as an ejected structure having a component of lateral motion could instead be a 'frozen' structure translating downstream inclined to the flow direction. The light sheet was repositioned to be horizontal, and the nature of the surface current was investigated in planes parallel to the free surface. Figure 4.16a shows an LIF visualization of the surface current with the light sheet positioned just beneath the free surface, about .3 cm from it; the jet depth was $h/d=2$. Near the jet exit, the lateral spreading of the jet agrees with the behavior of a deep jet, growing wider at approximately 12 deg. to the flow direction. However, beyond about 12-16 diameters downstream, the spreading angle near the free surface is much greater, approximately 40 deg. to the axis of the jet. The current layer shows strands or tendrils of ejected fluid that remain relatively coherent throughout the layer, and high concentrations of dye within the emitted fluid suggest that turbulent mixing is greatly

reduced within the surface current. This reduced mixing is confirmed by the LDV measurements made within the surface current.

Figure 4.16b shows an LIF visualization in a horizontal plane through the jet centerline, $z=0$. The small spreading angle characteristic of the deep jet is apparent up to about 24 diameters downstream, at which distance the surface current is revealed only by structures sufficiently large to intercept the light sheet from above. At this depth, the ejected structures no longer resemble strands, but appear instead as blobs or islands of dyed fluid.

Shadowgraph images of the free surface show considerable deformations near the jet centerline, where energetic structures within the jet interact with the surface. Away from the jet centerline, surface waves generated by these disturbances appear to coalesce into waves having wavelengths of approximately 1 to 4 cm and travelling nearly perpendicular to the jet axis at approximately 25 cm/s. Comparison of the wave speed estimated from shadowgraph videos of the free surface and of the flow velocities measured by the LDV within the surface current shows the wave speed to be three to many times greater than the mean speeds within the current; the waves propagate on top of the surface current (Peregrine, 1976). The hair-like corrugations of the free surface observed near the jet centerline and sketched in Figure 4.10 are believed to be the result of waves propagating over the ejected structures observed in LIF visualizations (Figure 4.16a) within the current layer.

CHAPTER V

CONCLUSIONS

Detailed three-component LDV measurements of the mean velocity and Reynolds stress tensor in the turbulent flowfield of a jet issuing beneath and parallel to a free surface were made to quantify aspects of the behavior of turbulence near a free boundary. For the measurements reported, the Reynolds number based on the jet diameter and exit velocity was $Re=12,700$, and the Froude number based on the jet exit velocity and depth was $Fr=5.66$.

The measurements show that near the jet centerline, where the interaction of the jet flow with the free surface is most energetic, the RMS velocity fluctuations become anisotropic as the free surface is approached: the fluctuations normal to the surface are diminished, while those parallel to the surface are enhanced. Although previous experiments have shown similar behavior beneath a free surface (e.g. Komori, *et al.*, 1982; Ramberg, *et al.*, 1989), these investigations were concerned with the behavior of turbulence in two-dimensional flows beneath essentially plane free surfaces. The present study extends these results to a highly three-dimensional flow in which free surface deformations, three-dimensional entrainment, and wave generation are significant.

Under the conditions investigated, the interaction of the jet flow with the free surface led to the generation of surface waves near the jet centerline. These waves,

generated continually and apparently at random by the large-scale structures in the jet flow, were observed to coalesce and to propagate in a direction almost perpendicular to the jet axis. Measurements of the wavelength and wave speed from shadowgraph images of the free surface showed the waves to be gravity-capillary waves travelling with approximately the minimum wavespeed, 23 cm/s, attainable on deep water having a clean free surface.

Characteristic of the jet interaction with a clean free surface was the formation of a shallow surface current, propagating downstream and laterally at an angle of approximately 40 degrees to the jet centerline. The width of this current was found to be much greater than that of the primary jet flow. Laser Induced Fluorescence (LIF) was used to visualize the nature of the surface current. Fluorescein dye was added to the jet reservoir, and the dye issuing from the jet was illuminated with a laser light sheet. The visualizations showed that the jet is highly unsteady, emitting puffs of dyed fluid in random directions. Puffs of fluid emitted just beneath a clean free surface were observed to propagate under the influence of their corresponding images above the surface to a lateral distance of several jet half-widths away. The average of many such emissions and their subsequent propagation outward gives rise to the surface current. The ejected fluid was found to form strand-like or tendril-like structures inclined at approximately 40 deg. to the jet axis, in agreement with the velocity measurements made within the surface current. These structures were observed to contain relatively high concentrations of dye, indicating that turbulent mixing is greatly reduced within the surface current.

Although the surface current arises from the ejection of turbulent jet fluid, the

orbital motions beneath surface waves superposed on the surface current contribute to the measured RMS velocity fluctuations. Turbulence measurements within the surface current showed that the cross-stream and vertical RMS velocity fluctuations were approximately equal, and were greater than the streamwise RMS velocity fluctuations. This result is distinctly different from that found near the jet centerline, where the vertical fluctuations were diminished and the parallel fluctuations were increased. The effects of the surface current and the surface waves are not expected to be independent, as the depth of the current was comparable to the wavelength of the observed waves.

Oleyl alcohol, an insoluble surfactant, was added to the free surface in sufficient concentration that the surface motions were visibly damped. The addition of the surfactant suppressed the formation of the surface current through the interaction between vortical fluid ejected from the jet and secondary vorticity of opposite sign generated beneath the surfactant covered surface.

APPENDIX

APPENDIX

COORDINATE TRANSFORMATIONS

The equations governing the transformation from Doppler frequencies measured by the green, blue, and violet beam pairs to velocity components in both probe and jet coordinates are developed.

The directions in which the individual beam pairs of the LDV probe measure velocity define three non-orthogonal vectors having fixed orientations with respect to the probe. The only ambiguity in this 'optical' coordinate system lies in the choice of which direction is positive on each component. The downmix frequencies on the green and blue components were chosen so that a scattering particle moving downstream, as determined by the jet flow, generates frequencies in excess of the selected shift frequency. The downmix setting on the violet beams was chosen so that a particle moving toward the free surface generated a frequency in excess of its selected shift frequency. Let g , b , and v denote unit vectors in these three non-orthogonal directions. The velocity components in these three directions depend linearly on the measured Doppler frequencies with proportionality constants determined during calibration of the LDV probe (Section 3.2):

$$V_g = \kappa_g(f_g - f_{gs})$$

$$V_b = \kappa_b(f_b - f_{bs})$$

$$V_v = \kappa_v(f_v - f_{vs})$$

The κ 's are the measured proportionality constants between velocity and frequency,

and the subscript s denotes the shift frequency.

For a differential Doppler LDV system, the measured velocity components are the projections of the flow velocity vector onto the unit vectors g , b , and v :

$$V_g = V \cdot g$$

$$V_b = V \cdot b$$

$$V_v = V \cdot v$$

The above relationships express the velocity components measured by the LDV in terms of the velocity vector and green, blue, and violet unit vectors. This non-orthogonal system is transformed into an orthogonal system that rotates with the LDV probe (Figure A.1). The 'probe' coordinate system is defined as follows: the axis of the LDV probe defines the x coordinate, positive downstream, and a line perpendicular to this axis and passing through the measurement volume defines the radial coordinate r . The remaining angular coordinate θ is defined as positive for rotations of the LDV measurement volume toward the free surface from below. Expressing the components of the velocity and unit vectors in the probe coordinate system, the above equations become

$$\begin{bmatrix} g_x & g_r & g_\theta \\ b_x & b_r & b_\theta \\ v_x & v_r & v_\theta \end{bmatrix} \begin{bmatrix} V_x \\ V_r \\ V_\theta \end{bmatrix} = \begin{bmatrix} V_g \\ V_b \\ V_v \end{bmatrix}$$

In the probe system, the unit vectors g , b , and v have constant components, giving

$$\begin{bmatrix} \cos \alpha_g & -\sin \alpha_g & 0 \\ \cos \alpha_b & \sin \alpha_b & 0 \\ 0 & 0 & 1 \end{bmatrix} \begin{bmatrix} V_x \\ V_r \\ V_\theta \end{bmatrix} = \begin{bmatrix} V_g \\ V_b \\ V_v \end{bmatrix}$$

The velocity components V_x , V_r , and V_θ in the probe coordinate system are determined by solving the above linear system of equations. The coefficient matrix, being constant in the probe system, is inverted once, and the velocity components in the probe system are subsequently obtained from those in the optical system by multiplication.

The jet coordinate system was defined in Section 3.3. The streamwise coordinate is x , positive downstream, the vertical coordinate is z , positive toward the free surface, and the horizontal component is y , positive so that the jet coordinate system is right handed. The probe and jet coordinates are related by a rotation about x through the angle θ (Figure A.2) giving

$$\begin{bmatrix} U \\ V \\ W \end{bmatrix} = \begin{bmatrix} 1 & 0 & 0 \\ 0 & \cos \theta & -\sin \theta \\ 0 & \sin \theta & \cos \theta \end{bmatrix} \begin{bmatrix} V_x \\ V_r \\ V_\theta \end{bmatrix}$$

REFERENCES

REFERENCES

- Abramovich, G. N. (1963), The Theory of Turbulent Jets, MIT Press, Cambridge, MA.
- Adrian, R. J. (1983), "Laser Velocimetry," in Fluid Mechanics Measurements, ed. R. J. Goldstein, Hemisphere Publishing Corp., pp. 155-244.
- Anthony, D. G., Willmarth, W. W., Madnia, K., and Bernal, L. P. (1990), "Turbulence Measurements in a Submerged Jet Near a Free Surface," *Proc. 18th Symp. Naval Hydro.*, Ann Arbor, MI.
- Bernal, L. P. and Madnia, K. (1988) "Interaction of a Turbulent Round Jet with the Free Surface," *Proc. 17th Symp. Naval Hydro.*, The Hague, Netherlands.
- Bernal, L. P. and Kwon, J. T. (1989), "Vortex Ring Dynamics at a Free Surface," *Physics of Fluids A*, 1 (3), pp. 449-451.
- Bernal, L. P., Hirska, A., Kwon, J. T., and Willmarth, W. W. (1989), "On the Interaction of Vortex Rings and Pairs with a Free Surface for Varying Amounts of Surface Active Agent," *Physics of Fluids A*, 1 (12), pp. 2001-2004.
- Browand, F. K. and Laufer, J. (1975), "The Role of Large Scale Structures in the Initial Development of Circular Jets," *Proc. 4th Symp. on Turbulence in Liquids*, University of Missouri-Rolla, eds. J. L. Zakin and G. K. Patterson.
- Davis, M. R. and Winarto, H. (1980), "Jet Diffusion from a Circular Nozzle above a Solid Wall," *J. Fluid Mech.*, 101 (1), pp. 201-221.
- Dimotakis, P. E. (1976), "Single Scattering Particle Laser Doppler Measurements of Turbulence," in *Applications of Non-Intrusive Instrumentation in Fluid Flow Measurement*, AGARD CP-193.
- Dimotakis, P. E., Miake-Lye, R. C., and Papantoniou, D. A. (1983), "Structure and Dynamics of Round Turbulent Jets," *Physics of Fluids*, 26 (11), pp 3185-3192.
- Drain, L. E. (1980), The Laser Doppler Technique, Wiley-Interscience.
- Edwards, R. V. (1987), "Report of the Special Panel on Statistical Particle Bias Problems in Laser Anemometry," *J. Fluids Eng.*, 109, pp. 89-93.
- Gaines, G. L. (1966), Insoluble Monolayers at Liquid-Gas Interfaces, Interscience.
- Hirska, A. (1990), "An Experimental Investigation of Vortex Pair Interaction with a Clean or Contaminated Free Surface," Ph. D. Thesis, The University of Michigan, Ann Arbor, MI.

Komori, S., Ueda, H., Ogino, F., and Mizushima, T. (1982), "Turbulence Structure and Transport Mechanism at the Free Surface in an Open Channel Flow," *Int. Journal Heat Mass Transfer*, **25** (4), pp. 513-521.

Kwon, J. T. (1989), "Experimental Study of Vortex Ring Interaction with a Free Surface," Ph. D. Thesis, The University of Michigan Program in Ship Hydrodynamics Technical Report No. 89-06, Ann Arbor, MI.

Lamb, H. (1932), *Hydrodynamics*, 6th ed., Cambridge University Press.

Liepmann, D. (1990), "The Near-Field Dynamics and Entrainment Field of Submerged and Near-Surface Jets," Ph. D. Thesis, University of California, San Diego, San Diego, CA.

Lighthill, J. (1978), *Waves in Fluids*, Cambridge University Press.

Lugt, H. J. (1981), "Numerical Modelling of Vortex Flows in Ship Hydrodynamics: A Review," *Proc. 3rd Int'l. Conf. Numerical Ship Hydro.*, Paris, France, pp. 297-316.

Lyden, J. D., Hammond, R. R., Lyzenga, D. R., and Shuchman, R. A. (1988), "Synthetic Aperture Radar Imaging of Surface Ship Wakes," *Journal of Geophysical Research*, **93** (C10), pp. 12,293-12,303.

Madnia, K. (1989), "Interaction of a Turbulent Round Jet with the Free Surface," Ph. D. Thesis, The University of Michigan Program in Ship Hydrodynamics Technical Report No. 89-05, Ann Arbor, MI.

McLaughlin, D. K. and Tiederman, W. G. (1973), "Biasing Correction for Individual Realization of Laser Anemometer Measurements in Turbulent Flow," *Physics of Fluids*, **16** (12), pp. 2082-2088.

Munk, W. H., Scully-Power, P., and Zachariasen, F. (1987), "Ship Wakes from Space, The Bakerian Lecture, 1986," *Proc. Royal Soc. London A*, **412**, 231-254.

Peregrine, D. H. (1976), "Interaction of Water Waves and Currents," *Adv. Appl. Mech.*, **16**, pp. 9-117.

Rajaratnam, N. (1976), *Turbulent Jets*, Elsevier Scientific Publishing Co., New York, NY.

Rajaratnam, N. and Humphries, L. A. (1984), "Turbulent Non-Bouyant Surface Jets," *Journal Hydraulic Res.*, **22** (2), pp. 103-115.

Rajaratnam, N. and Subramanyan, S. (1985), "Plane Turbulent Bouyant Surface Jets and Jumps," *Journal Hydraulic Res.*, **23** (2), pp. 131-146.

Ramberg, S. E., Swean, T. F., and Plesnia, M. W. (1989), "Turbulence Near a Free Surface in a Plane Jet," NRL Memorandum Report 6367, Naval Research Laboratory, Washington, DC.

Rashidi, M. and Banerjee, S. (1988), "Turbulence Structure in Free-Surface Channel Flows," *Physics of Fluids*, **31** (9), pp. 2491-2503.

Schneider, W. (1985), "Decay of Momentum Flux in Submerged Jets", *J. Fluid Mech.*, **154**, pp. 91-110.

Song, M., Kachman, N., Kwon, J. T., Bernal, L. P., and Tryggvason, G. (1990), "Vortex Ring Interaction with a Free Surface," *Proc. 18th Symp. Naval Hydro.*, Ann Arbor, MI.

Swean, T. F., Ramberg, S. E., Plesnia, M. W., and Stewart, M. B. (1989), "Turbulent Surface Jet in Channel of Limited Depth," *Journal of Hydraulic Engineering*, **115** (12), pp. 1587-1606.

Walker, J. (1988), "The Amateur Scientist: Shadows cast on the bottom of a pool are not like other shadows. Why?" *Scientific American*, July, 1988.

Willmarth, W. W. (1987), "Design of Three Component Fiber Optic Laser Doppler Anemometer for Wake Measurements in a Towing Tank," *Proc. Int'l. Towing Tank Conf.*

Whiffen, M. C. (1976), "Polar Response of an LV Measurement Volume," in *Minnesota Symp. on Laser Anemometry Proc. - 1975*, ed. E. R. G. Eckert, University of Minnesota, Minneapolis, MN.

Wynanski, I. and Fiedler, H. (1969), "Some Measurements in the Self-Preserving Jet," *J. Fluid Mech.*, **38** (3), pp. 577-612.

FIGURES

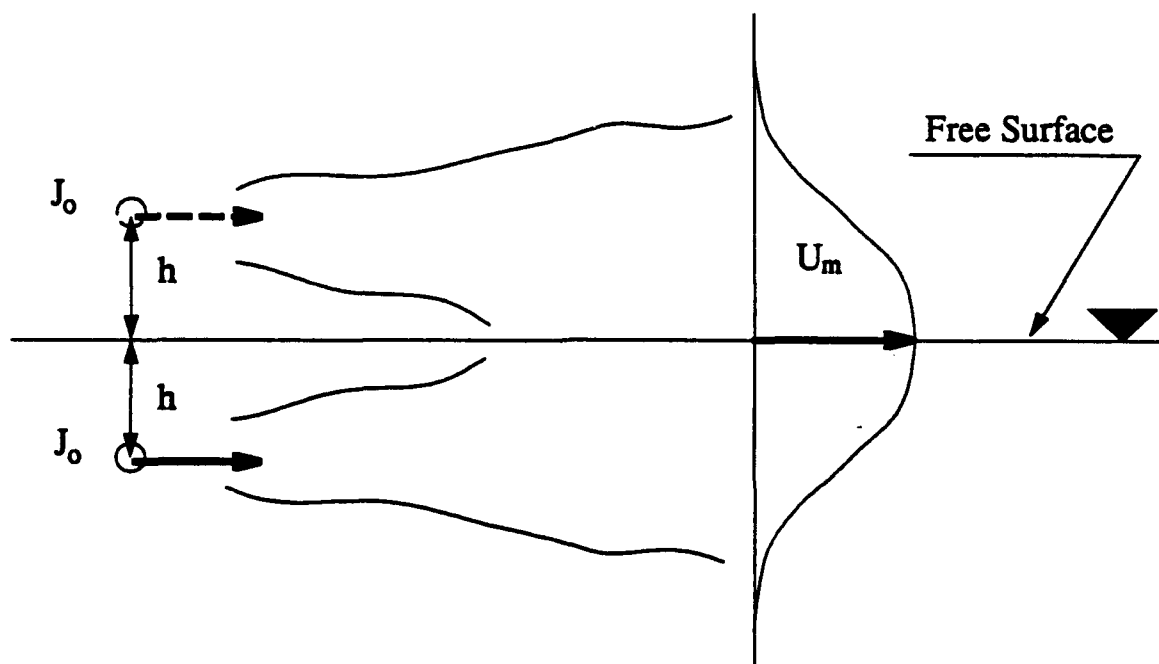


Figure 1.1. Schematic of the jet and image model of Bernal and Madnia, 1988, for the free surface jet. The jet depth is h , and the exit momentum flux is J_o . U_m denotes the maximum streamwise mean velocity in the profile.

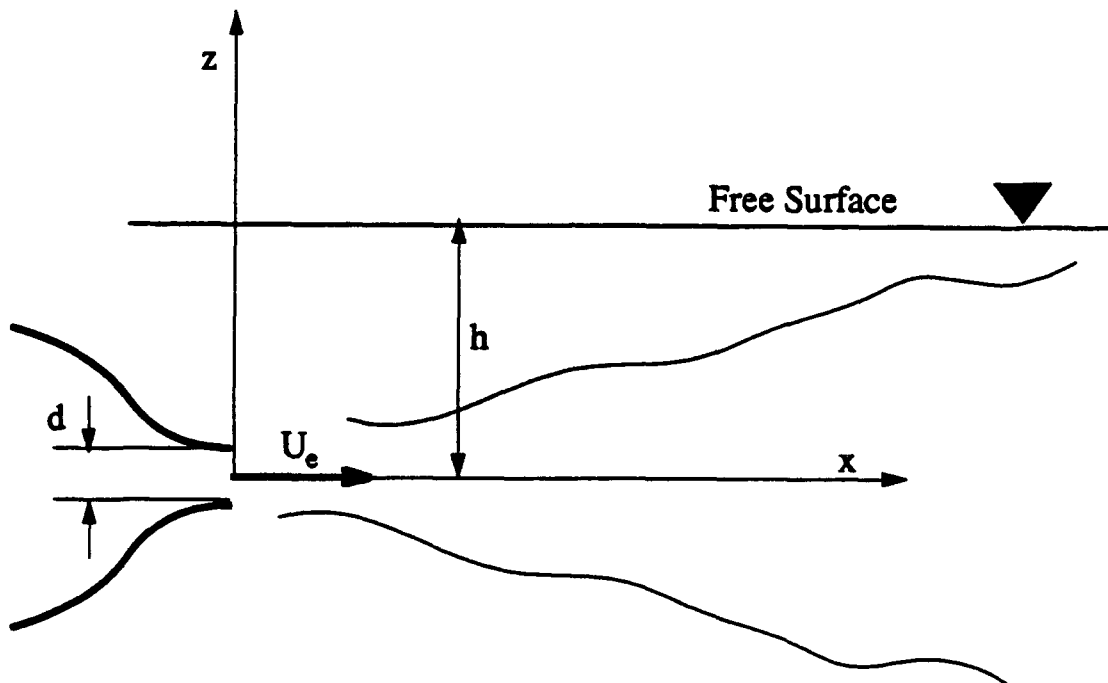


Figure 1.2. Schematic of the flow geometry. The coordinate x is defined as positive downstream, and z is defined as positive toward the free surface. The remaining coordinate, y , is defined so as to give a right-handed system.

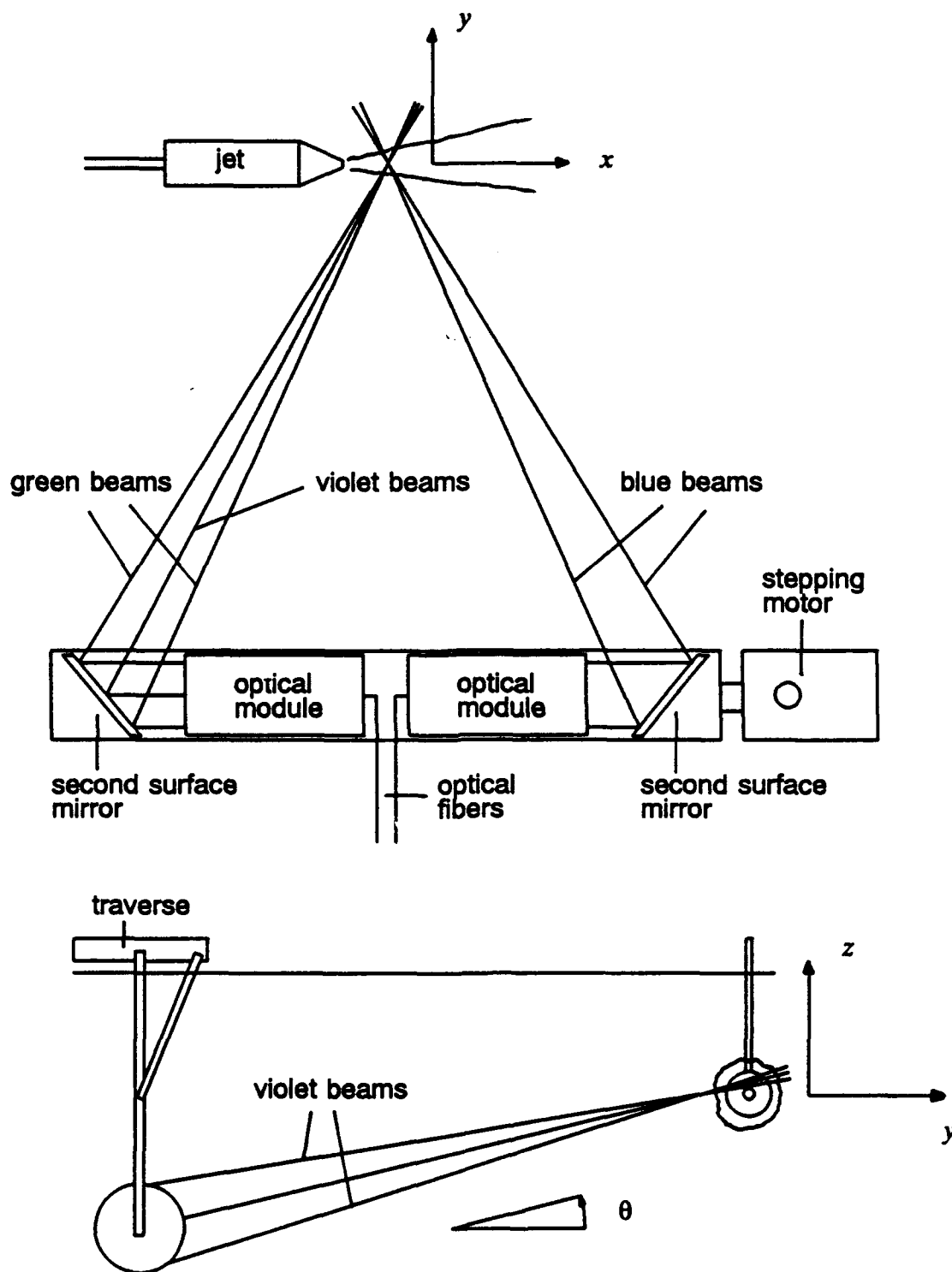


Figure 2.1. Plan and side views of the LDV probe and jet nozzle. The LDV rotates about its axis and translates perpendicular to the jet; the jet translates on its axis.

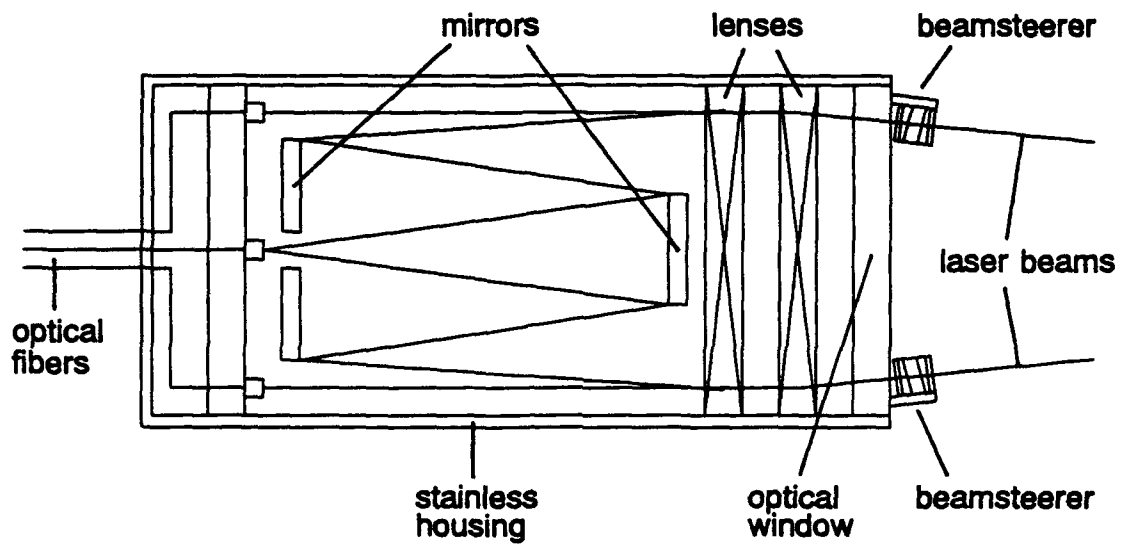


Figure 2.2 Schematic of the single-component underwater LDV module, showing the transmitting and receiving optics.

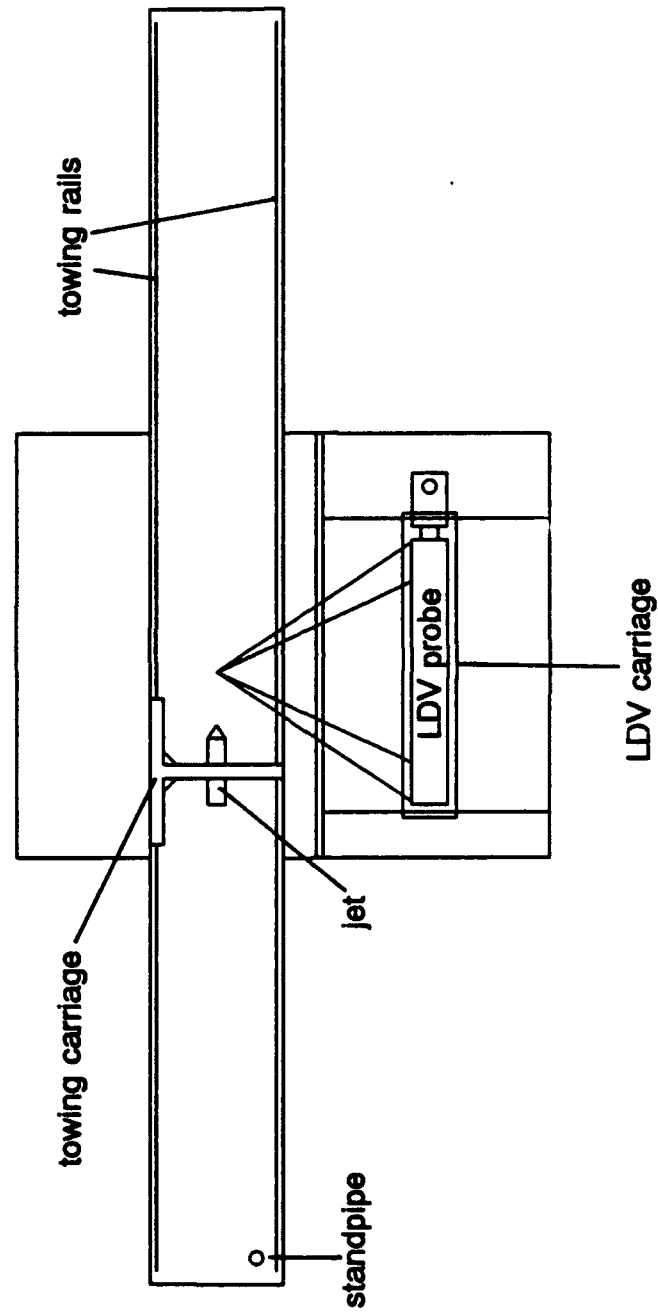


Figure 2.3. Schematic of the towing tank, LDV probe, and jet nozzle.

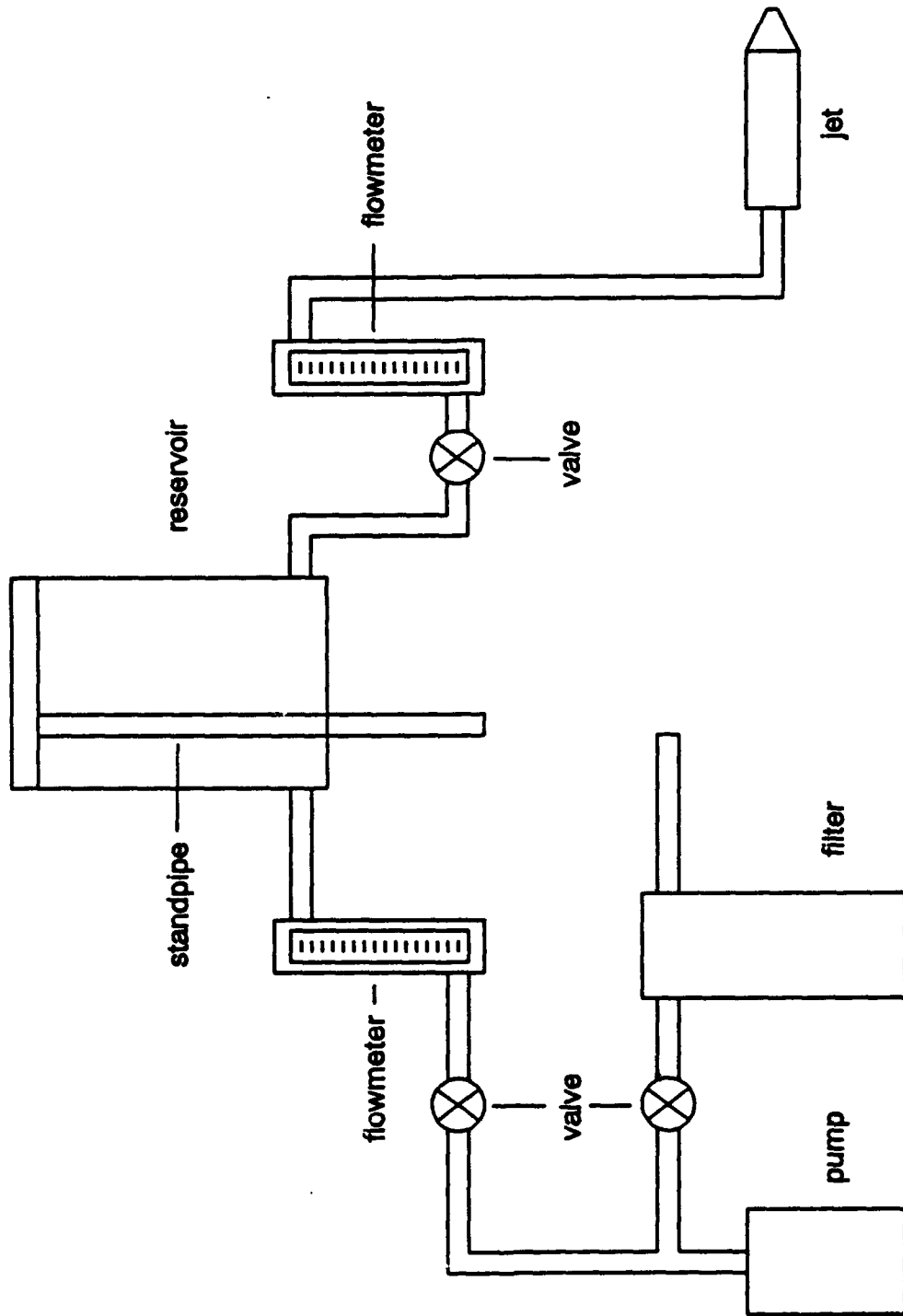


Figure 2.4. Schematic of the flow loop, showing both the jet circuit and the filter circuit.

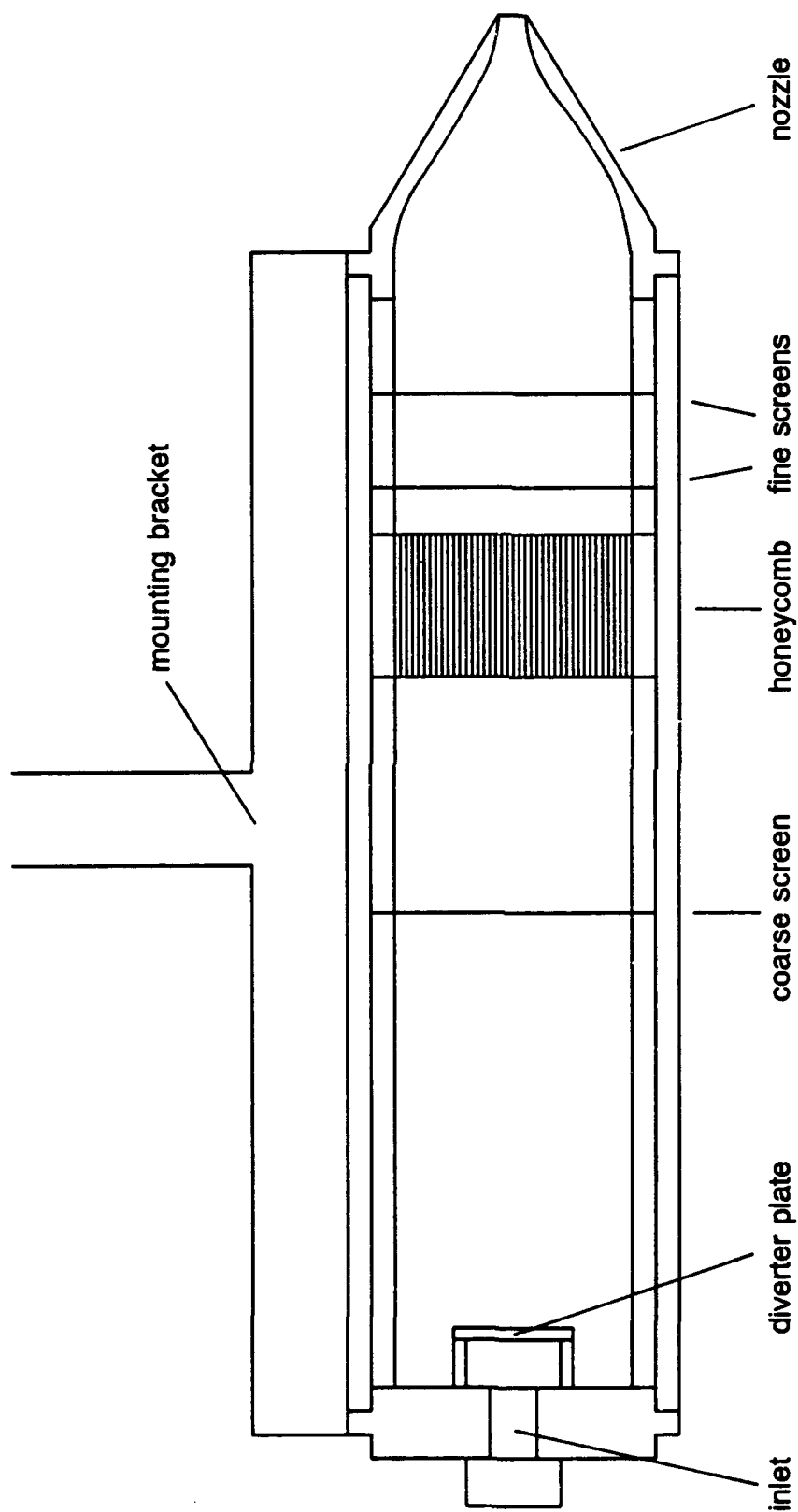


Figure 2.5. Schematic of the jet nozzle and settling chamber. The nozzle profile is a fifth-degree polynomial, having specified diameter and both zero slope and curvature at entry and exit.

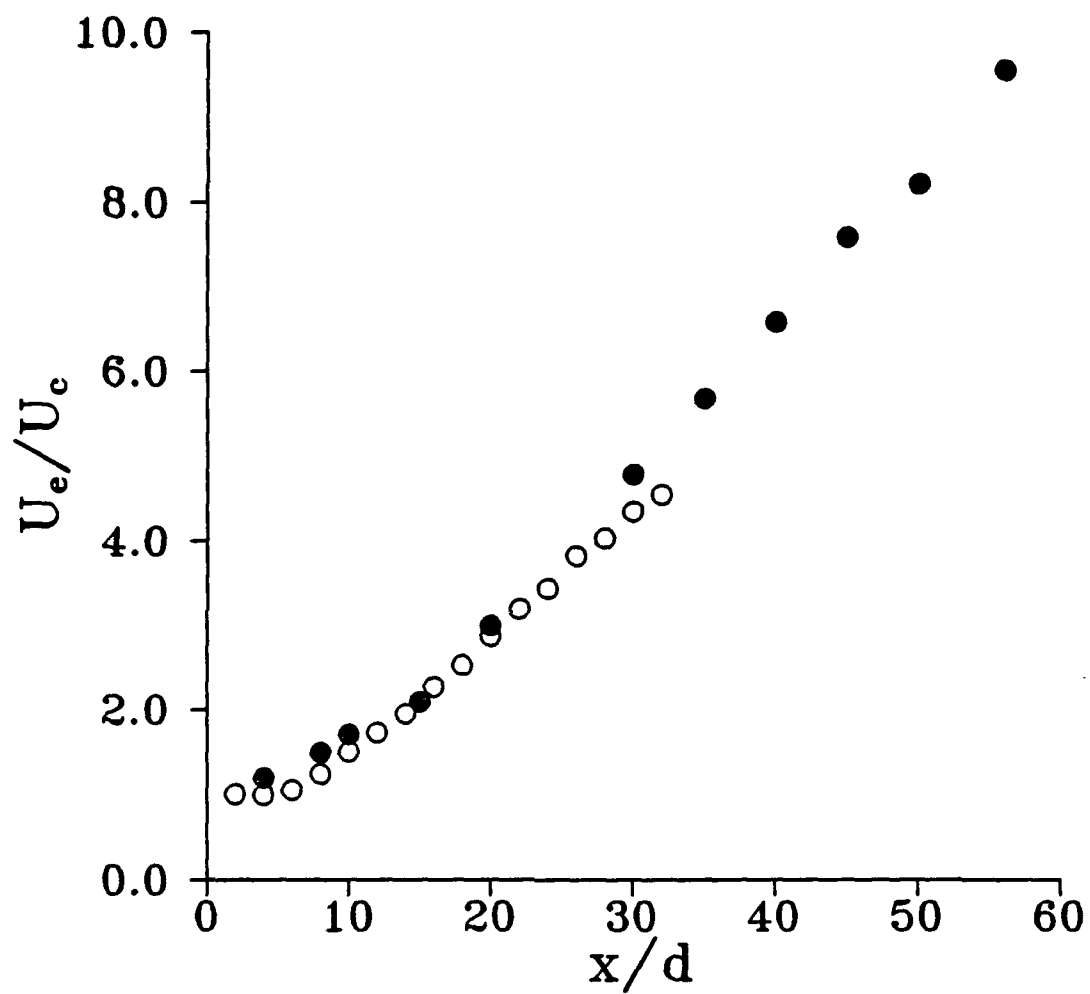


Figure 4.1. Variation of streamwise mean velocity U_e on jet centerline for the deep jet, $h/d=50$. Open symbols are data of the present investigation; solid symbols are data of Wygnanski and Fiedler, 1969.

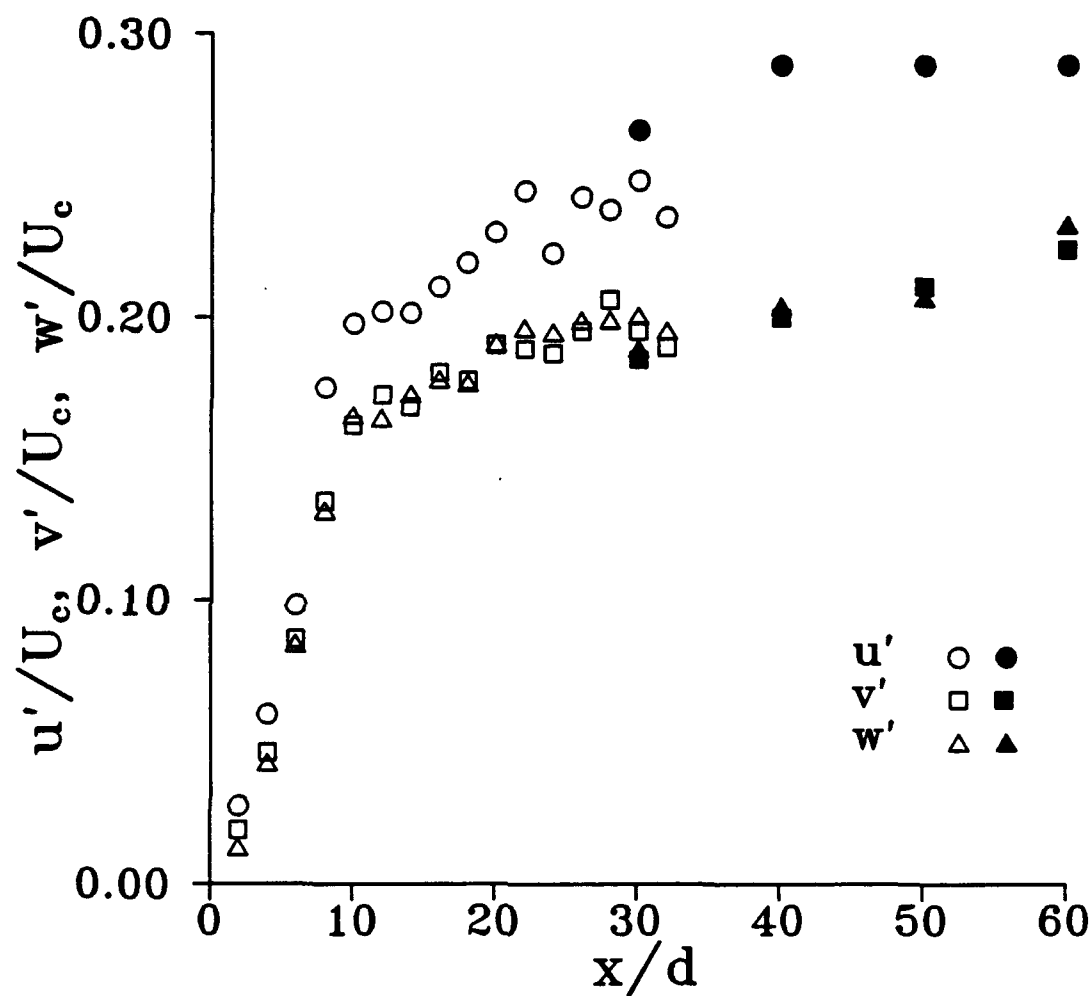


Figure 4.2. Variation of RMS velocity fluctuations on jet centerline for the deep jet, $h/d=50$. Open symbols are data of the present investigation; solid symbols are data of Wygnanski and Fiedler, 1969.

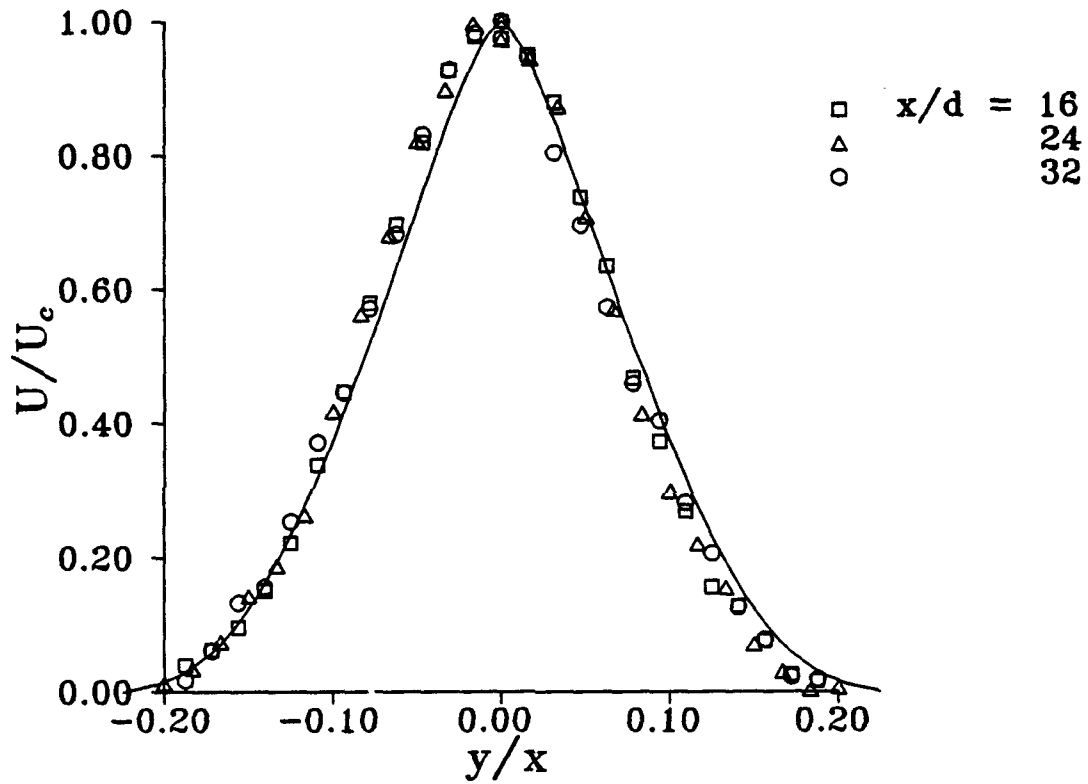


Figure 4.3a. Horizontal profiles of the streamwise mean velocity U/U_c for the deep jet, $h/d \approx 50$, $z/d = 0$. Solid curve is the theoretical solution of Tollmien.

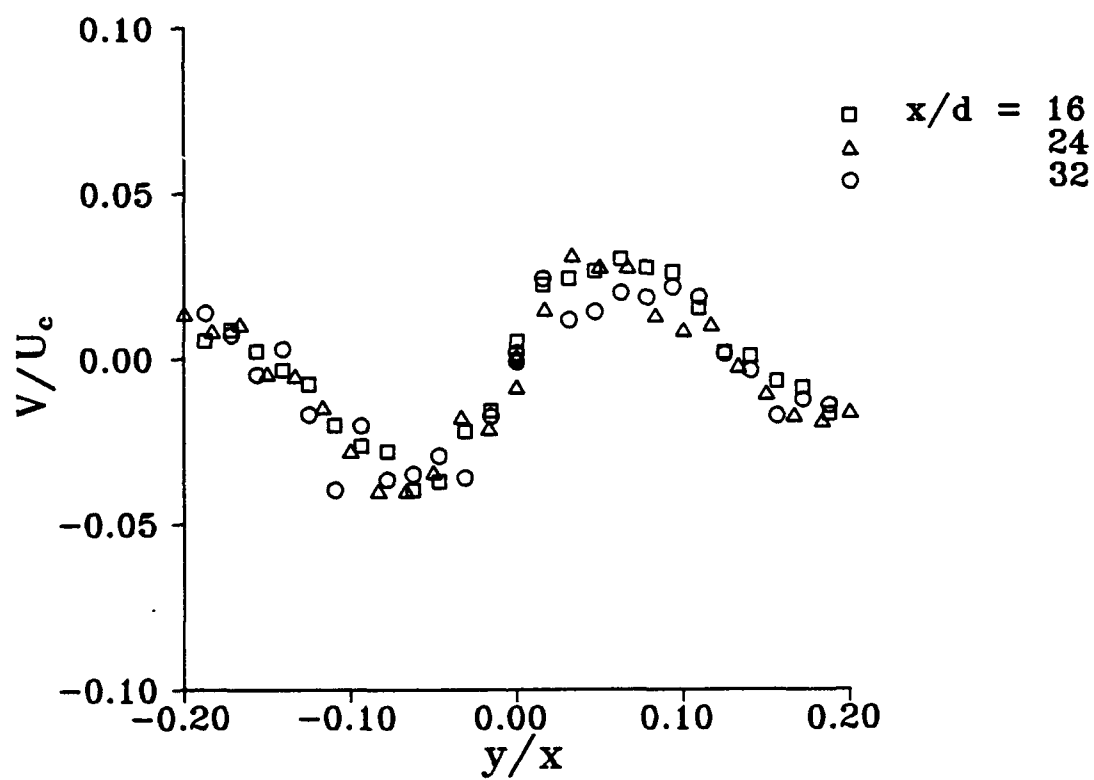


Figure 4.3b. Horizontal profiles of the horizontal mean velocity V/U_c for the deep jet, $h/d=50$, $z/d=0$.

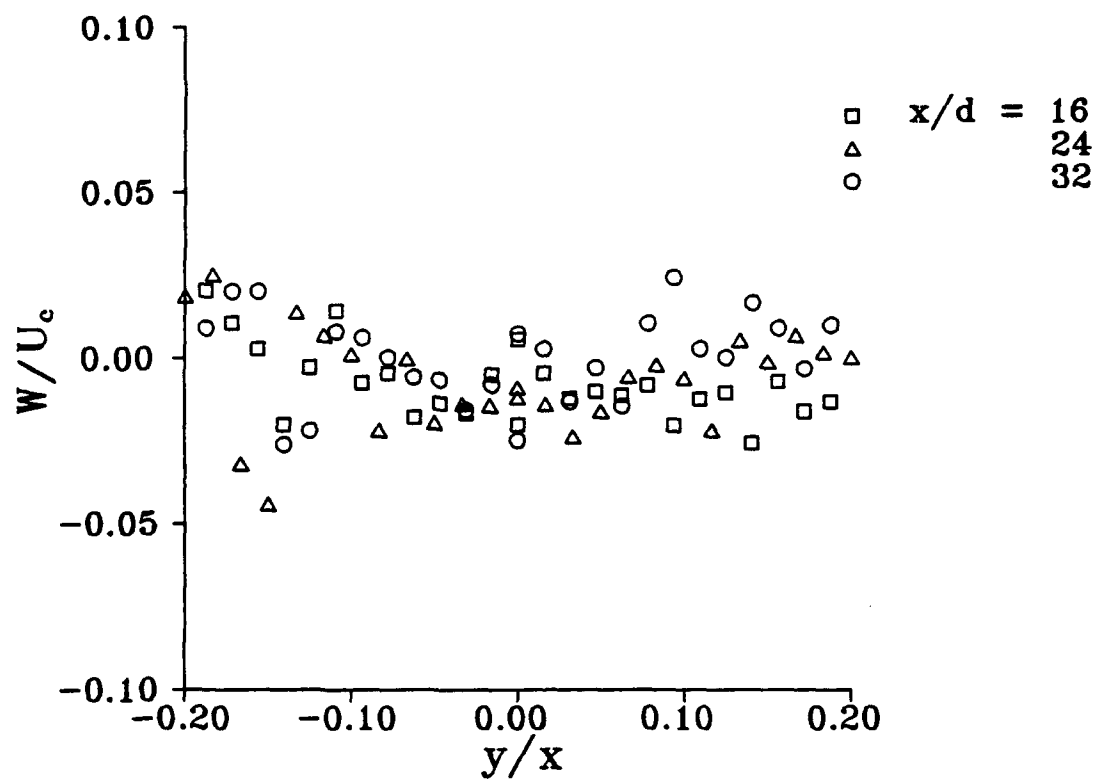


Figure 4.3c. Horizontal profiles of the vertical mean velocity W/U_c for the deep jet, $h/d=50$, $z/d=0$.

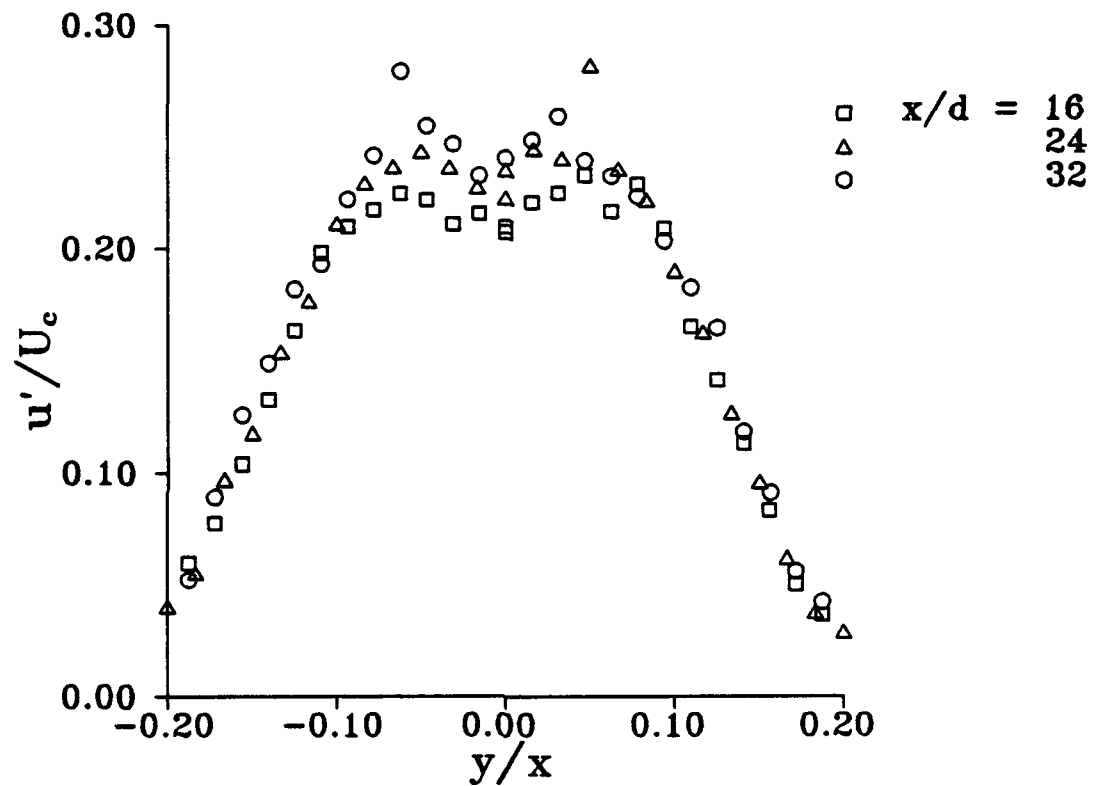


Figure 4.3d. Horizontal profiles of the streamwise RMS velocity fluctuations u'/U_c for the deep jet, $h/d=50$, $z/d=0$.

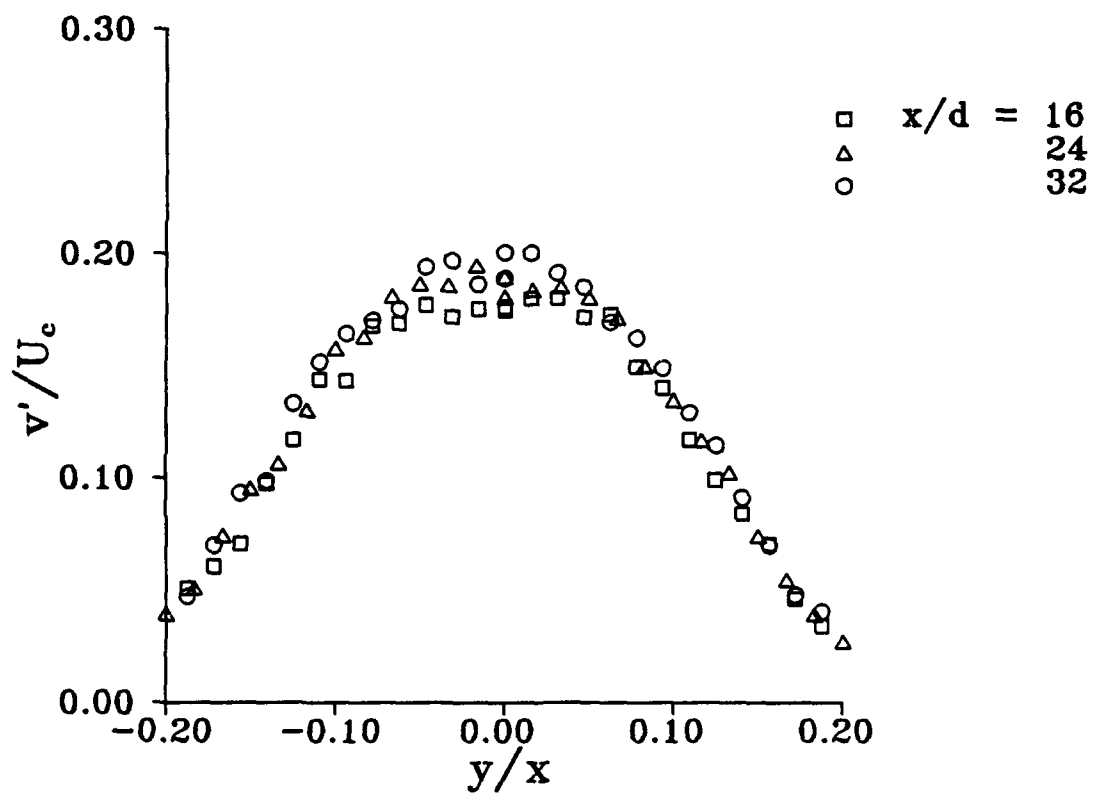


Figure 4.3e. Horizontal profiles of the horizontal RMS velocity fluctuations v'/U_c for the deep jet, $h/d=50$, $z/d=0$.

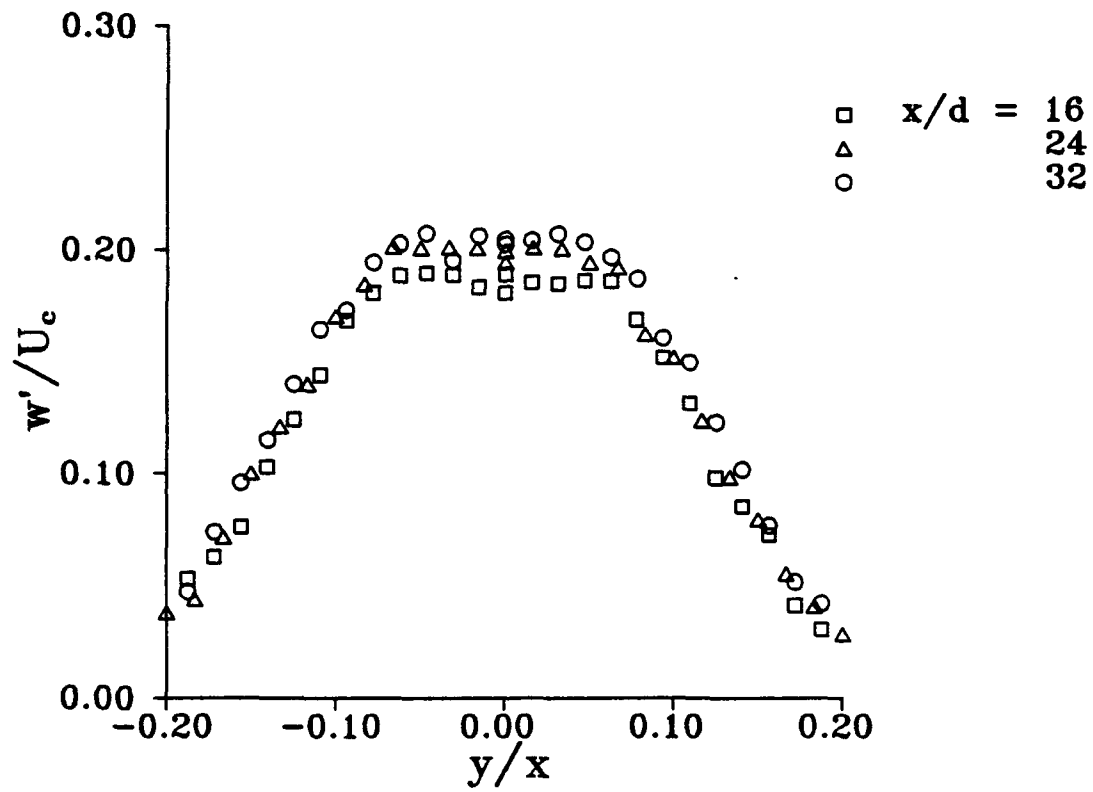


Figure 4.3f. Horizontal profiles of the vertical RMS velocity fluctuations w'/U_c for the deep jet, $h/d=50$, $z/d=0$.

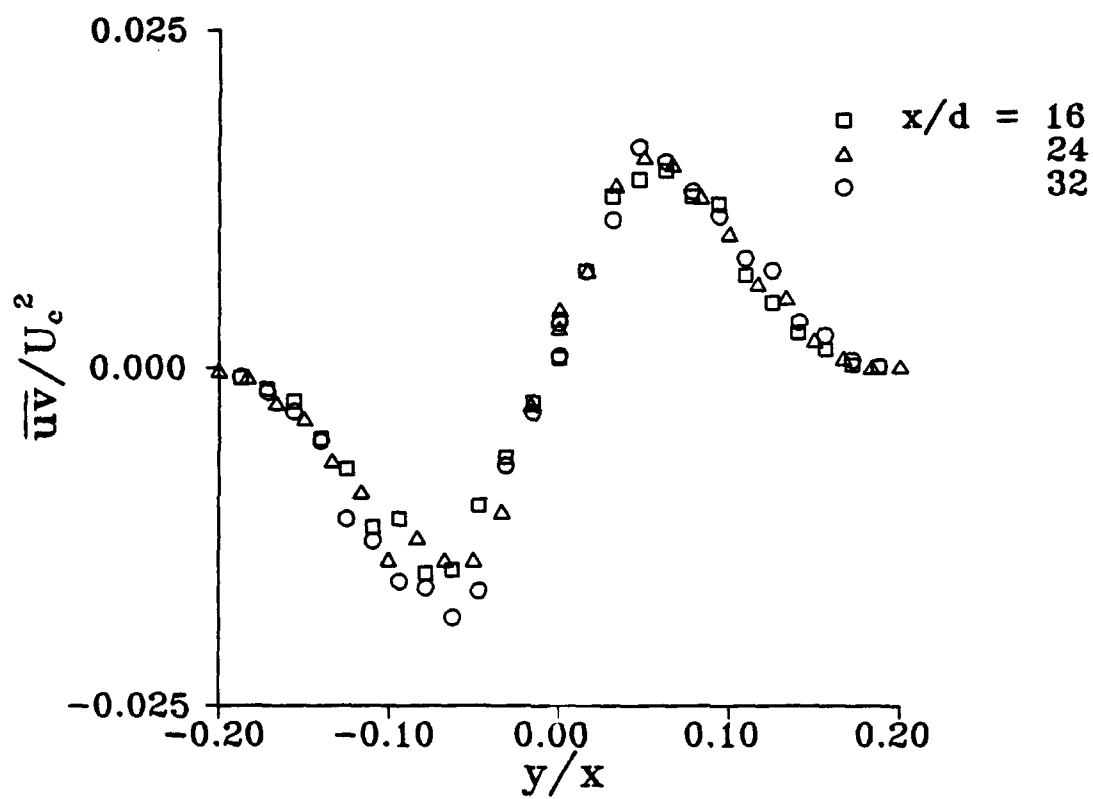


Figure 4.3g. Horizontal profiles of the Reynolds stress \overline{uv}/U_c^2 for the deep jet, $h/d=50$, $z/d=0$.

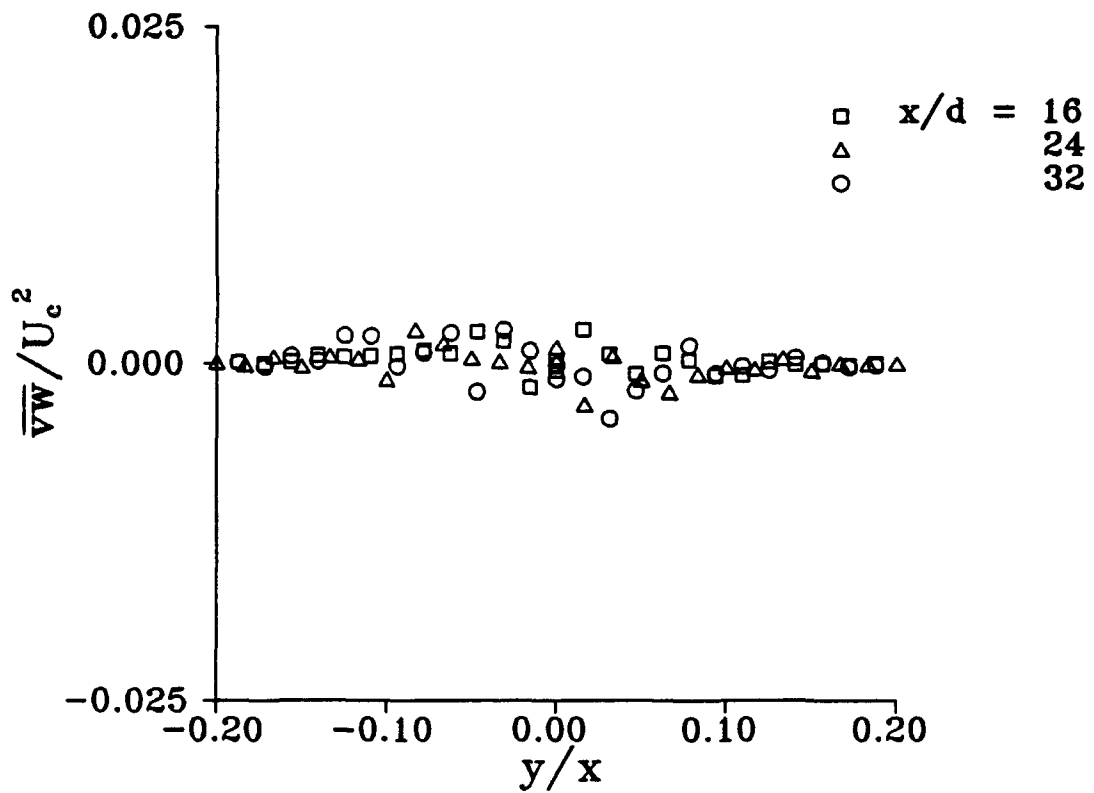


Figure 4.3h. Horizontal profiles of the Reynolds stress \overline{vw}/U_c^2 for the deep jet, $h/d=50$, $z/d=0$.

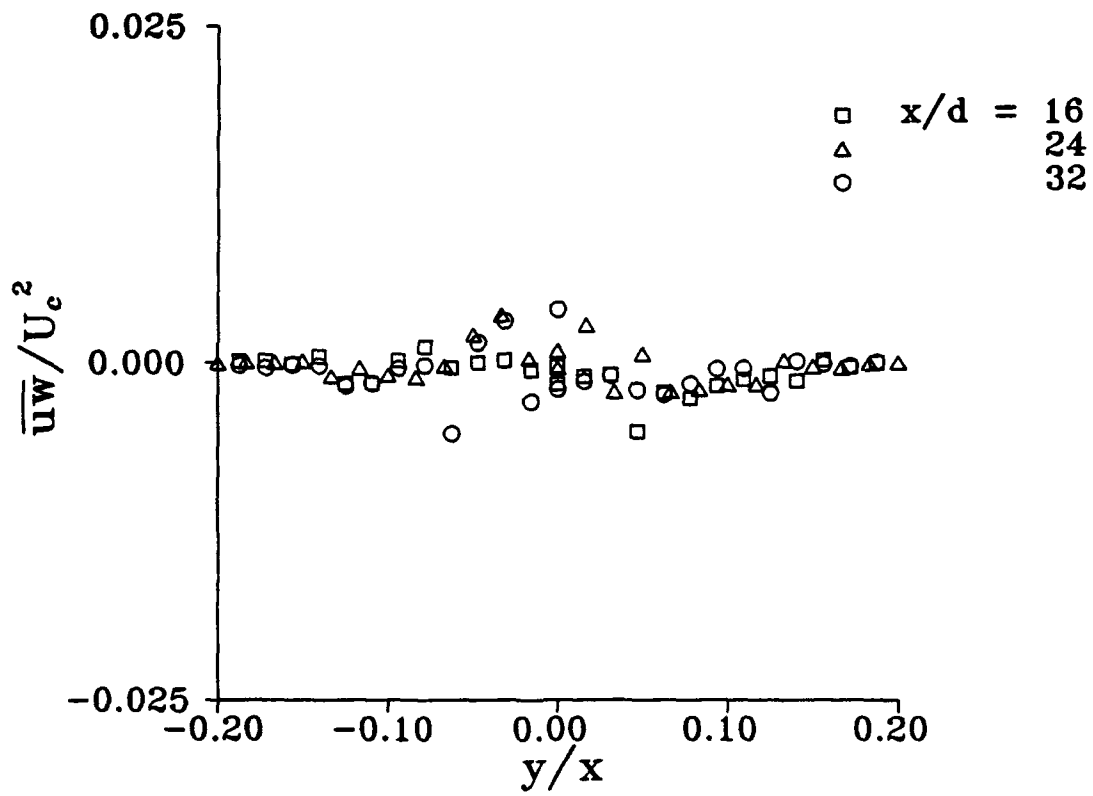


Figure 4.3i. Horizontal profiles of the Reynolds stress \overline{uw}/U_c^2 for the deep jet, $h/d=50$, $z/d=0$.

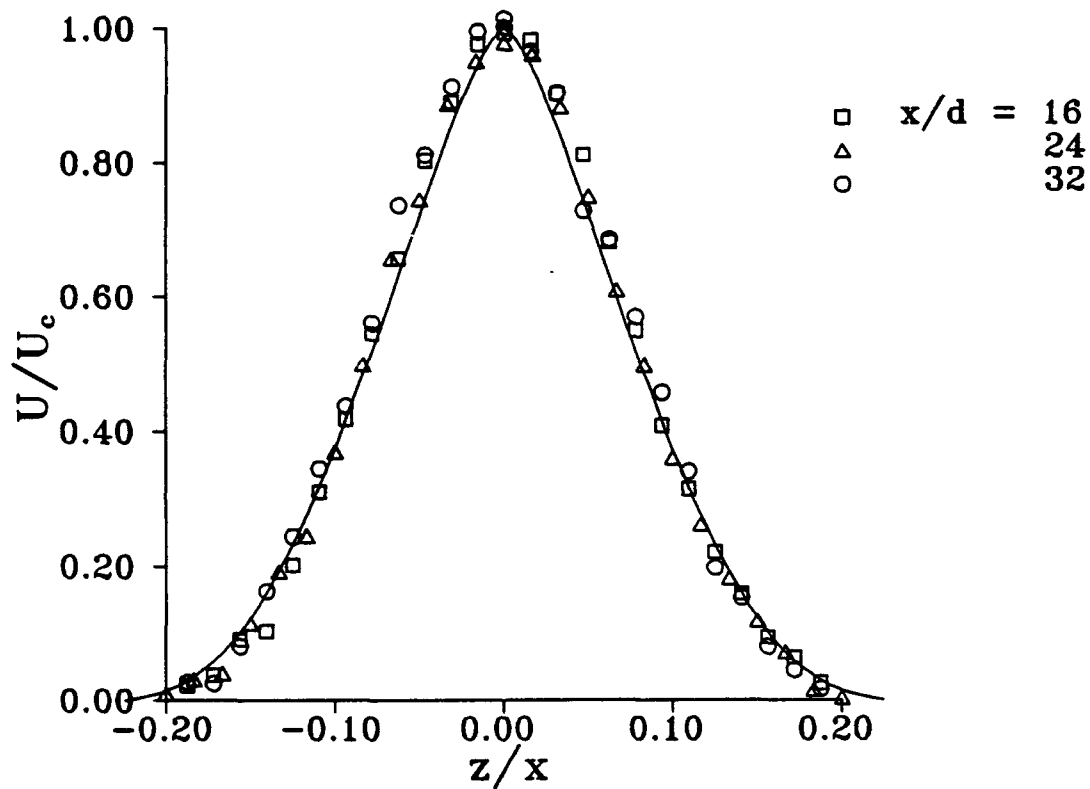


Figure 4.4a. Vertical profiles of the streamwise mean velocity U/U_c for the deep jet, $h/d=50$, $y/d=0$. Solid curve is the theoretical solution of Tollmien.

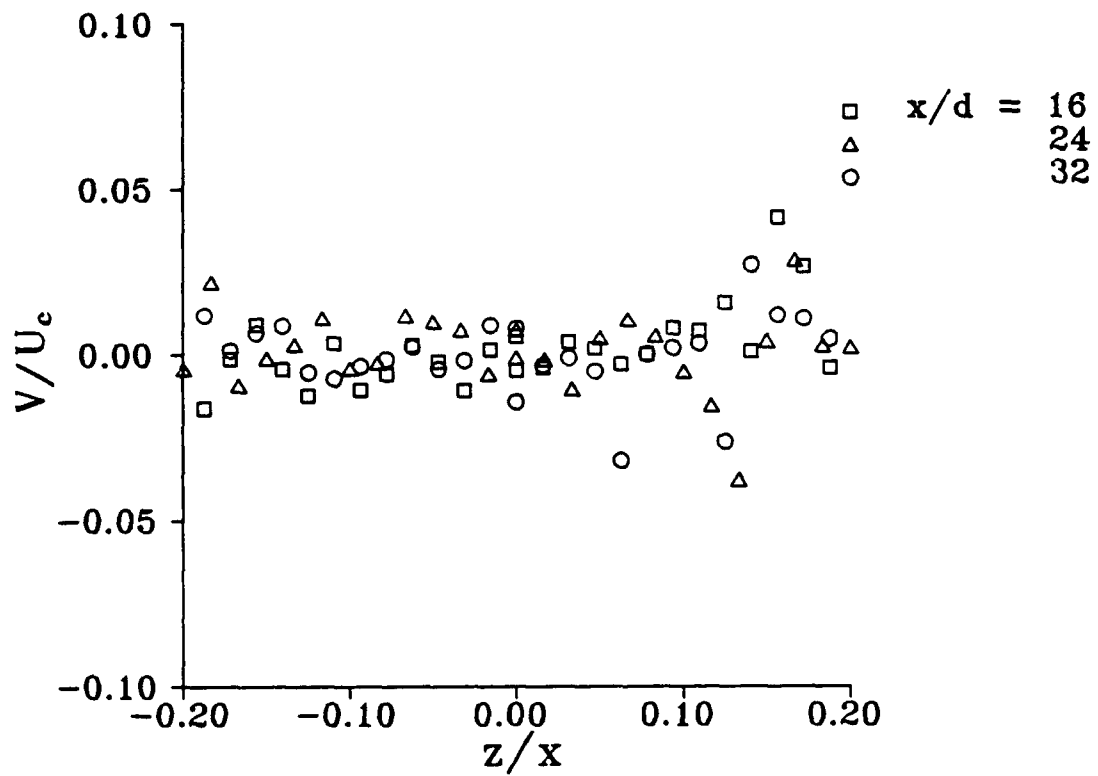


Figure 4.4b. Vertical profiles of the horizontal mean velocity V/U_e for the deep jet, $h/d=50$, $y/d=0$.

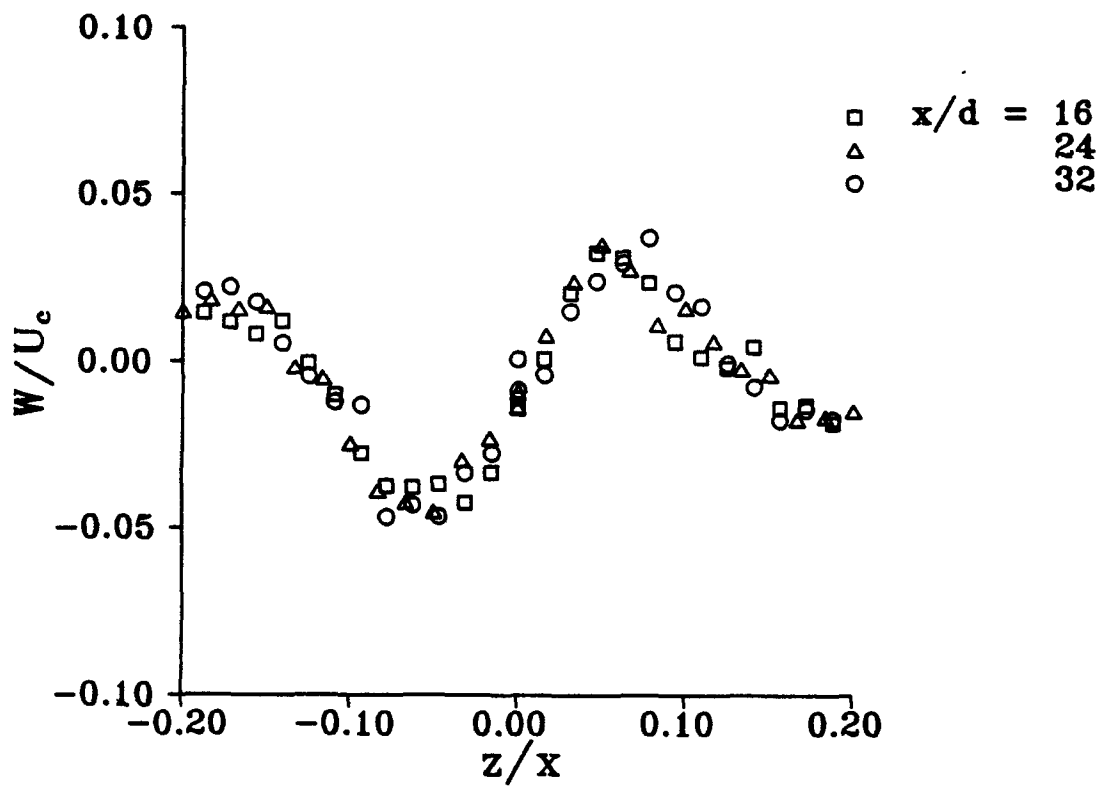


Figure 4.4c. Vertical profiles of the vertical mean velocity W/U_c for the deep jet, $h/d=50$, $y/d=0$.

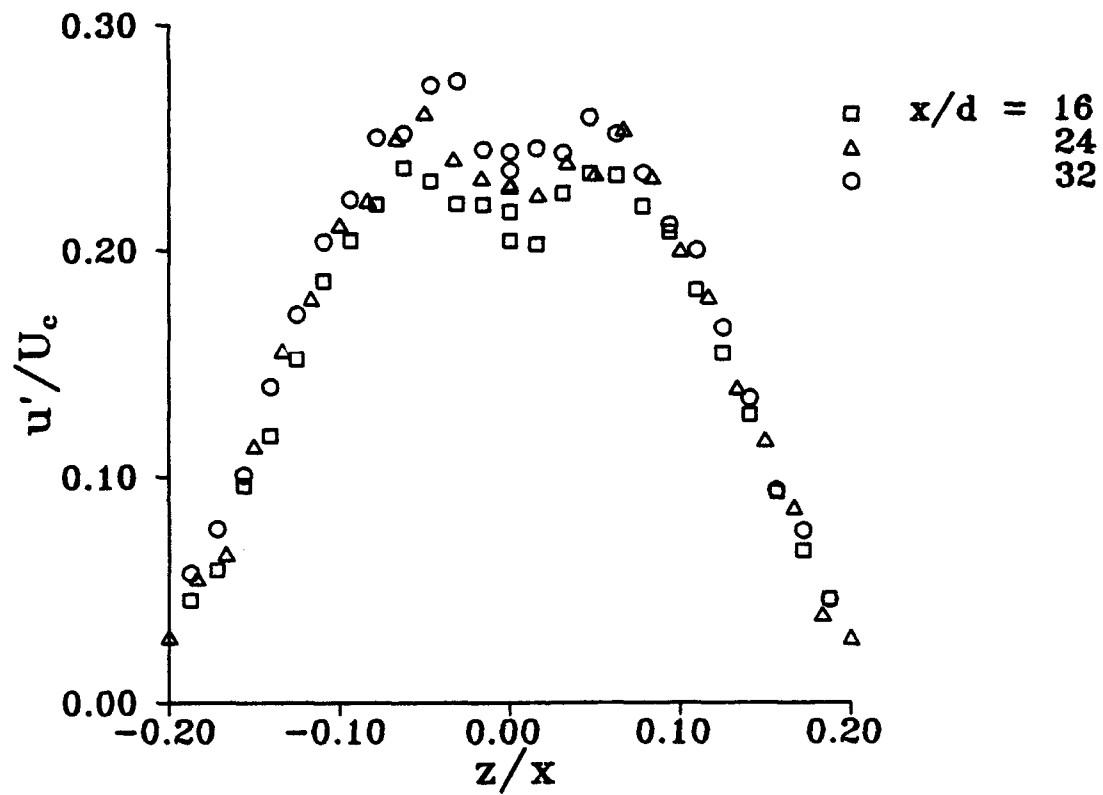


Figure 4.4d. Vertical profiles of the streamwise RMS velocity fluctuations u'/U_c for the deep jet, $h/d=50$, $y/d=0$.

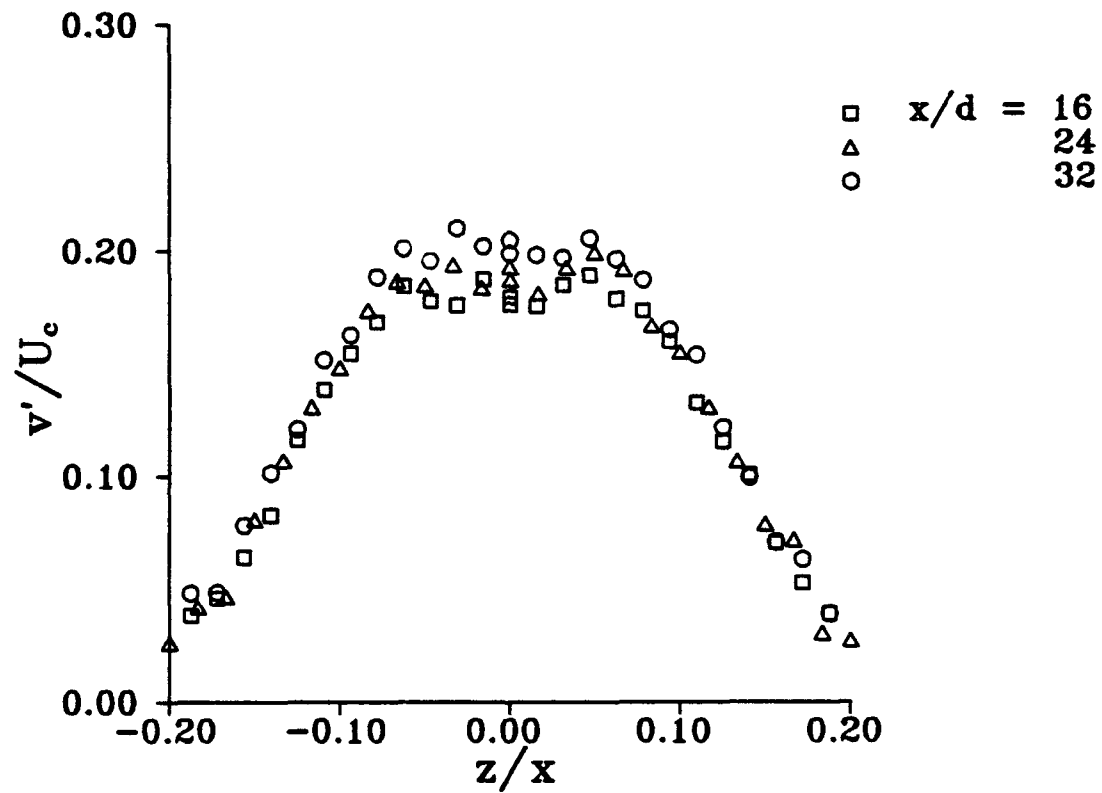


Figure 4.4e. Vertical profiles of the horizontal RMS velocity fluctuations v'/U_c for the deep jet, $h/d=50$, $y/d=0$.

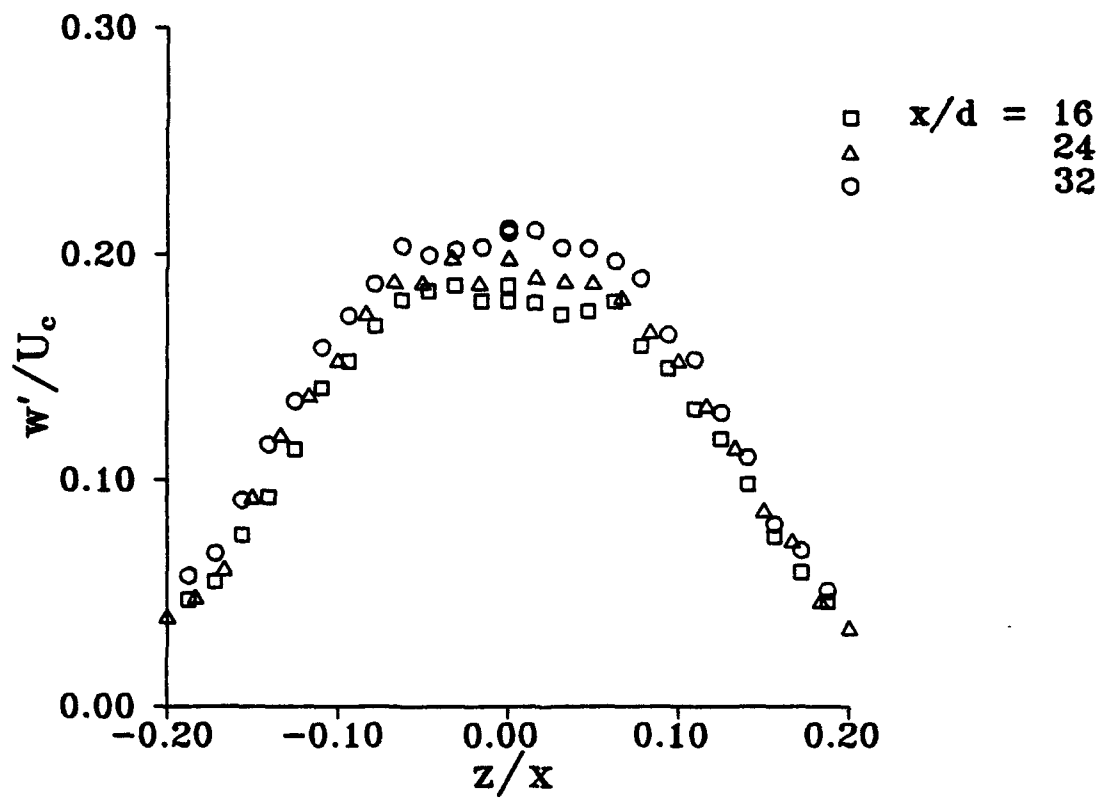


Figure 4.4f. Vertical profiles of the vertical RMS velocity fluctuations w'/U_c for the deep jet, $h/d \sim 50$, $y/d = 0$.

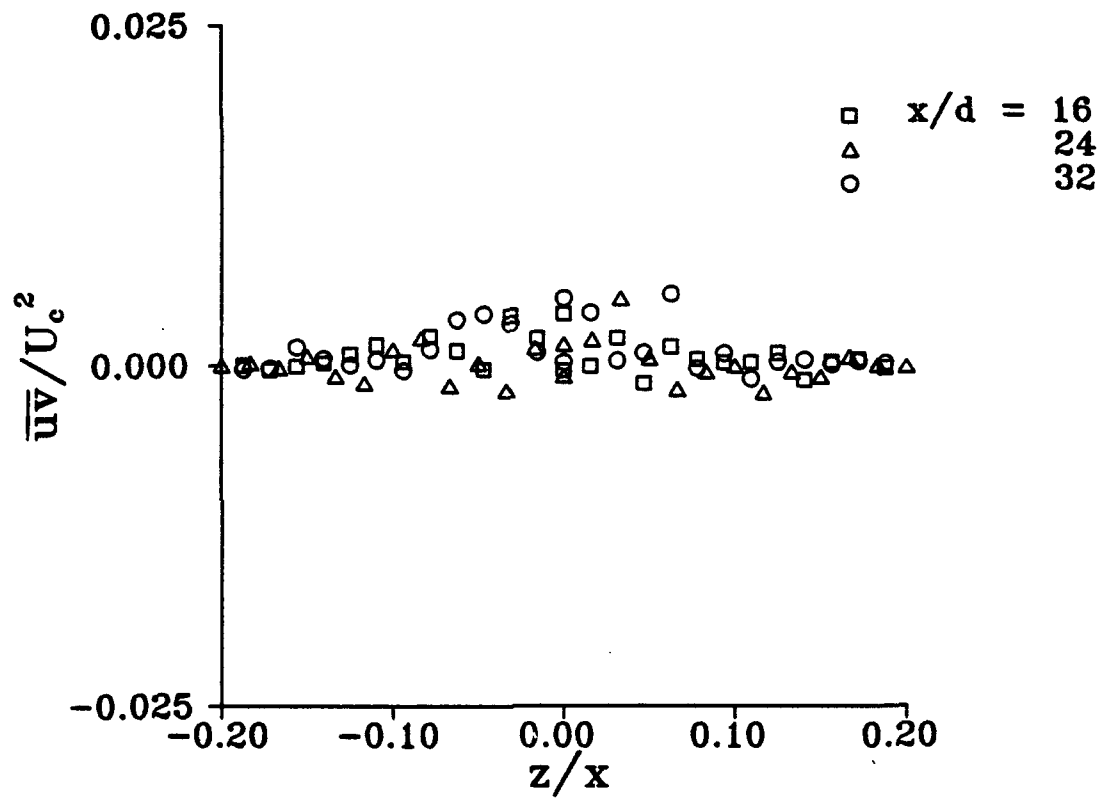


Figure 4.4g. Vertical profiles of the Reynolds stress \overline{uv}/U_c^2 for the deep jet, $h/d=50$, $y/d=0$.

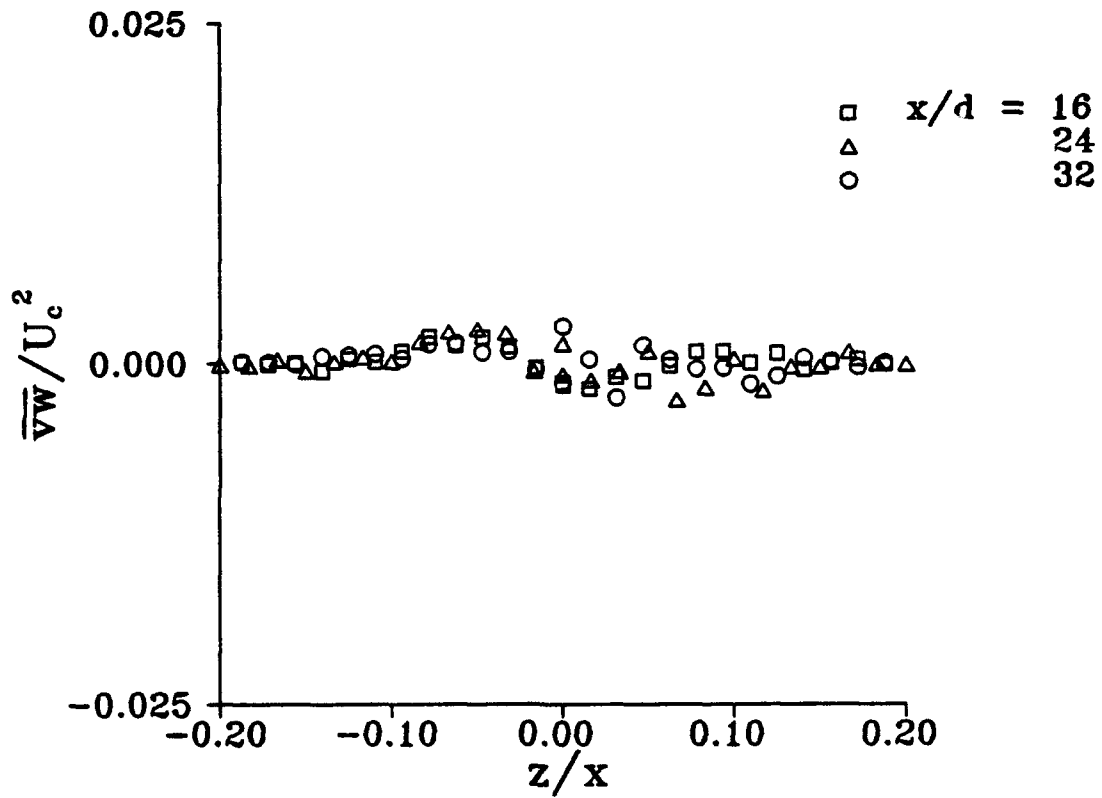


Figure 4.4h. Vertical profiles of the Reynolds stress \overline{vw}/U_c^2 for the deep jet, $h/d=50$, $y/d=0$.

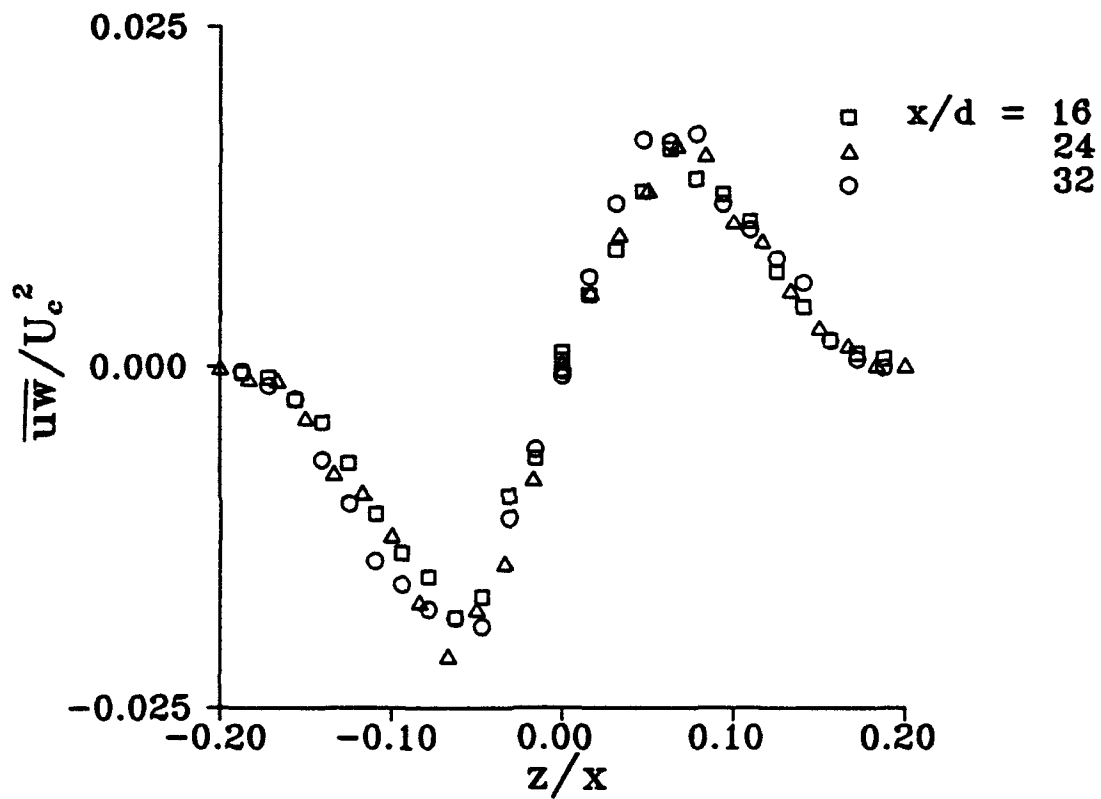


Figure 4.4i. Vertical profiles of the Reynolds stress \overline{uw}/U_c^2 for the deep jet, $h/d=50$, $y/d=0$.

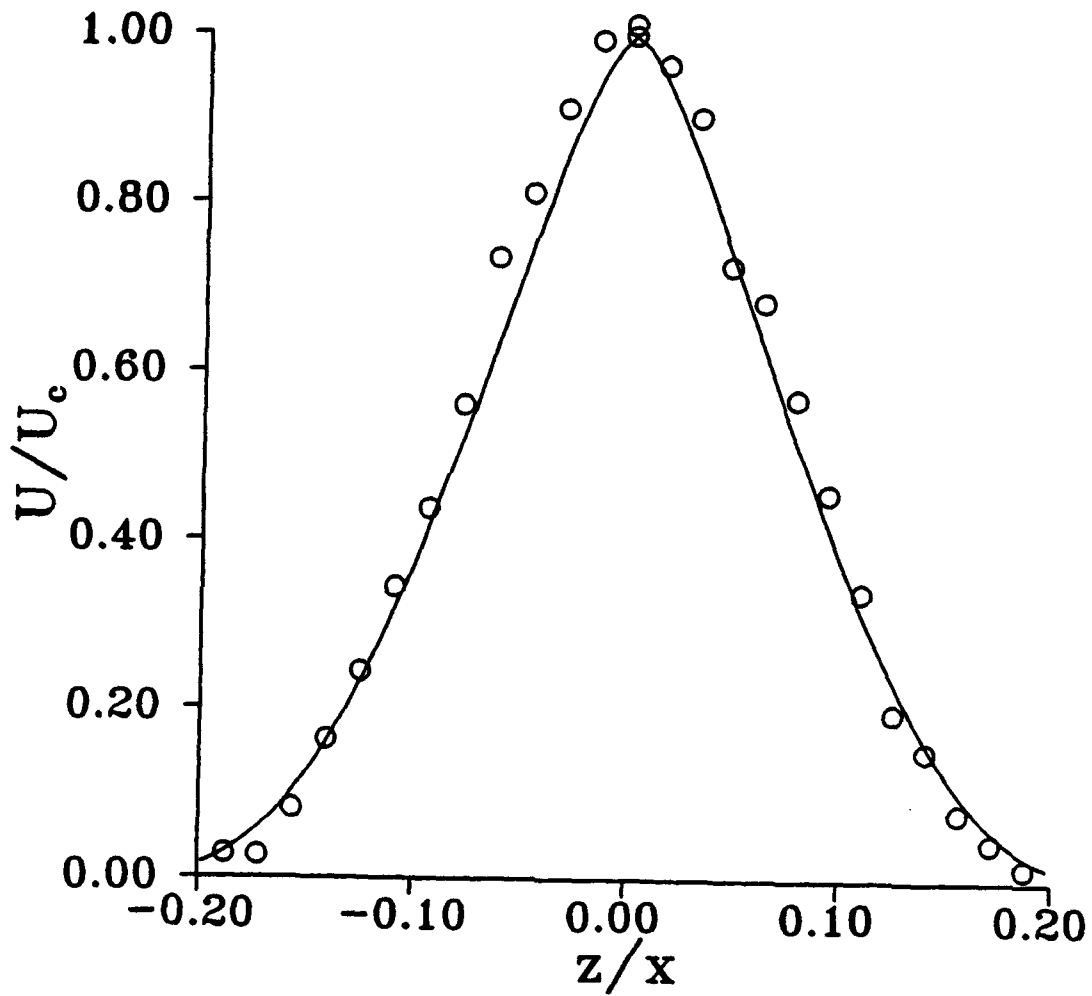


Figure 4.5a. Vertical profile of the streamwise mean velocity at $x/d=32$ for the deep jet, $h/d=50$, $y/d=0$. Solid curve is the theoretical solution of Tollmien.

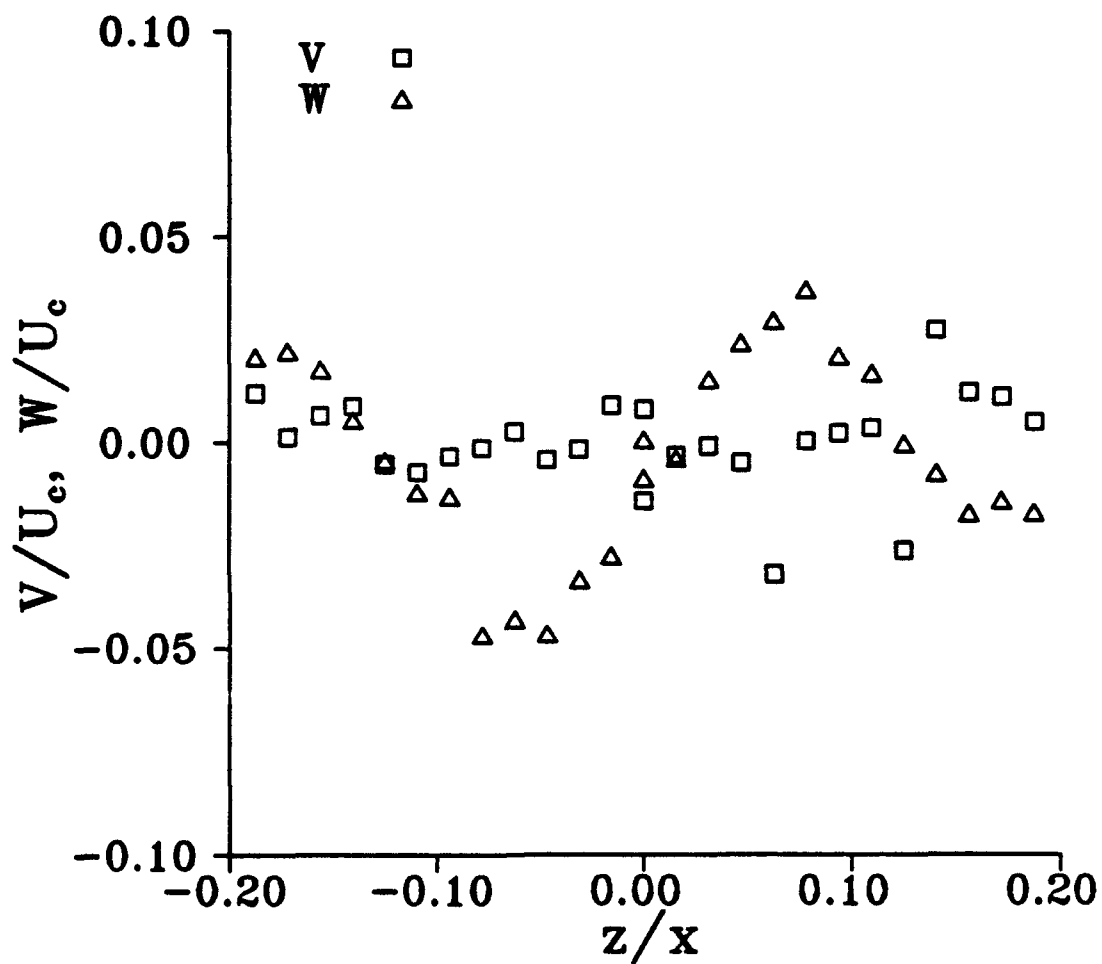


Figure 4.5b. Vertical profiles of the horizontal and vertical mean velocities at $x/d=32$ for the deep jet, $h/d=50$, $y/d=0$.

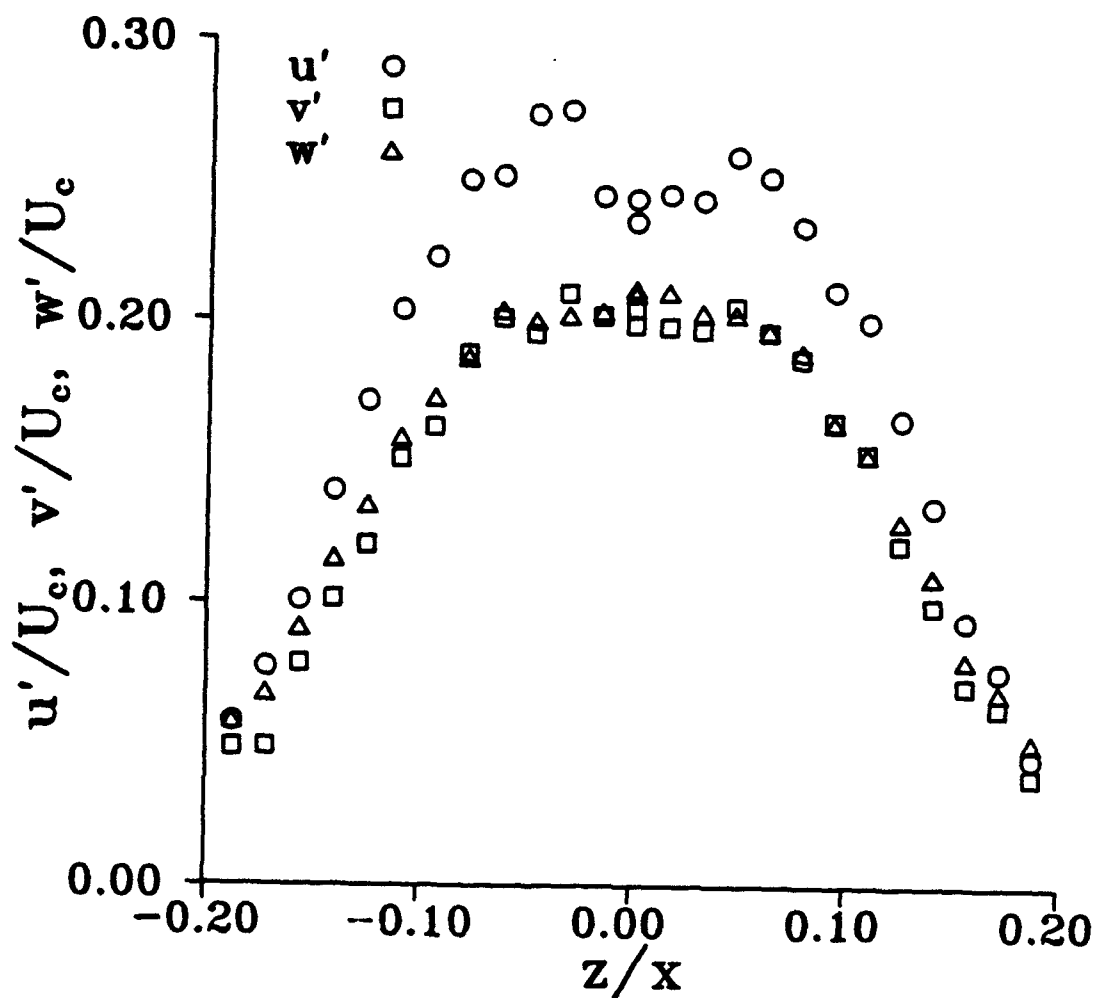


Figure 4.5c. Vertical profiles of the RMS velocity fluctuations at $x/d=32$ for the deep jet, $h/d=50$, $y/d=0$.

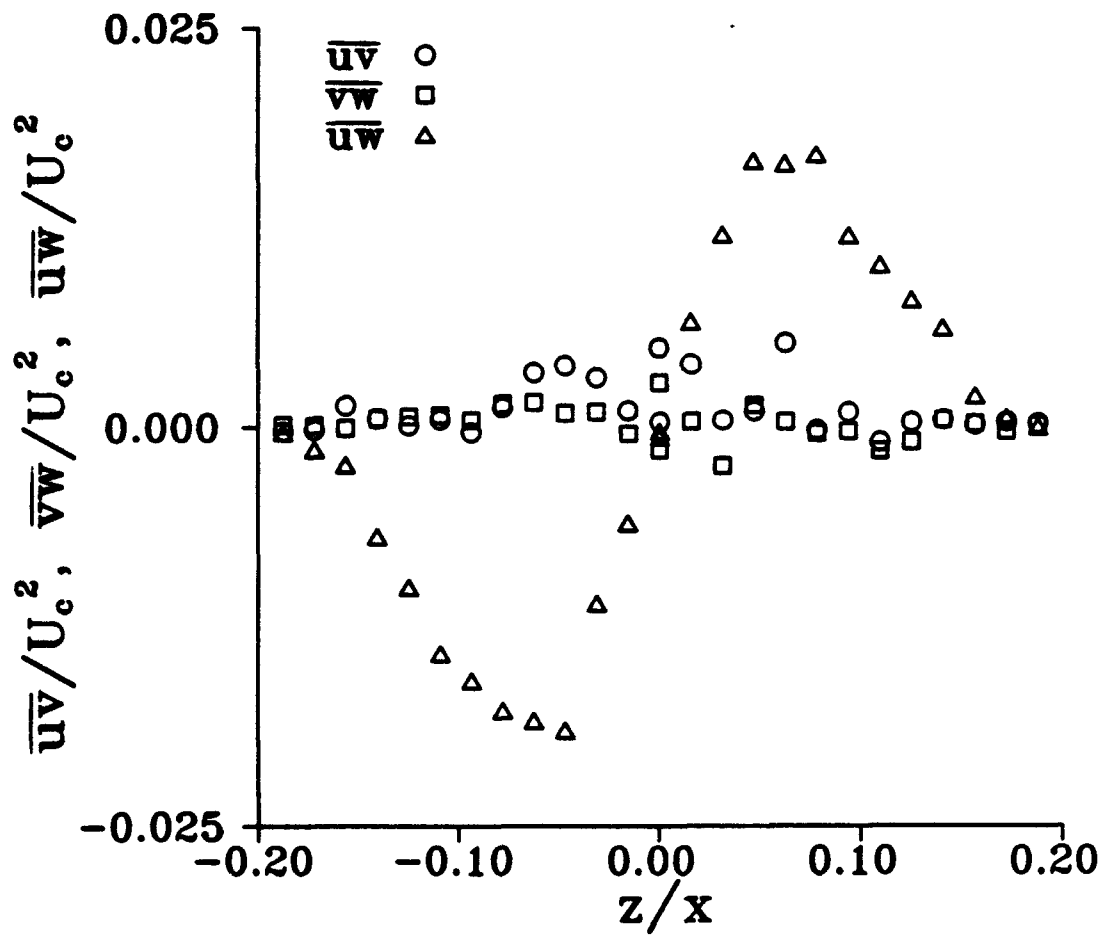


Figure 4.5d. Vertical profiles of the Reynolds stresses at $x/d=32$ for the deep jet, $h/d=50$, $y/d=0$.

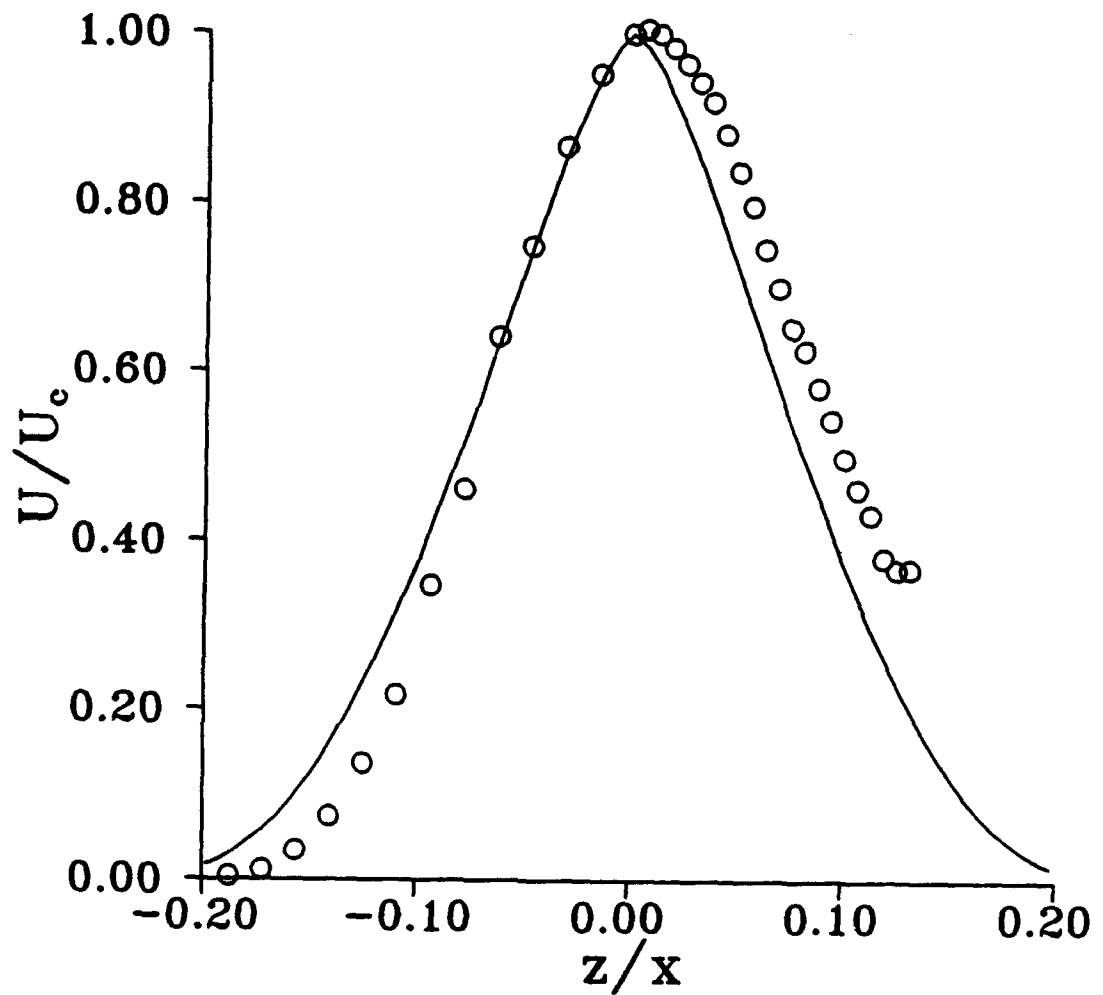


Figure 4.6a. Vertical profile of the streamwise mean velocity at $x/d=16$ for the shallow jet, $h/d=2$, $y/d=0$. Solid curve is the theoretical free jet solution of Tollmien.

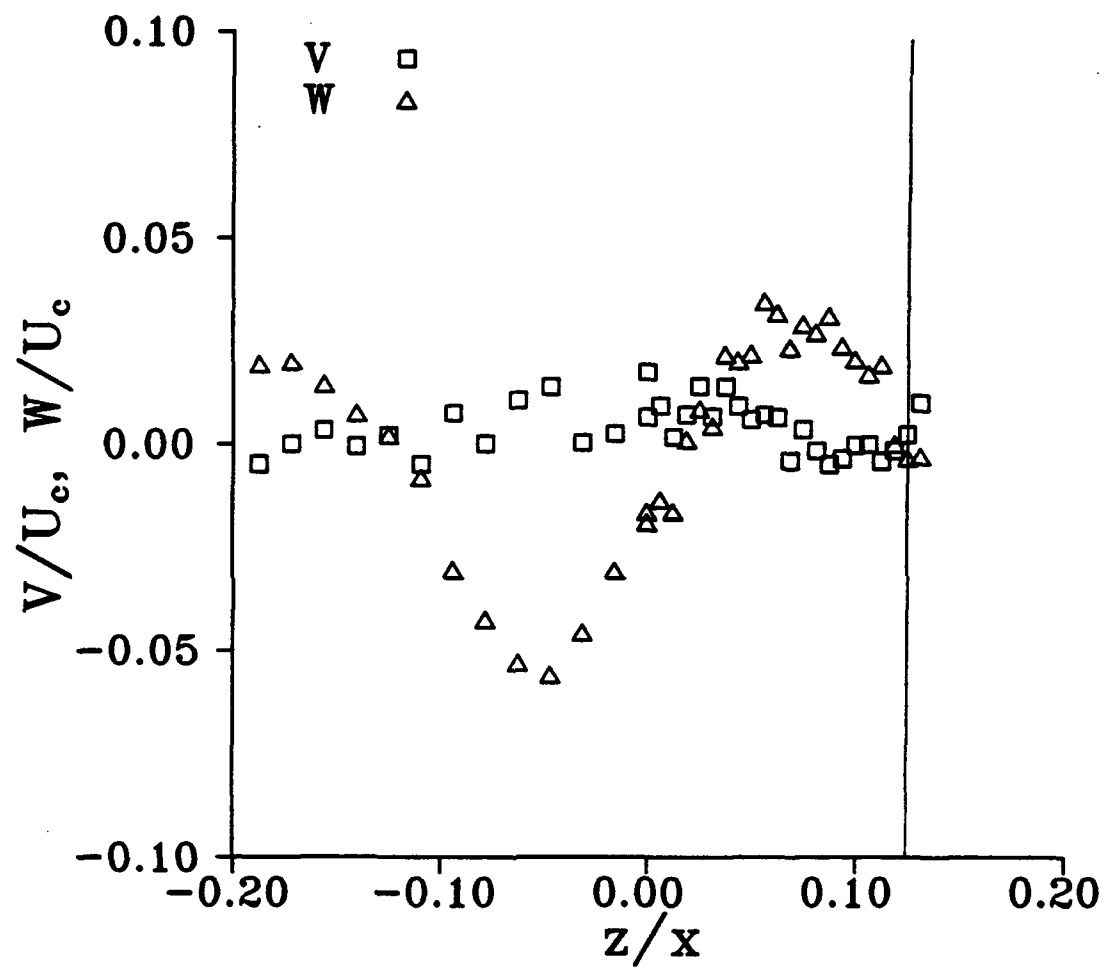


Figure 4.6b. Vertical profiles of the horizontal and vertical mean velocities at $x/d=16$ for the shallow jet, $h/d=2$, $y/d=0$.

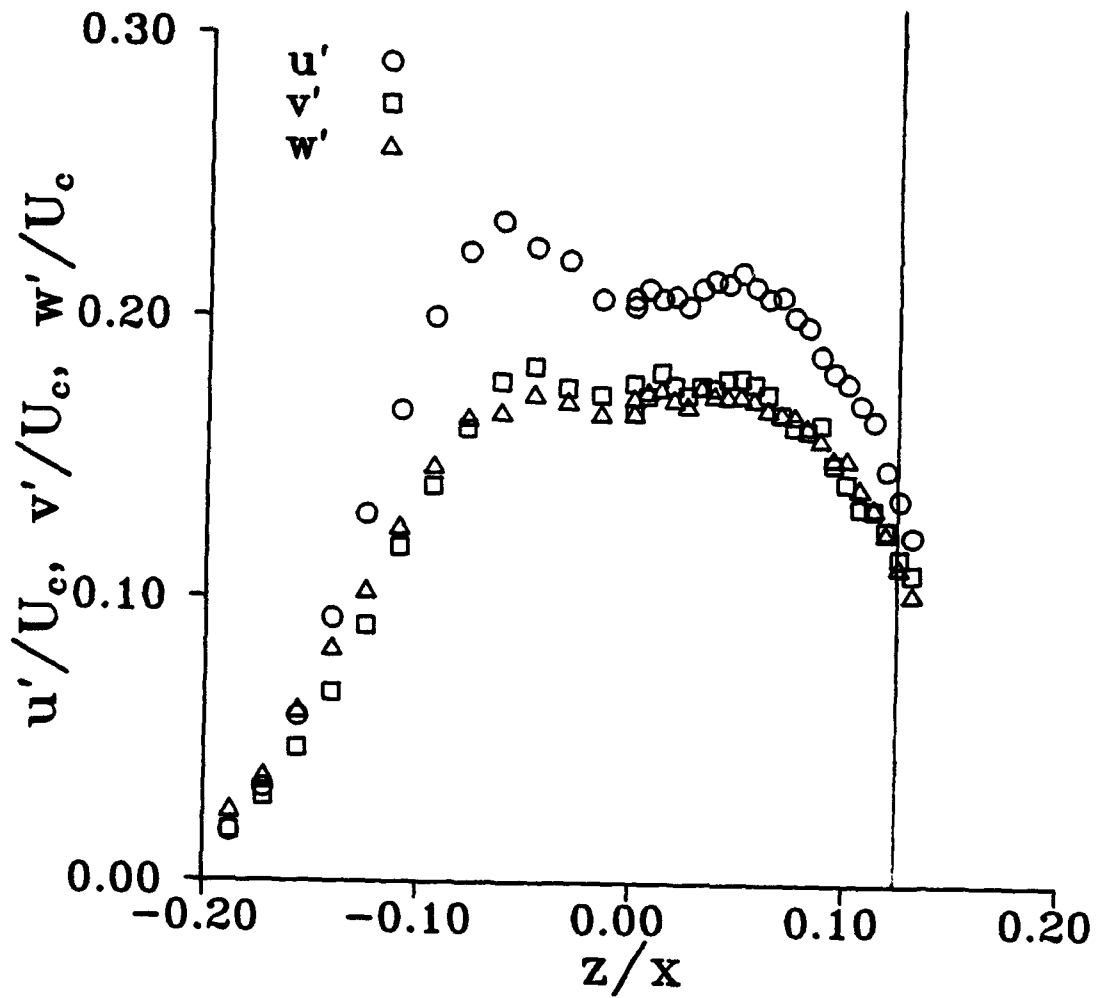


Figure 4.6c. Vertical profiles of the RMS velocity fluctuations at $x/d=16$ for the shallow jet, $h/d=2$, $y/d=0$.

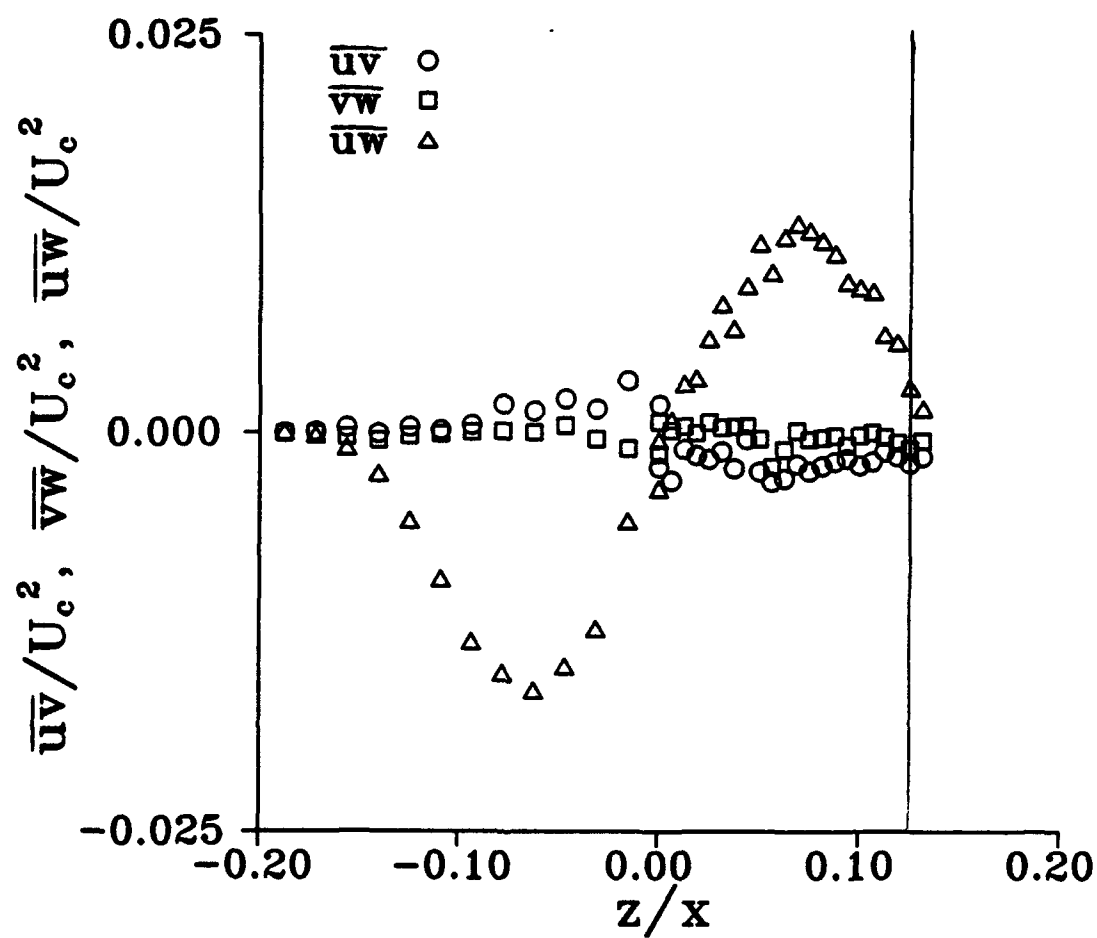


Figure 4.6d. Vertical profiles of the Reynolds stresses at $x/d=16$ for the shallow jet, $h/d=2$, $y/d=0$.

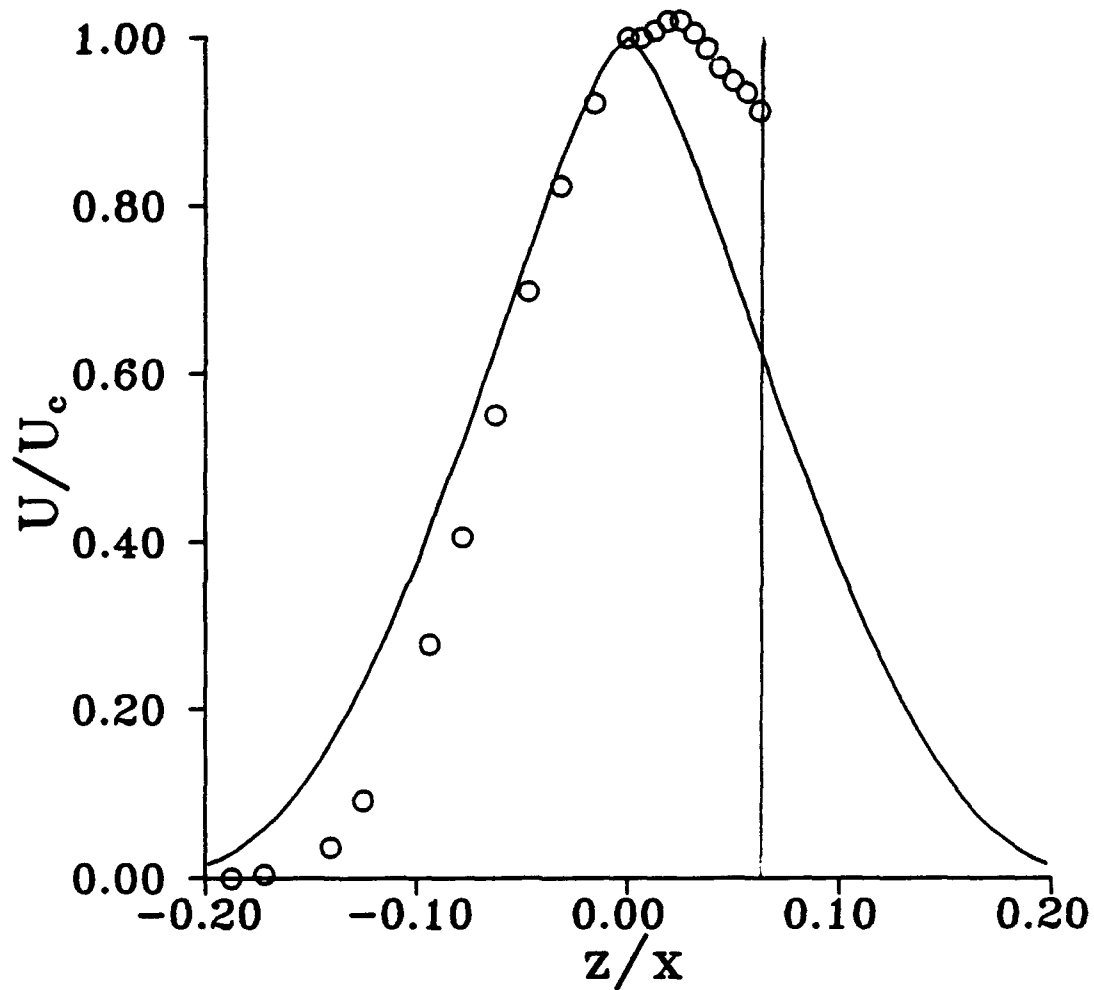


Figure 4.7a. Vertical profile of the streamwise mean velocity at $x/d=32$ for the shallow jet, $h/d=2$, $y/d=0$. Solid curve is the theoretical free jet solution of Tollmien.

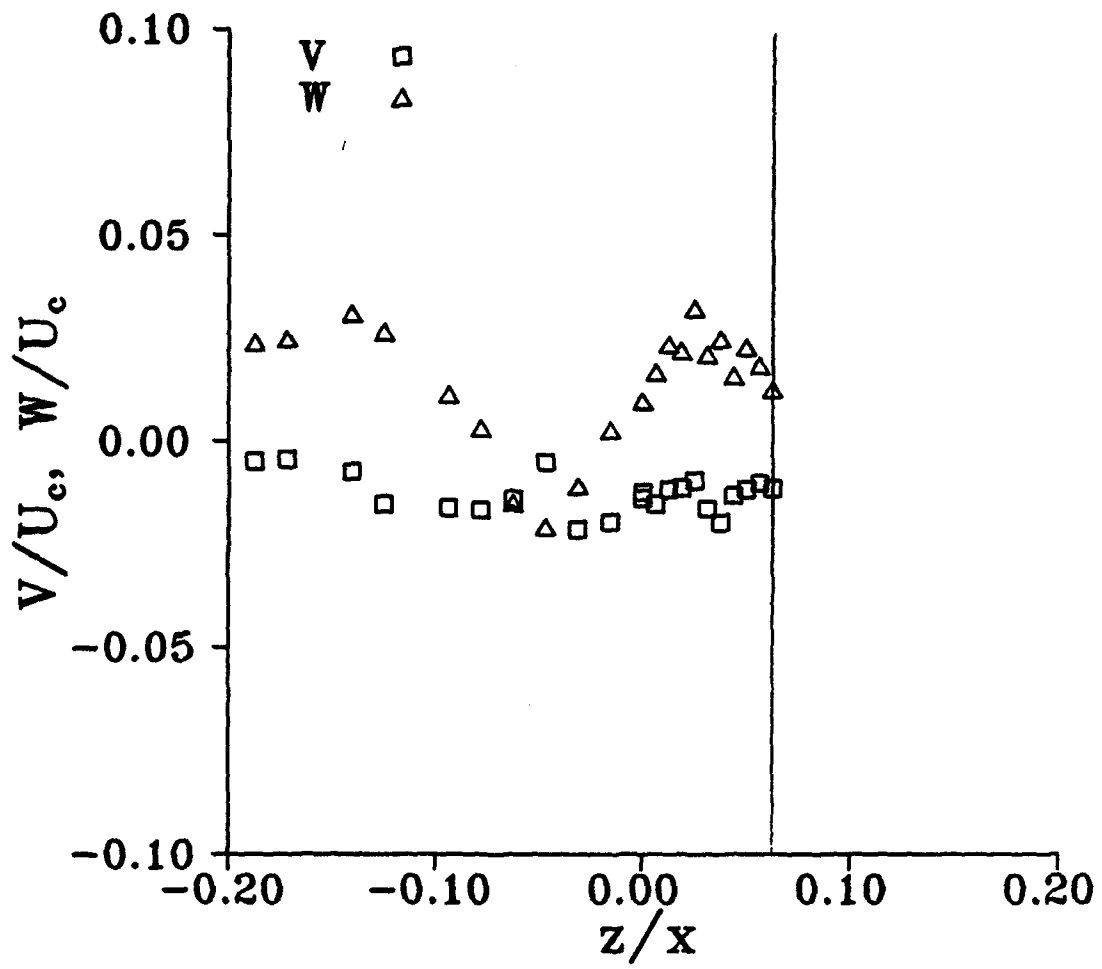


Figure 4.7b. Vertical profiles of the horizontal and vertical mean velocities at $x/d=32$ for the shallow jet, $h/d=2$, $y/d=0$.

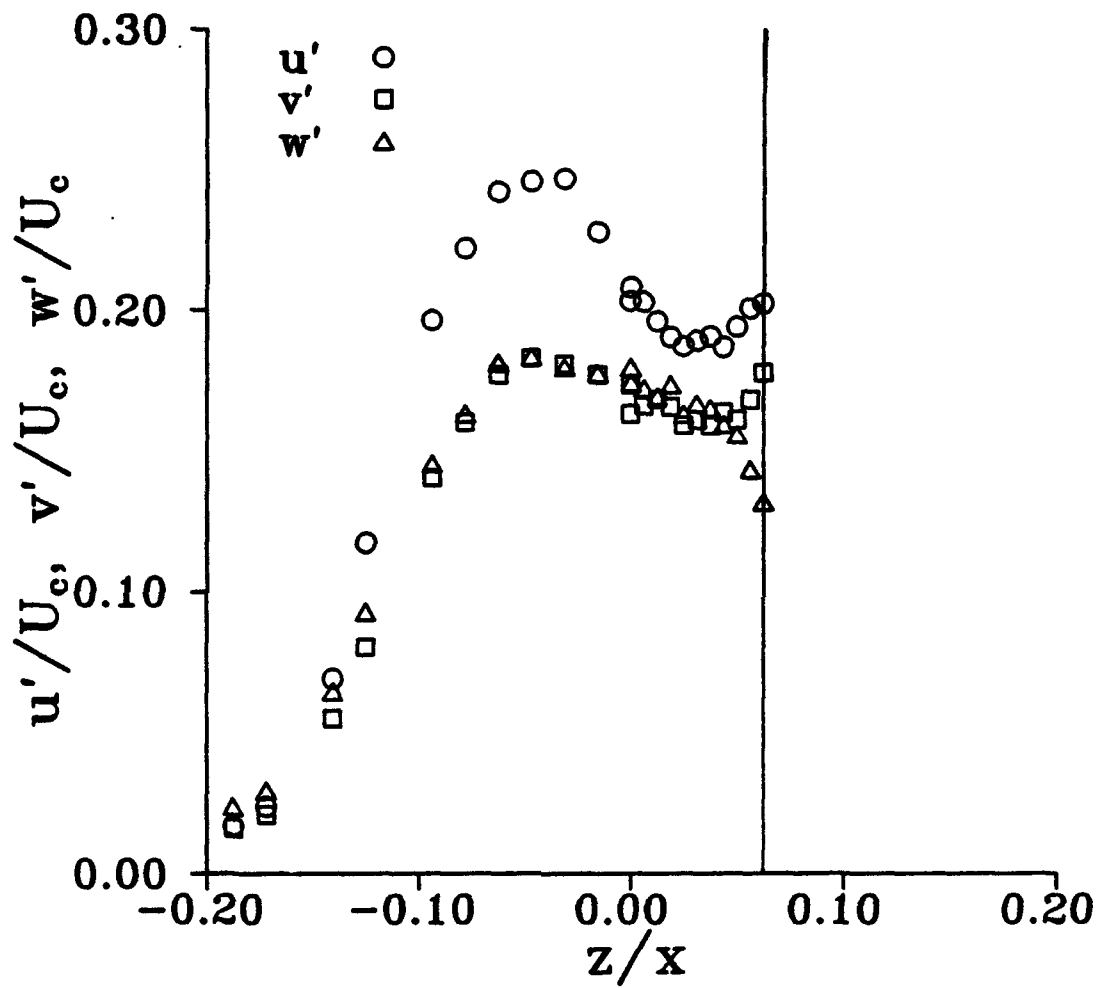


Figure 4.7c. Vertical profiles of the RMS velocity fluctuations at $x/d=32$ for the shallow jet, $h/d=2$, $y/d=0$.

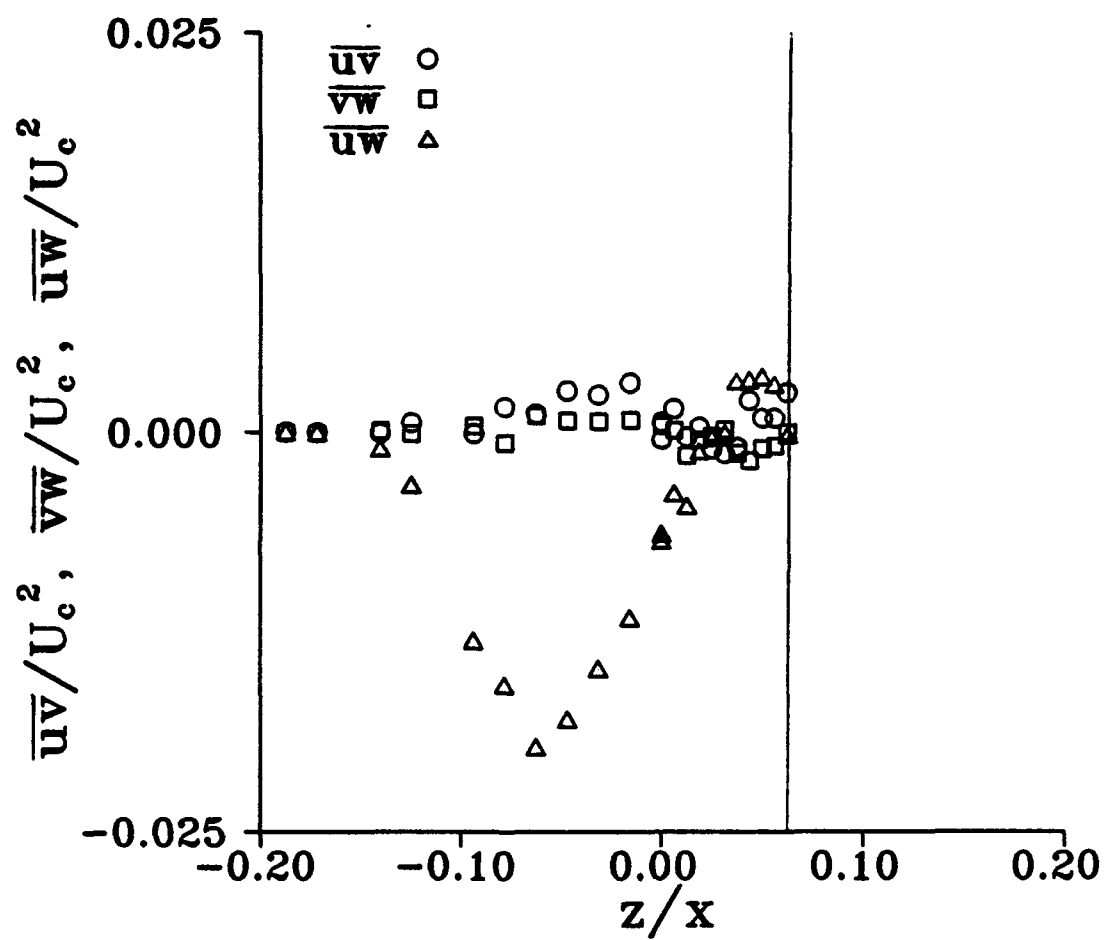


Figure 4.7d. Vertical profiles of the Reynolds stresses at $x/d=32$ for the shallow jet, $h/d=2$, $y/d=0$.

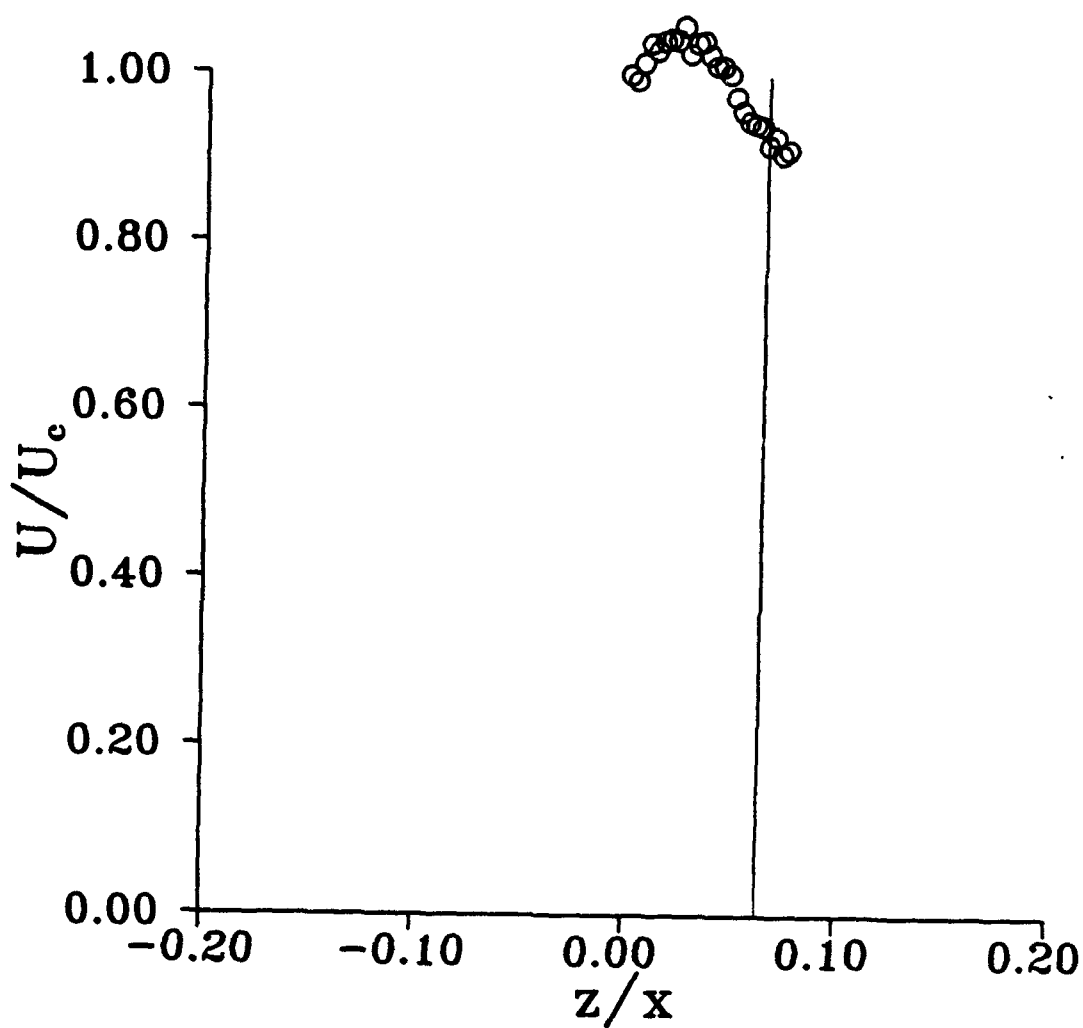


Figure 4.8a. Vertical profile of the streamwise mean velocity above the jet centerline at $x/d=32$ for the shallow jet, $h/d=2$, $y/d=0$.

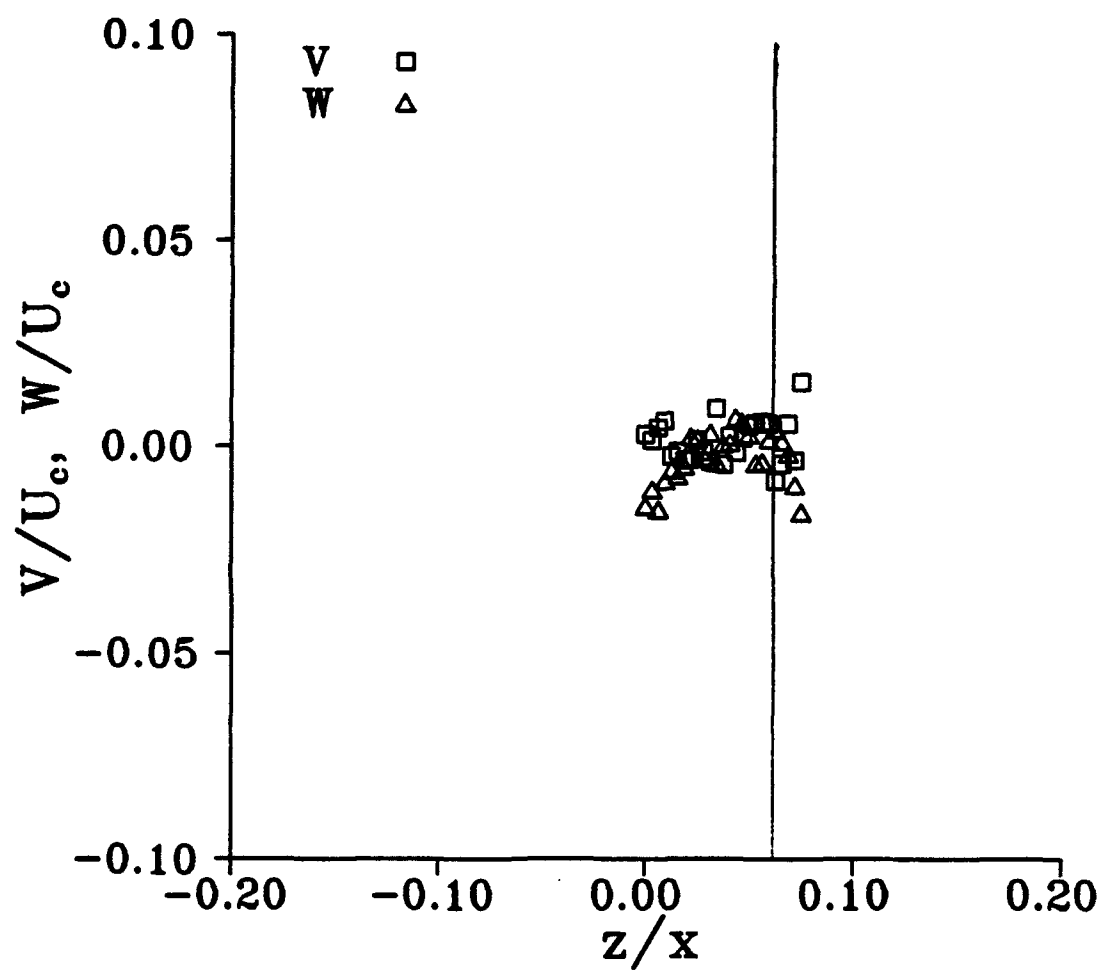


Figure 4.8b. Vertical profiles of the horizontal and vertical mean velocities above the jet centerline at $x/d=32$ for the shallow jet, $h/d=2$, $y/d=0$.

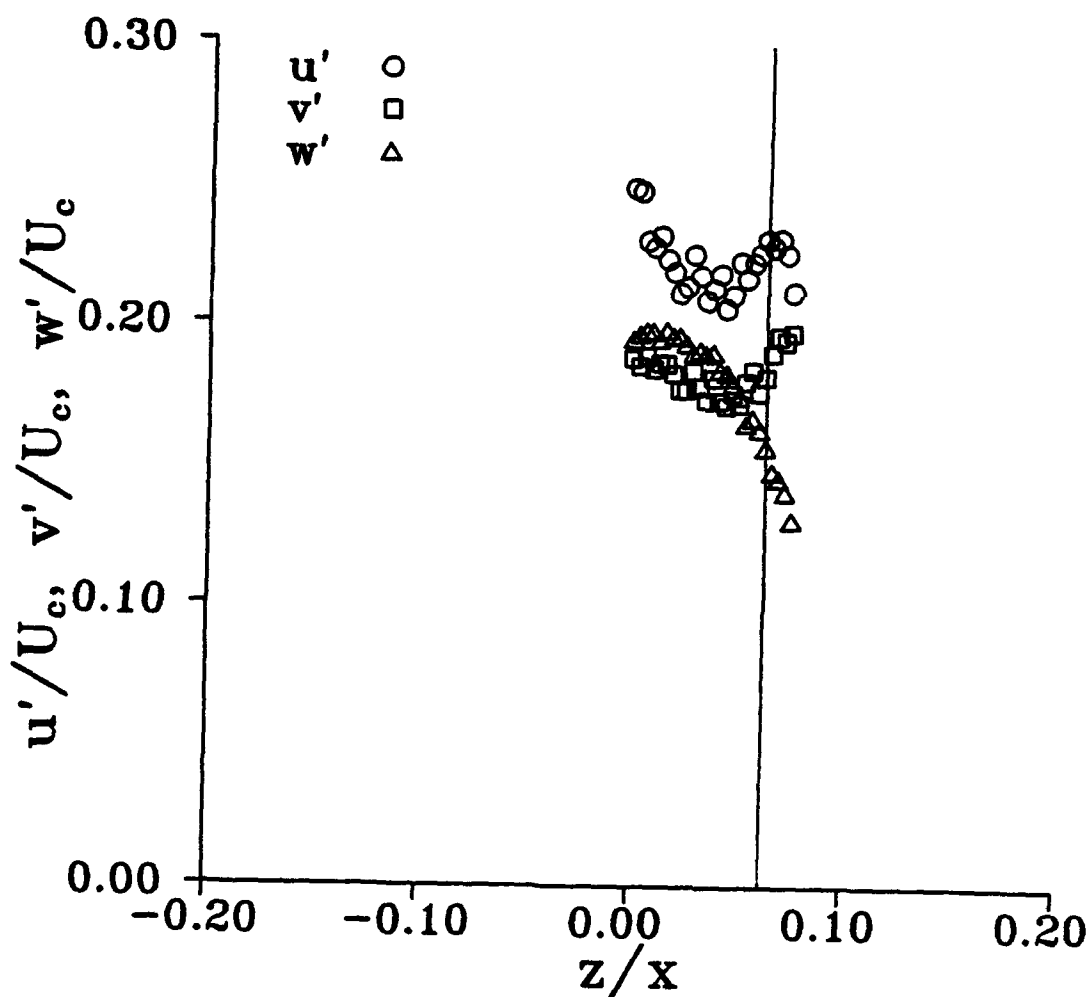


Figure 4.8c. Vertical profiles of the RMS velocity fluctuations above the jet centerline at $x/d=32$ for the shallow jet, $h/d=2$, $y/d=0$.

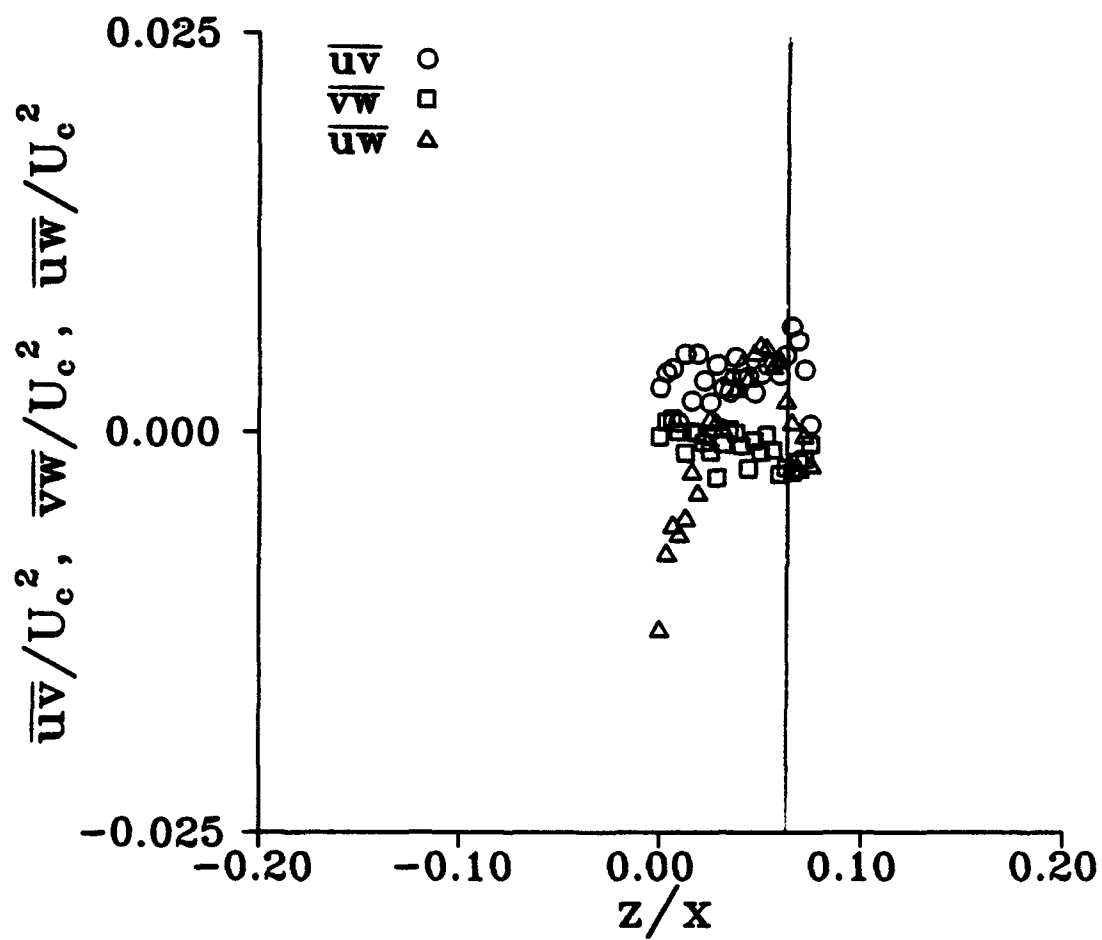


Figure 4.8d. Vertical profiles of the Reynolds stresses above the jet centerline at $x/d=32$ for the shallow jet, $h/d=2$, $y/d=0$.

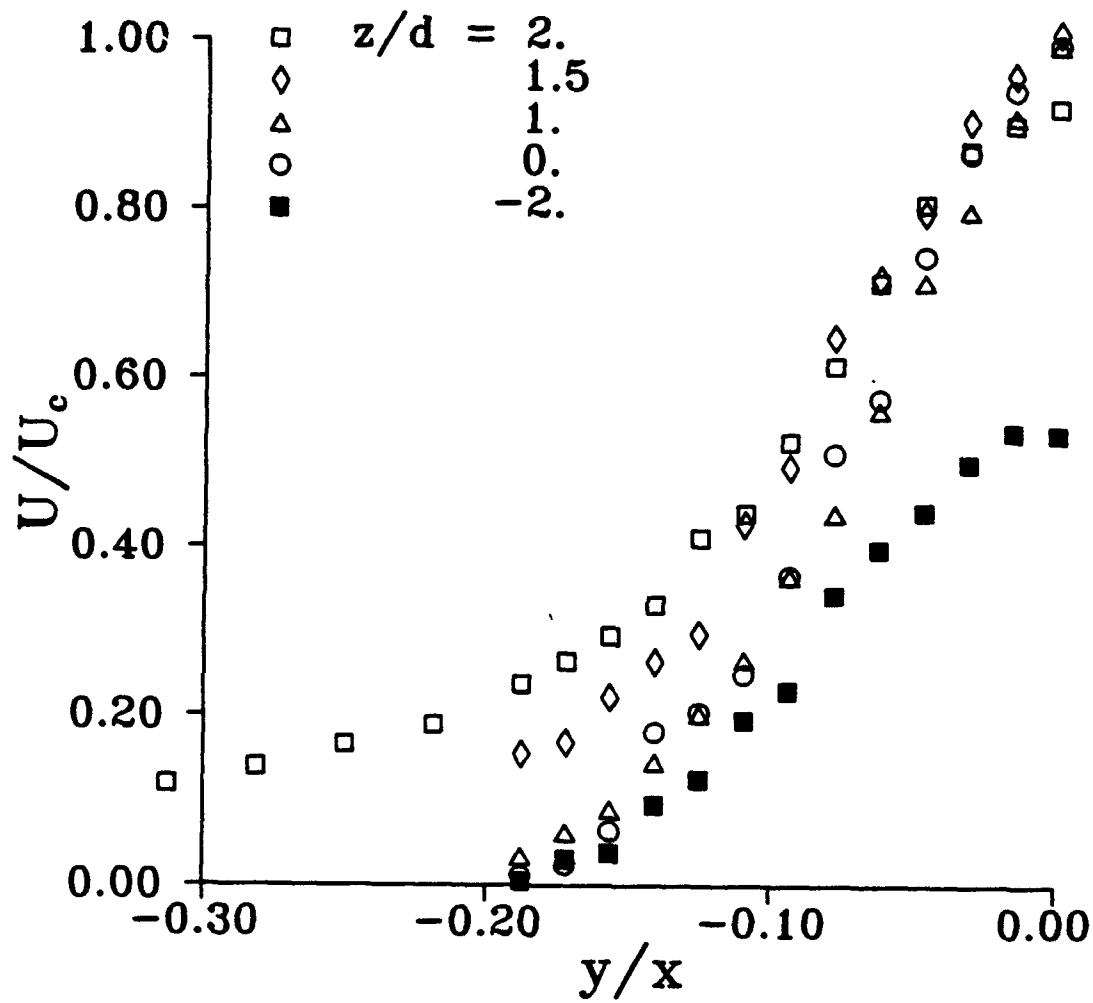


Figure 4.9a. Horizontal profiles of the streamwise mean velocity U/U_c at $x/d=32$ for the shallow jet, $h/d=2$.

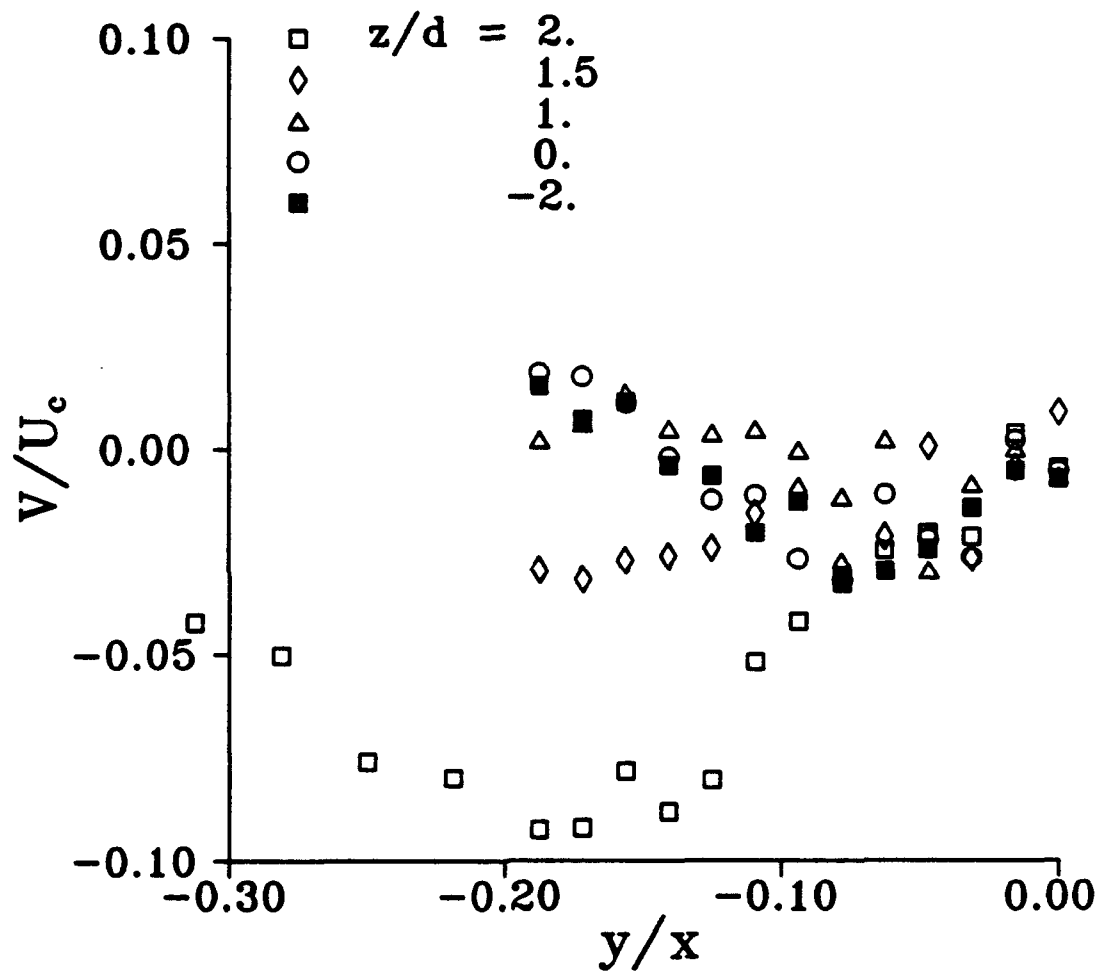


Figure 4.9b. Horizontal profiles of the horizontal mean velocity V/U_c at $x/d=32$ for the shallow jet, $h/d=2$.

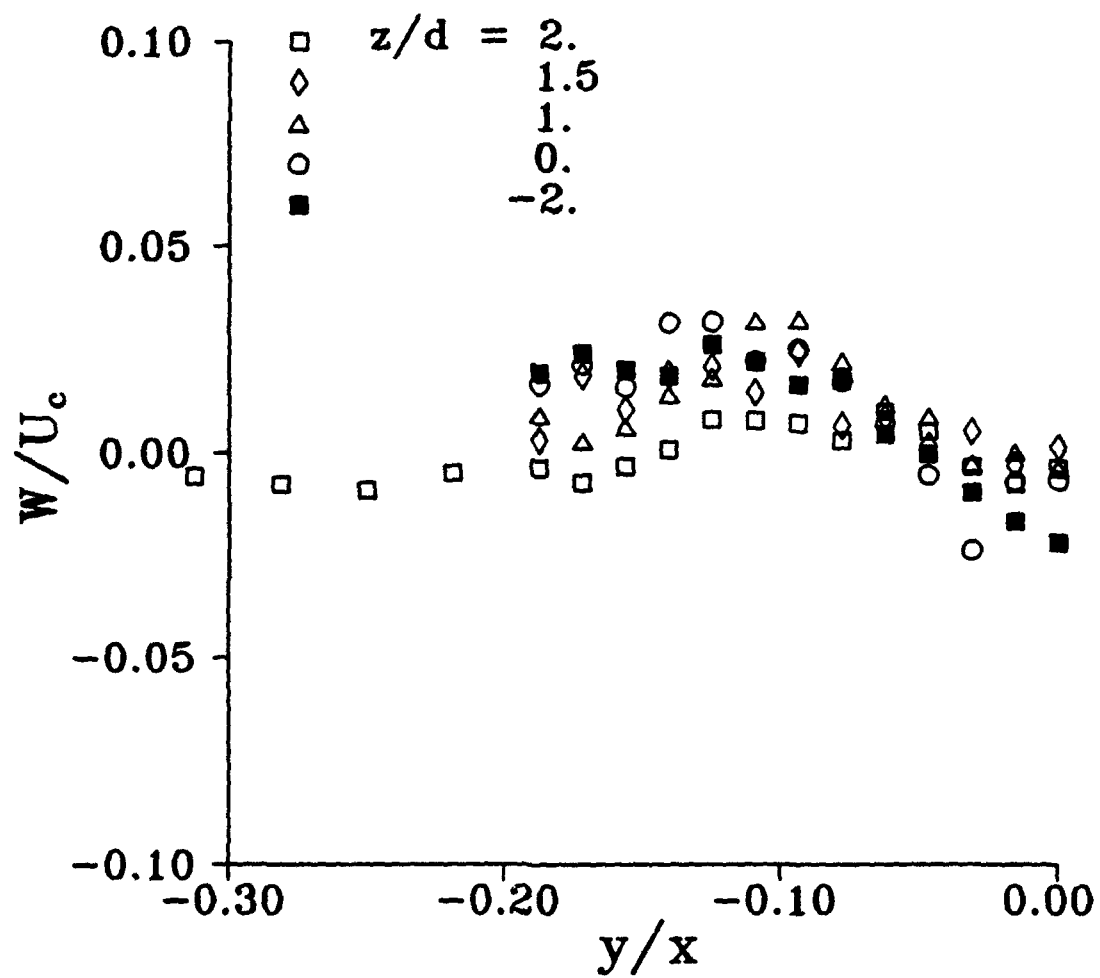


Figure 4.9c. Horizontal profiles of the vertical mean velocity W/U_c at $x/d=32$ for the shallow jet, $h/d=2$.

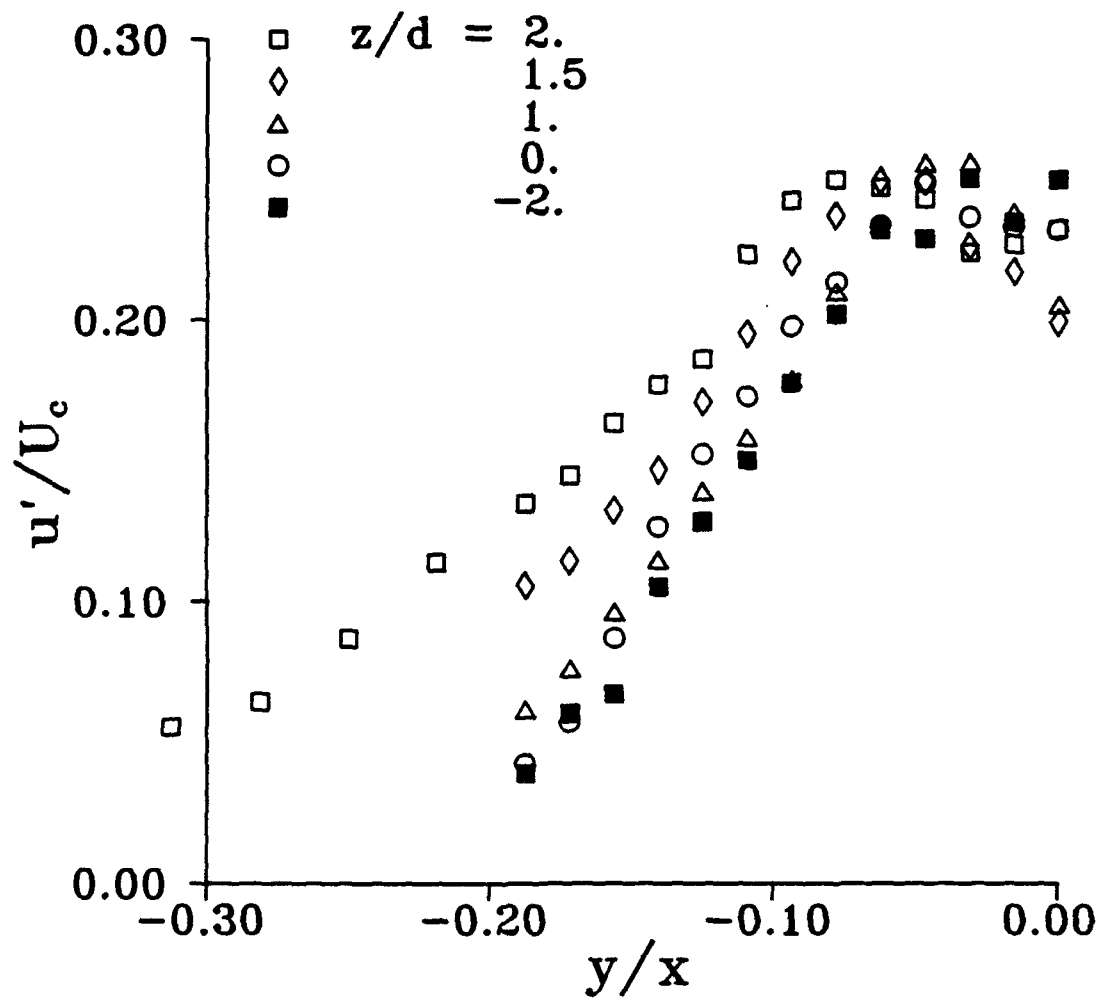


Figure 4.9d. Horizontal profiles of the streamwise RMS velocity fluctuations, u'/U_c at $x/d=32$ for the shallow jet, $h/d=2$.

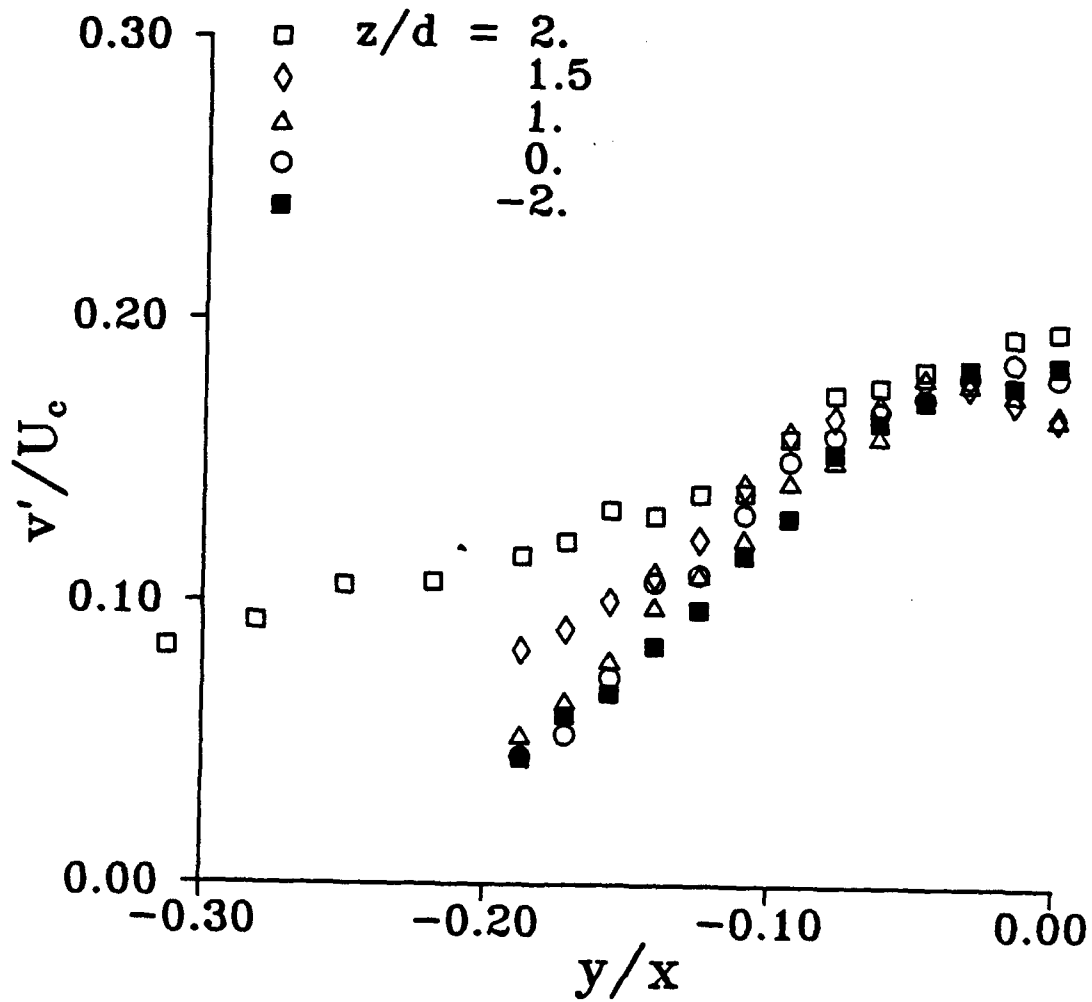


Figure 4.9e. Horizontal profiles of the horizontal RMS velocity fluctuations v'/U_c at $x/d=32$ for the shallow jet, $h/d=2$.

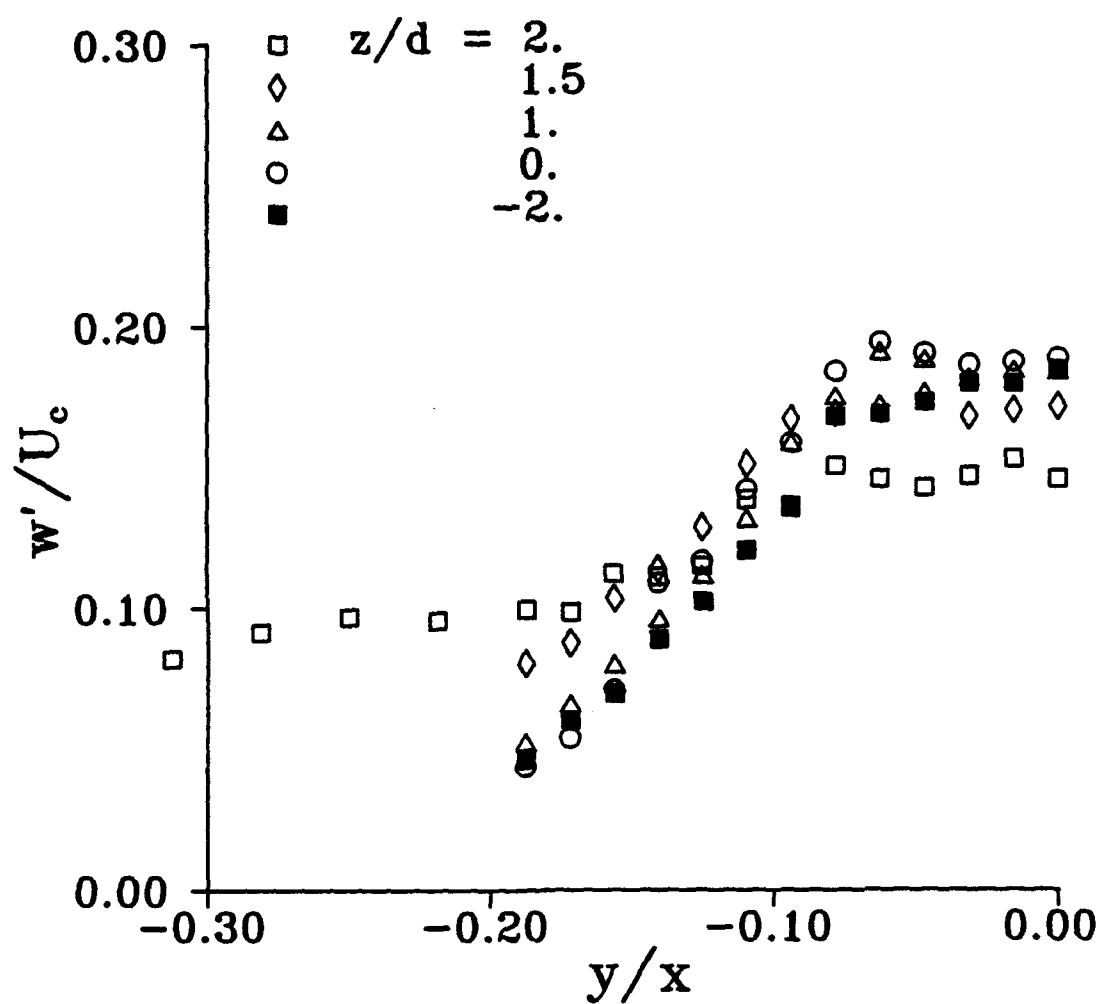


Figure 4.9f. Horizontal profiles of the vertical RMS velocity fluctuations w'/U_c at $x/d=32$ for the shallow jet, $h/d=2$.

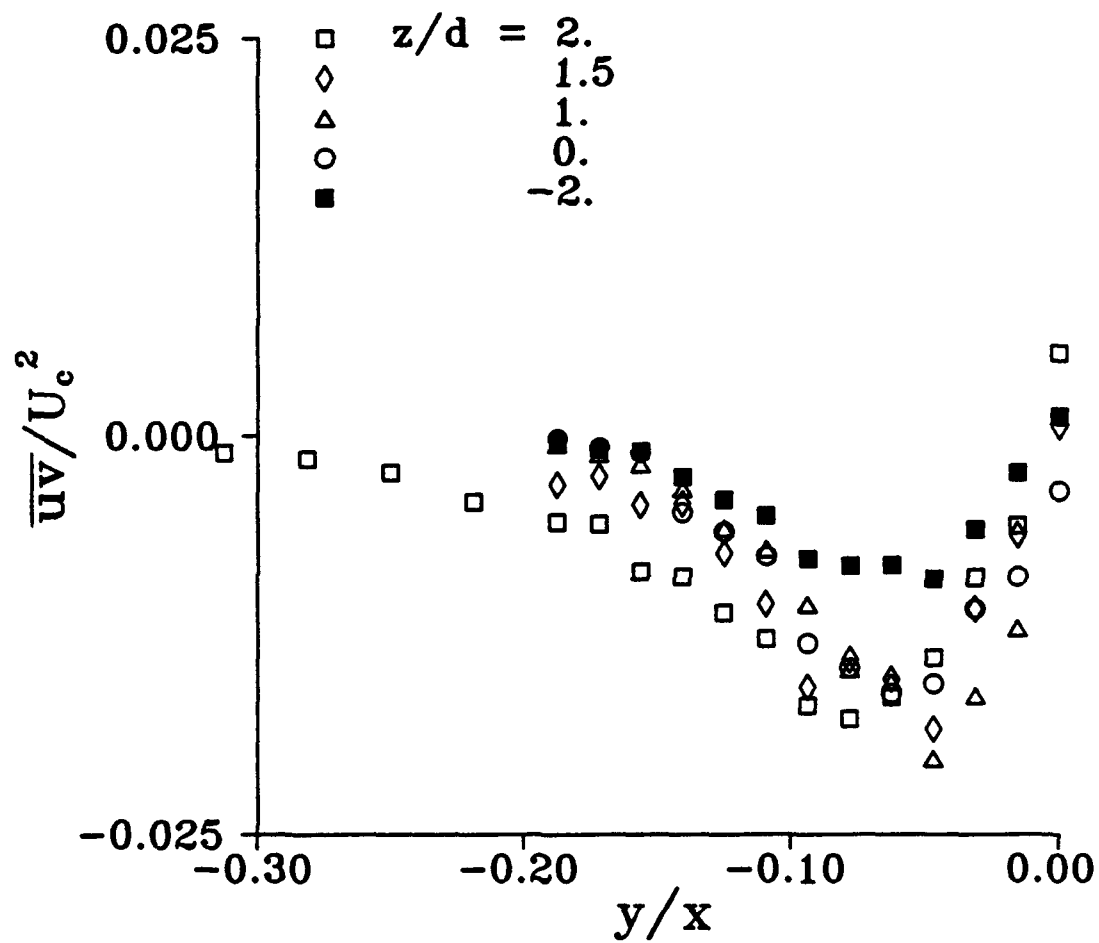


Figure 4.9g. Horizontal profiles of the Reynolds stress \overline{uv}/U_c^2 at $x/d=32$ for the shallow jet, $h/d=2$.

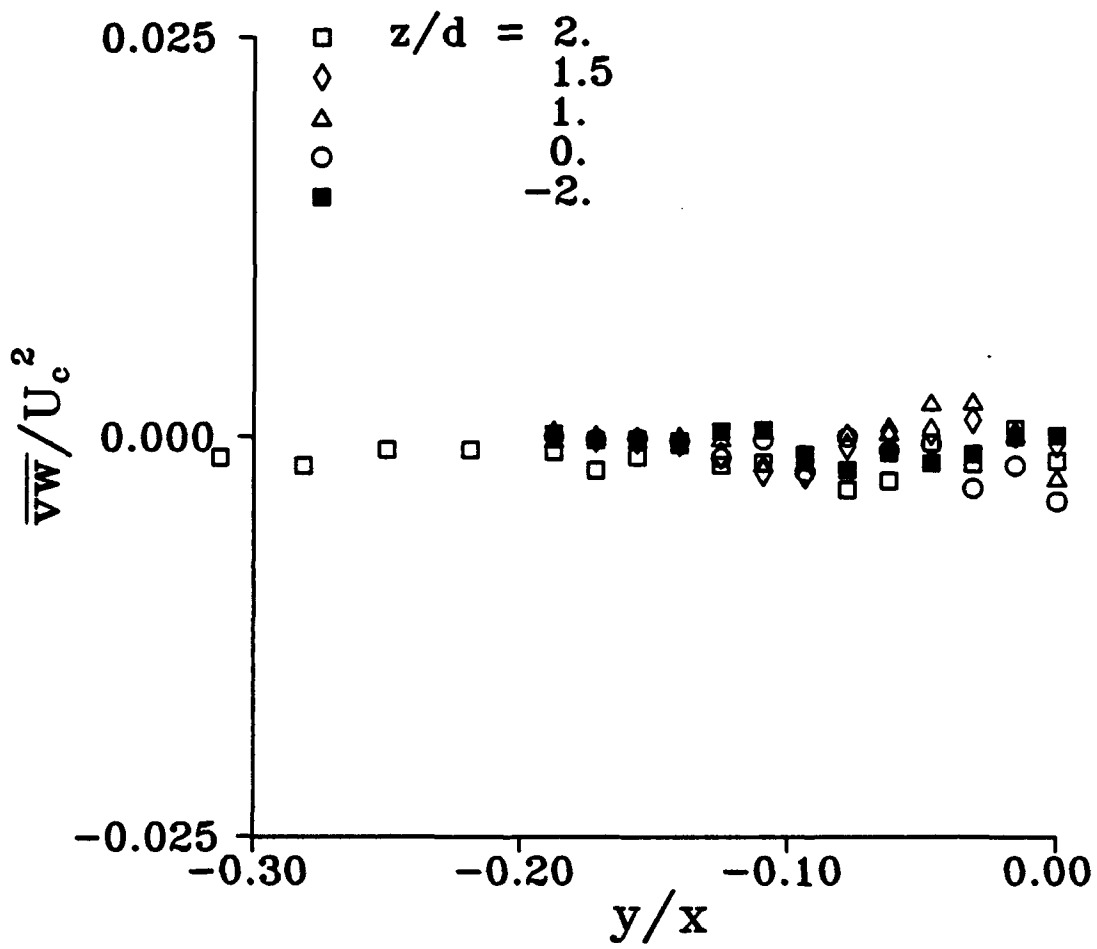


Figure 4.9h. Horizontal profiles of the Reynolds stress \overline{vw}/U_c^2 at $x/d=32$ for the shallow jet, $h/d=2$.

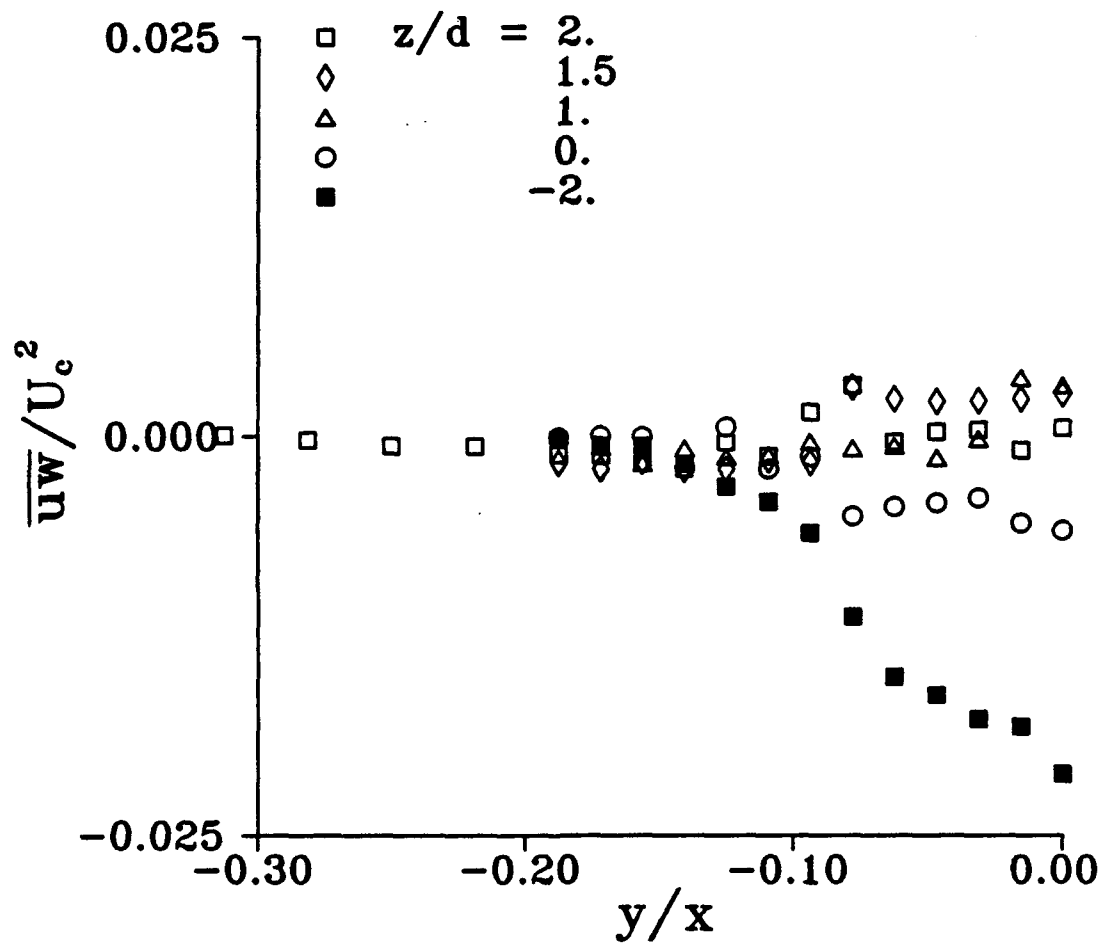


Figure 4.9i. Horizontal profiles of the Reynolds stress \overline{uw}/U_c^2 at $x/d=32$ for the shallow jet, $h/d=2$.

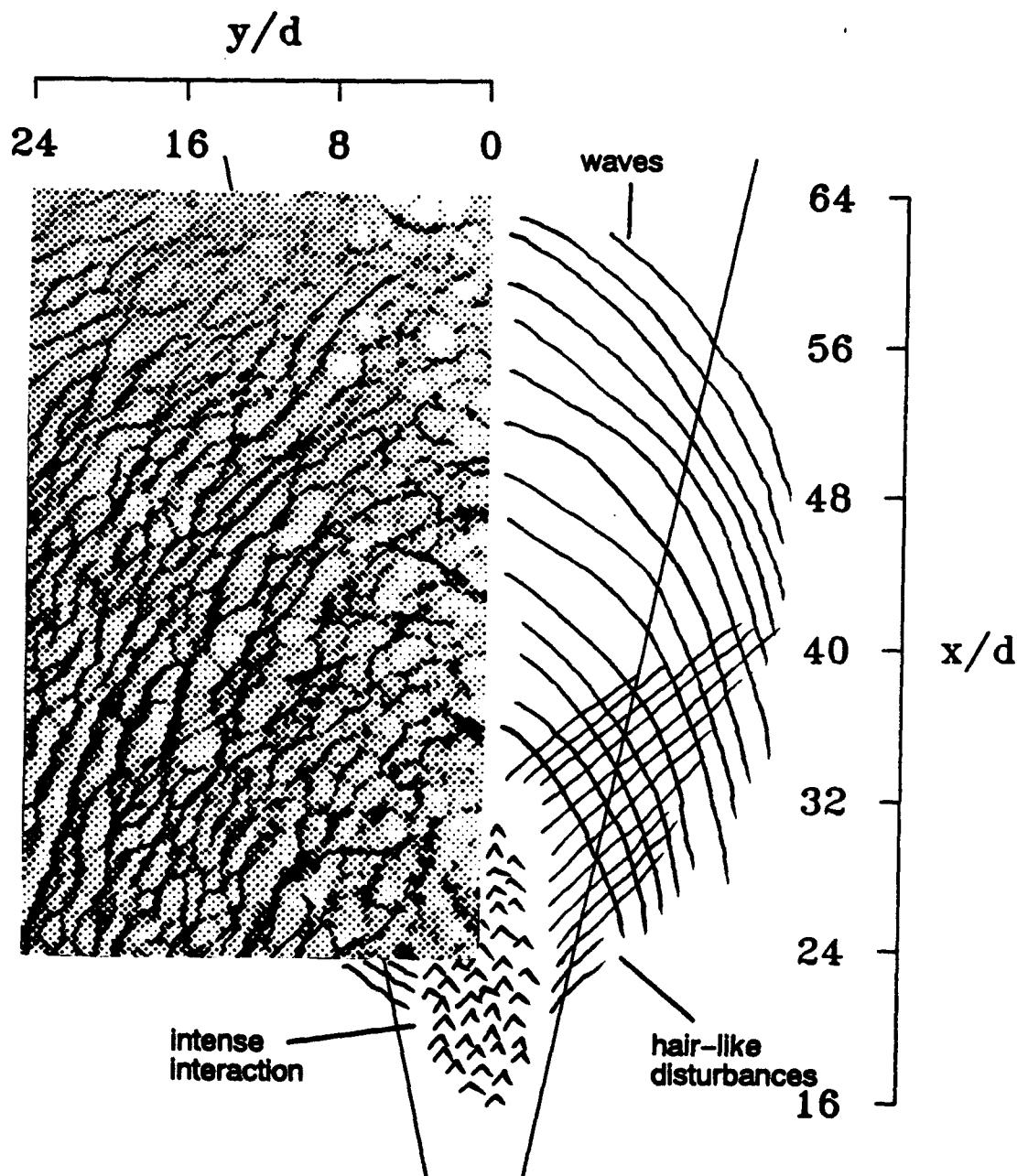


Figure 4.10. Shadowgraph and sketch showing surface deformations above the shallow jet, $h/d=2$, beneath a clean free surface. The inset on the left is a shadowgraph, inverted so as to show the crests of waves as dark rather than light. The sketch indicates a region of intense jet/free-surface interaction with higher amplitude but rather incoherent waves being generated near the jet centerline. These waves are observed to coalesce into more coherent, smaller amplitude waves propagating away from the jet centerline. The wavelength and wave speed of these waves are observed from video images to be approximately 1 to 4 cm and 25 cm/s, respectively. Also indicated are the closely spaced hair-like disturbances which are observed in the video images but were not resolved in the inset shadowgraph.

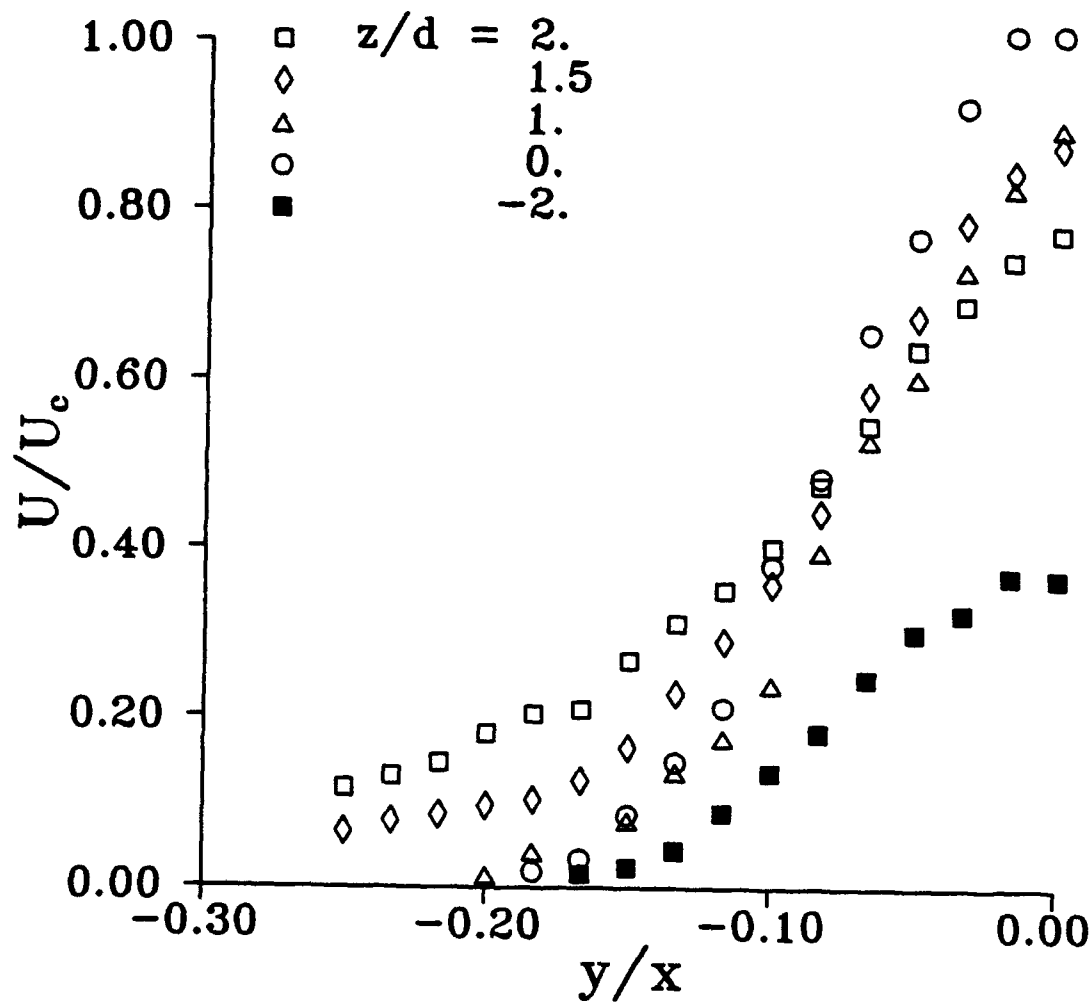


Figure 4.11a. Horizontal profiles of the streamwise mean velocity U/U_c at $x/d=24$ for the shallow jet, $h/d=2$.

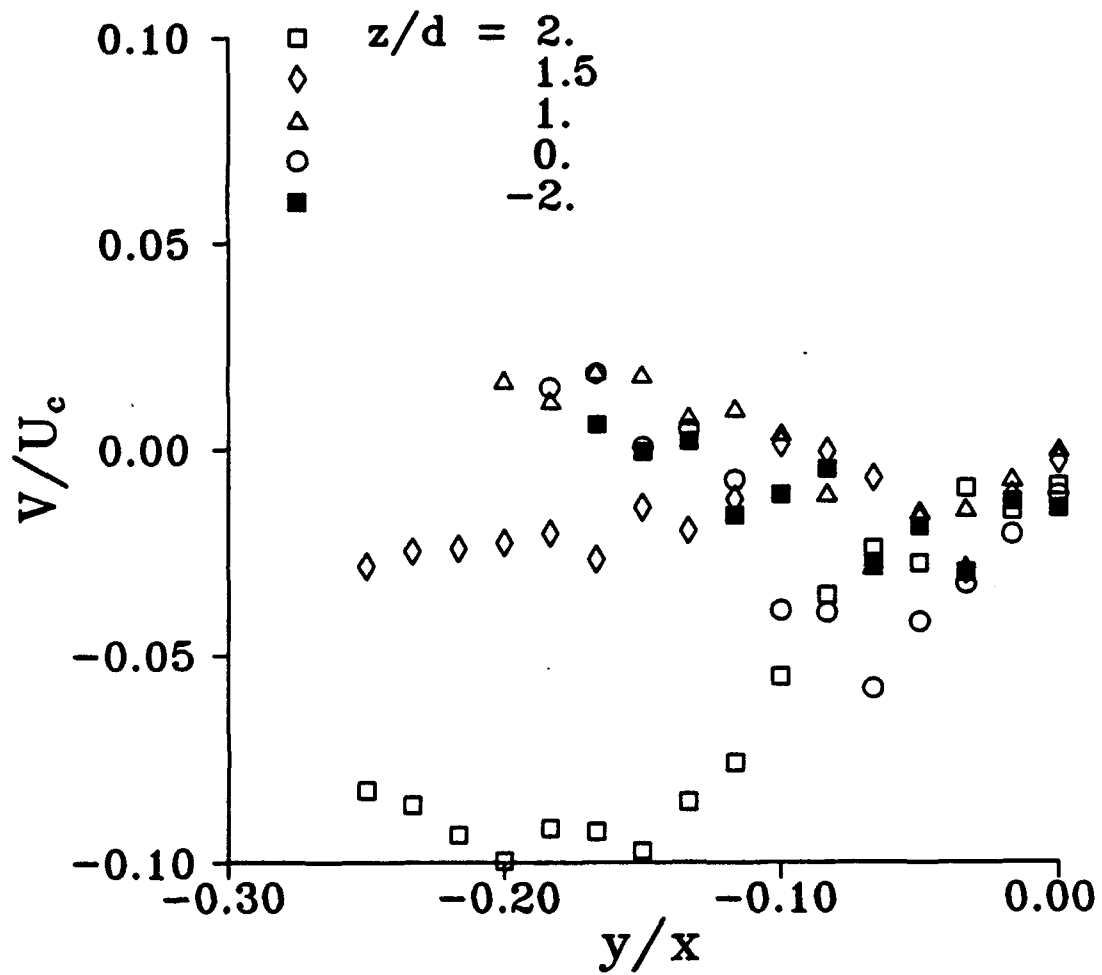


Figure 4.11b. Horizontal profiles of the horizontal mean velocity V/U_c at $x/d=24$ for the shallow jet, $h/d=2$.

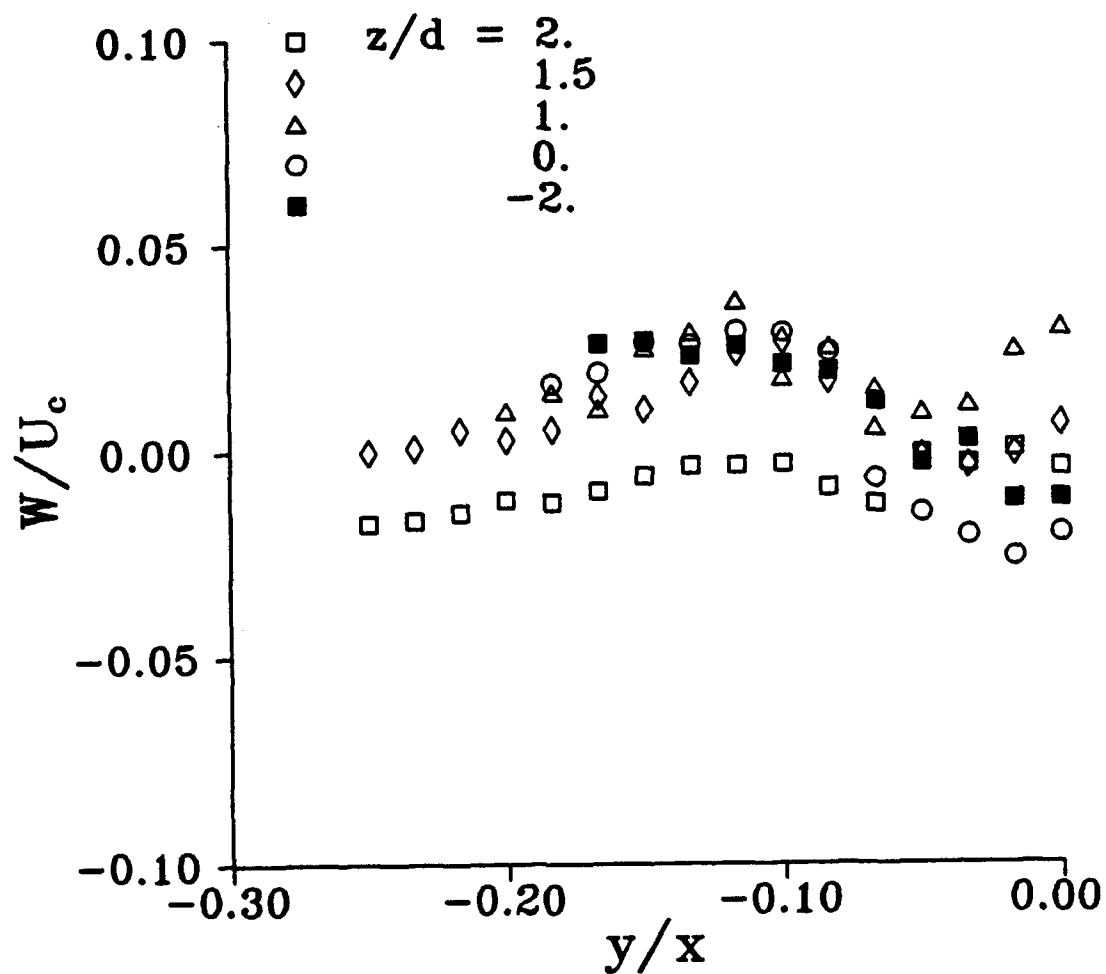


Figure 4.11c. Horizontal profiles of the vertical mean velocity W/U_c at $x/d=24$ for the shallow jet, $h/d=2$.

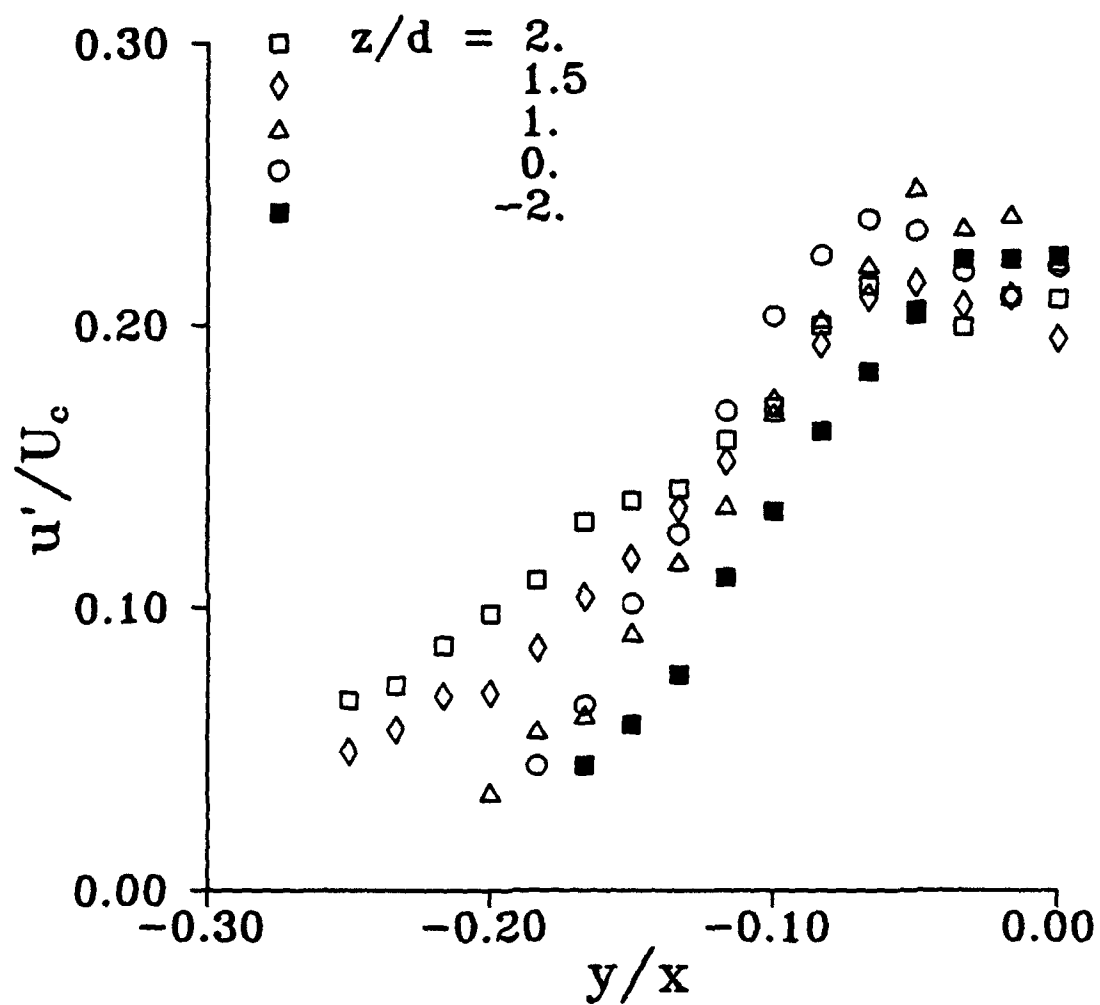


Figure 4.11d. Horizontal profiles of the streamwise RMS velocity fluctuations u'/U_c at $x/d=24$ for the shallow jet, $h/d=2$.

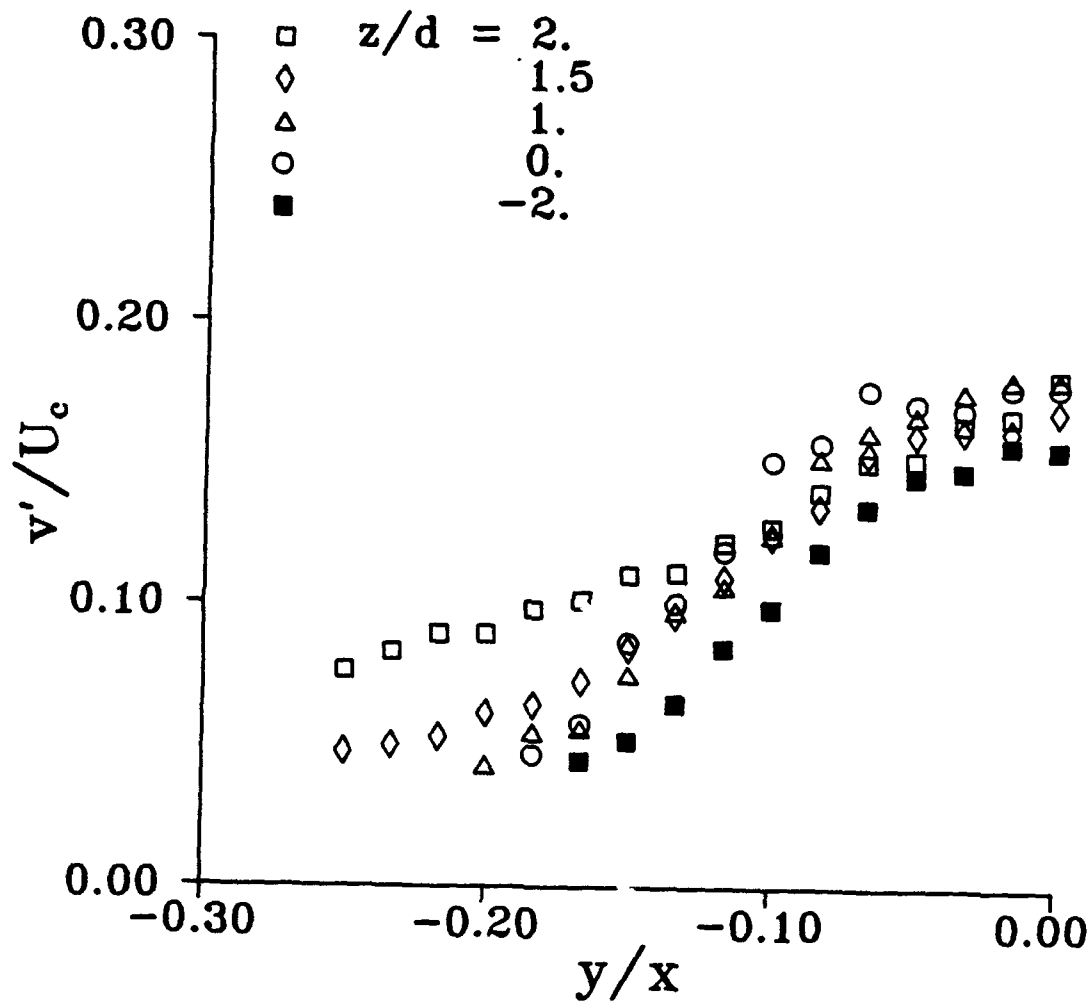


Figure 4.11e. Horizontal profiles of the horizontal RMS velocity fluctuations v'/U_c at $x/d=24$ for the shallow jet, $h/d=2$.

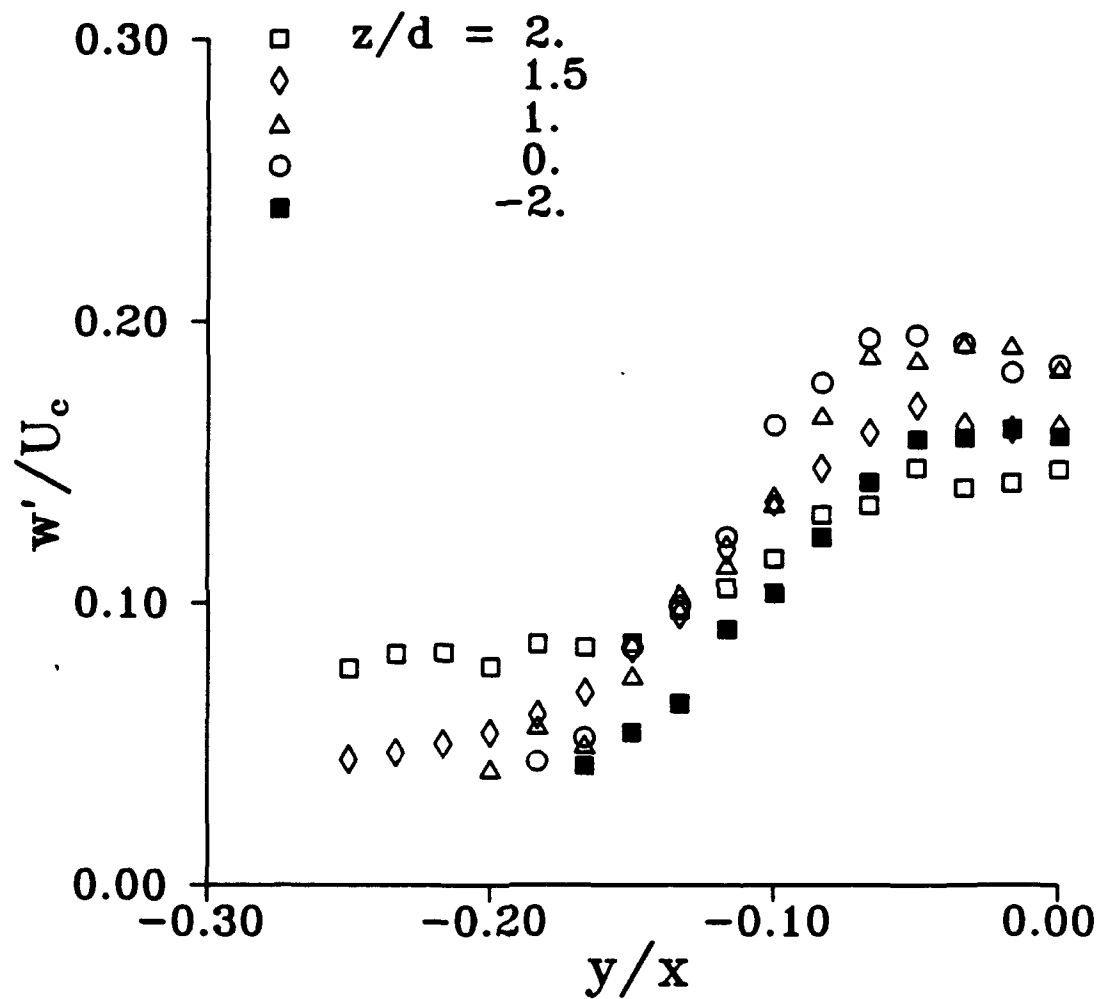


Figure 4.11f. Horizontal profiles of the vertical RMS velocity fluctuations w'/U_c at $x/d=24$ for the shallow jet, $h/d=2$.

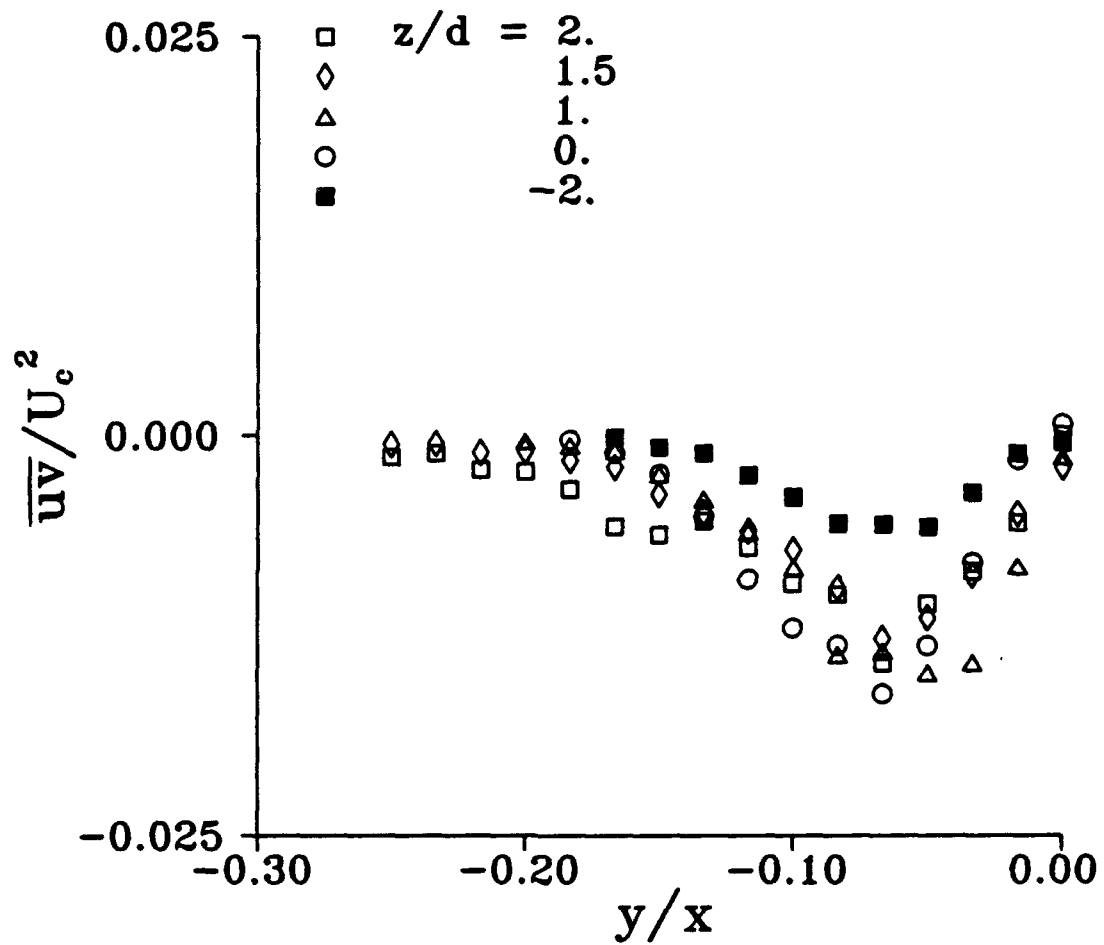


Figure 4.11g. Horizontal profiles of the Reynolds stress \overline{uv}/U_c^2 at $x/d=24$ for the shallow jet, $h/d=2$.

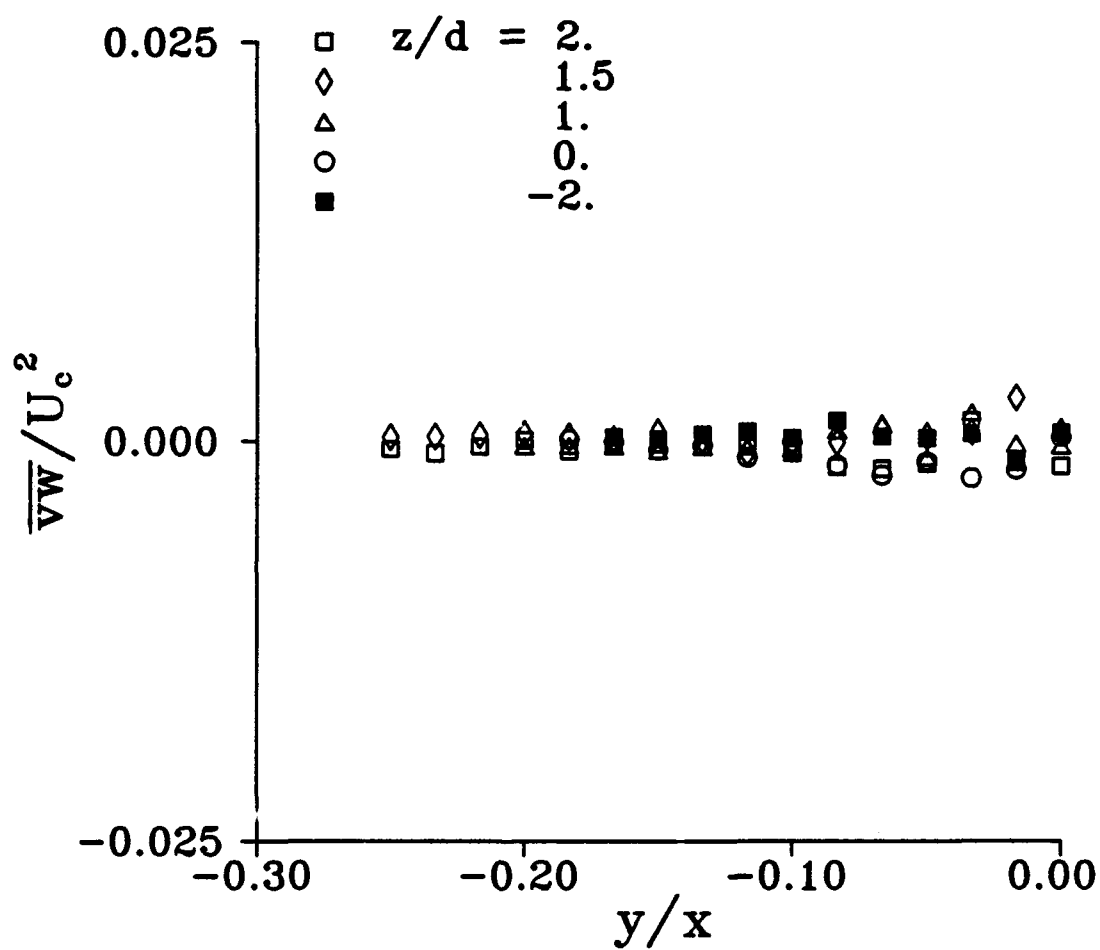


Figure 4.11h. Horizontal profiles of the Reynolds stress \overline{vw}/U_c^2 at $x/d=24$ for the shallow jet, $h/d=2$.

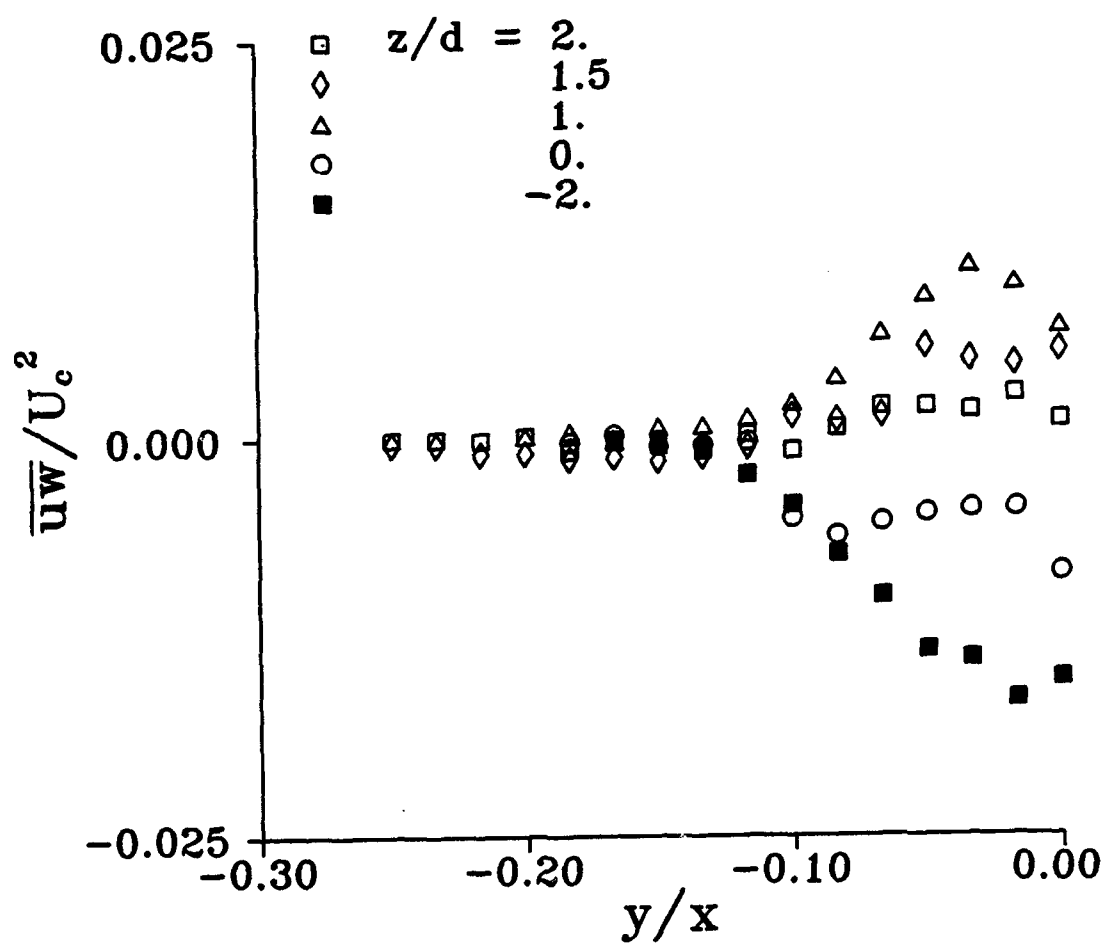


Figure 4.11i. Horizontal profiles of the Reynolds stress \overline{uw}/U_c^2 at $x/d=24$ for the shallow jet, $h/d=2$.

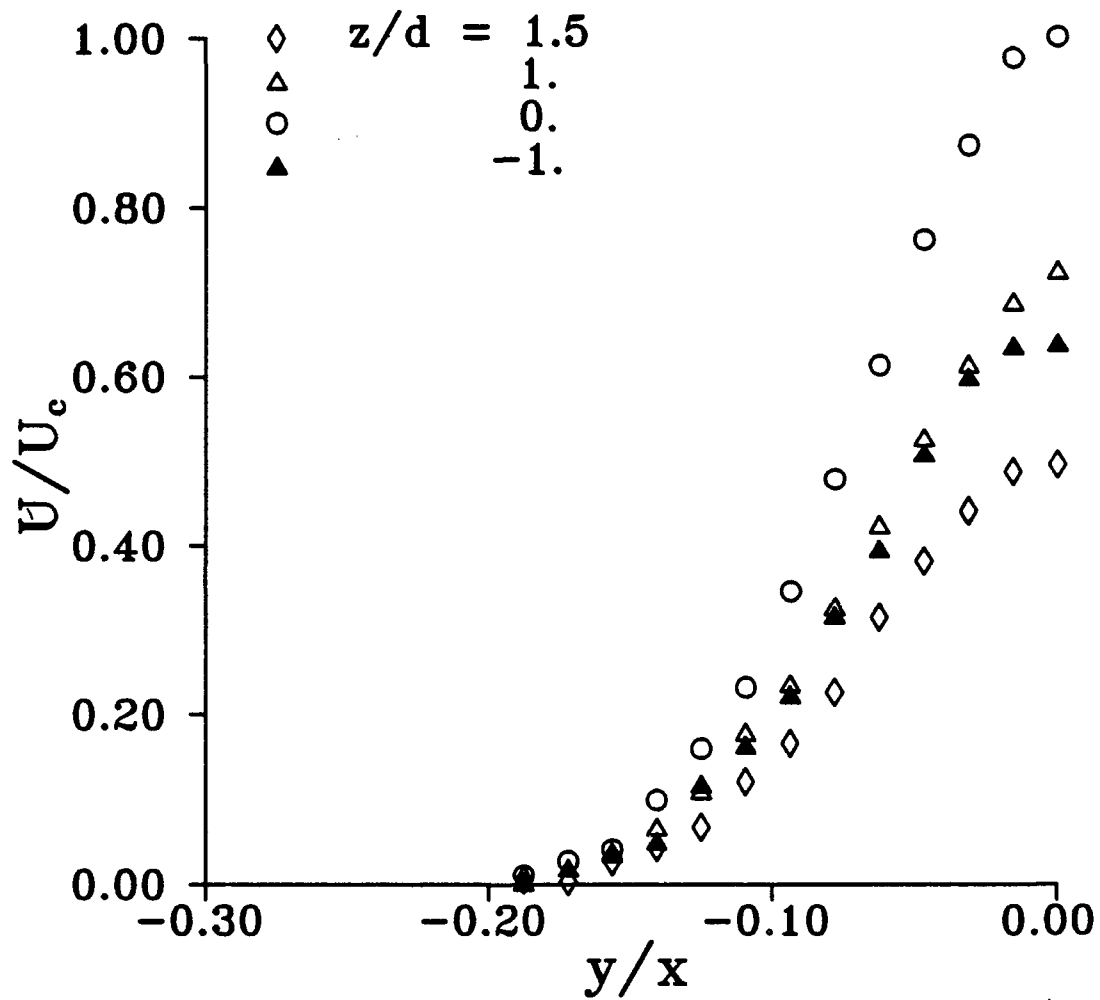


Figure 4.12a. Horizontal profiles of the streamwise mean velocity U/U_c at $x/d=16$ for the shallow jet, $h/d=2$.

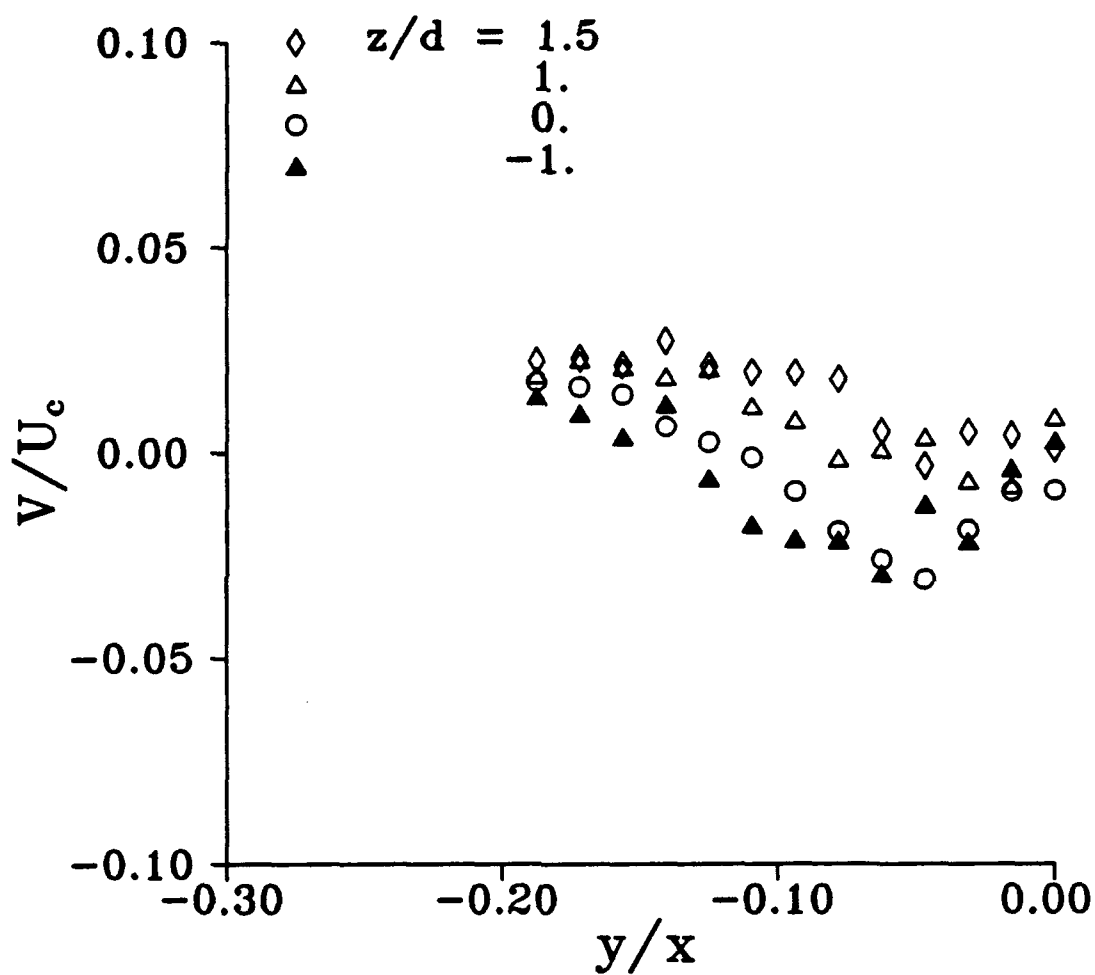


Figure 4.12b. Horizontal profiles of the horizontal mean velocity V/U_c at $x/d=16$ for the shallow jet, $h/d=2$.

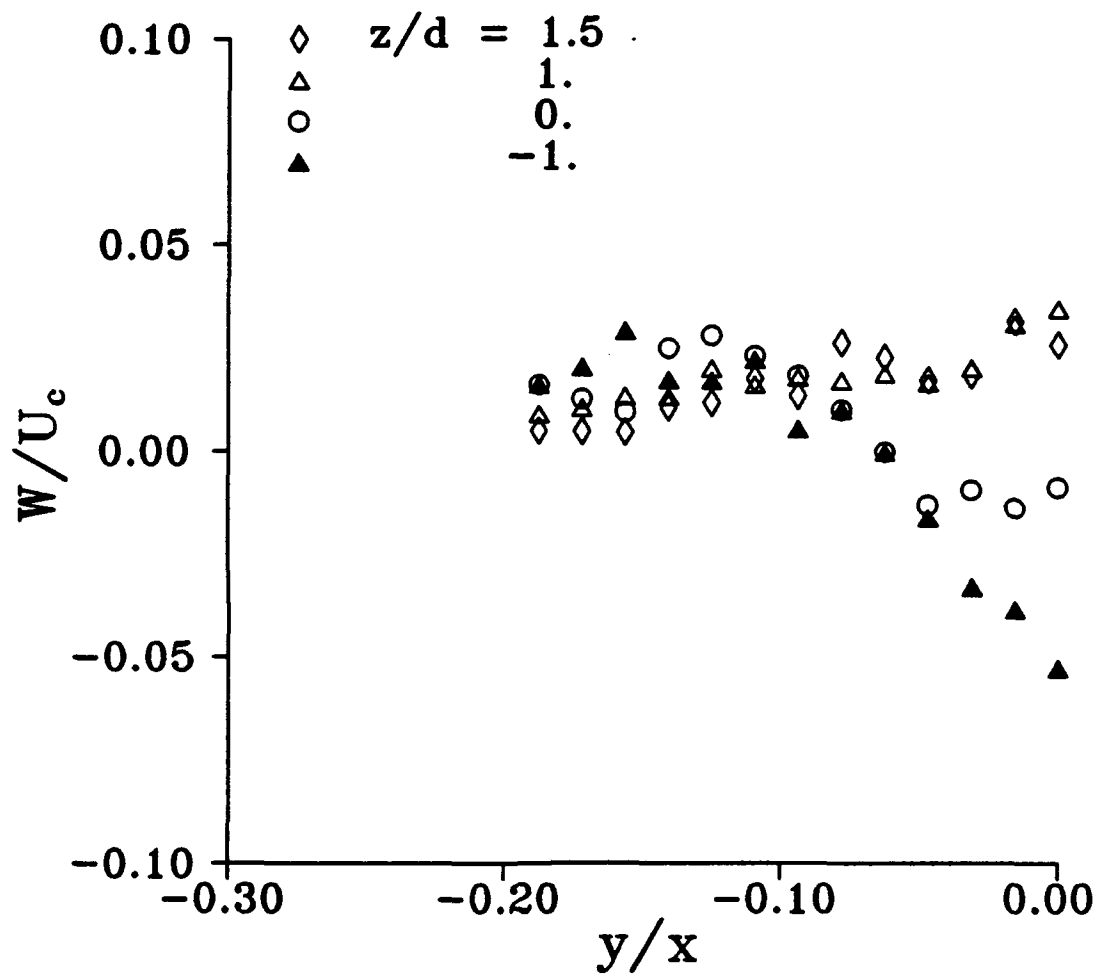


Figure 4.12c. Horizontal profiles of the vertical mean velocity W/U_c at $x/d=16$ for the shallow jet, $h/d=2$.

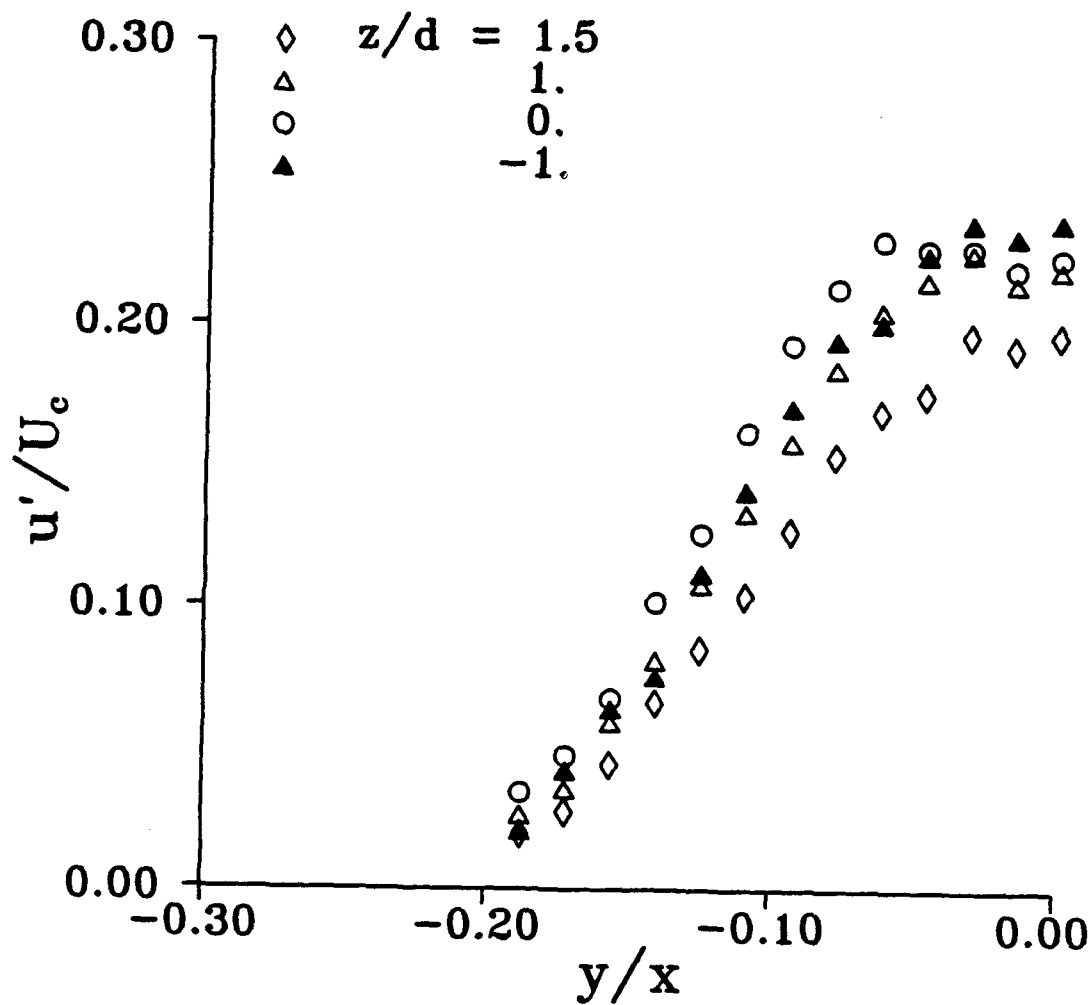


Figure 4.12d. Horizontal profiles of the streamwise RMS velocity fluctuations u'/U_c at $x/d=16$ for the shallow jet, $h/d=2$.

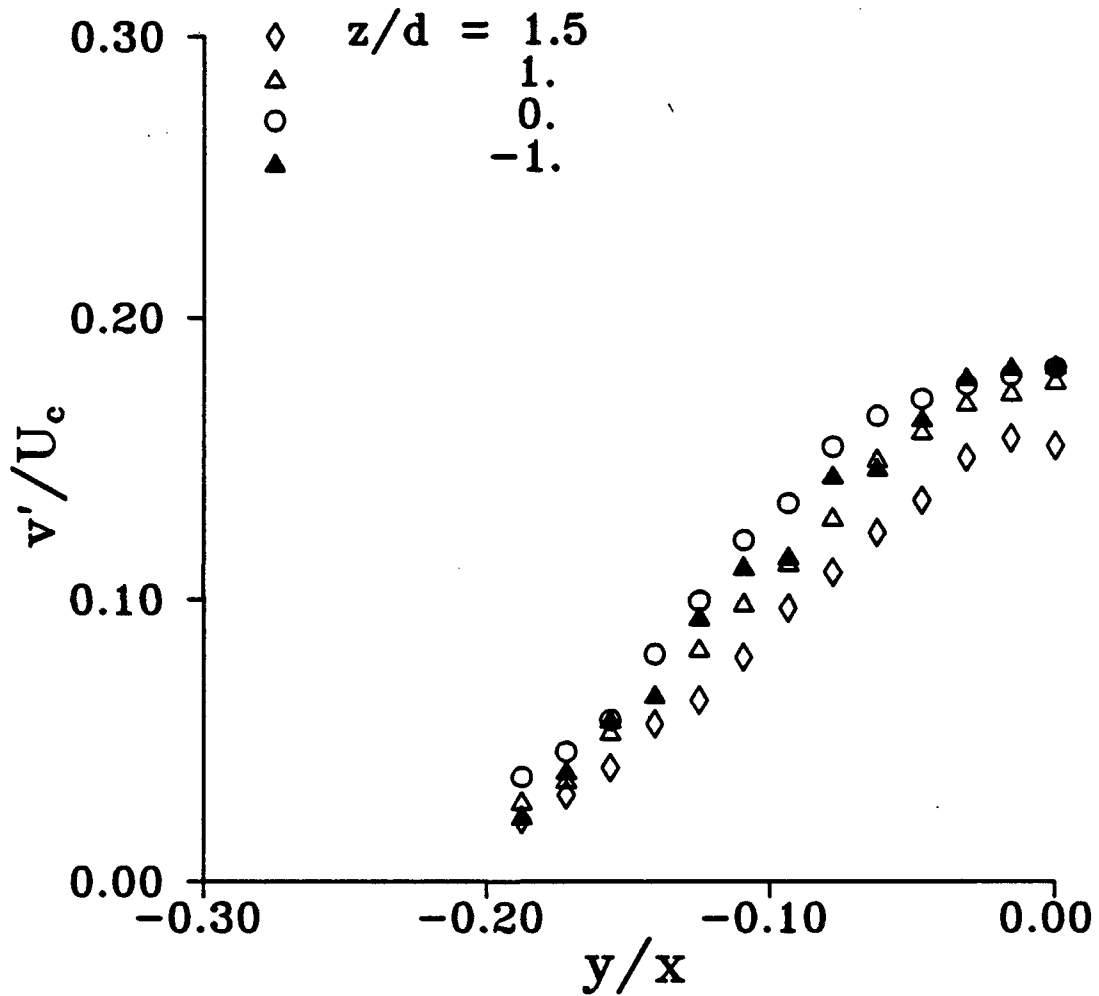


Figure 4.12c. Horizontal profiles of the horizontal RMS velocity fluctuations v'/U_c at $x/d=16$ for the shallow jet, $h/d=2$.

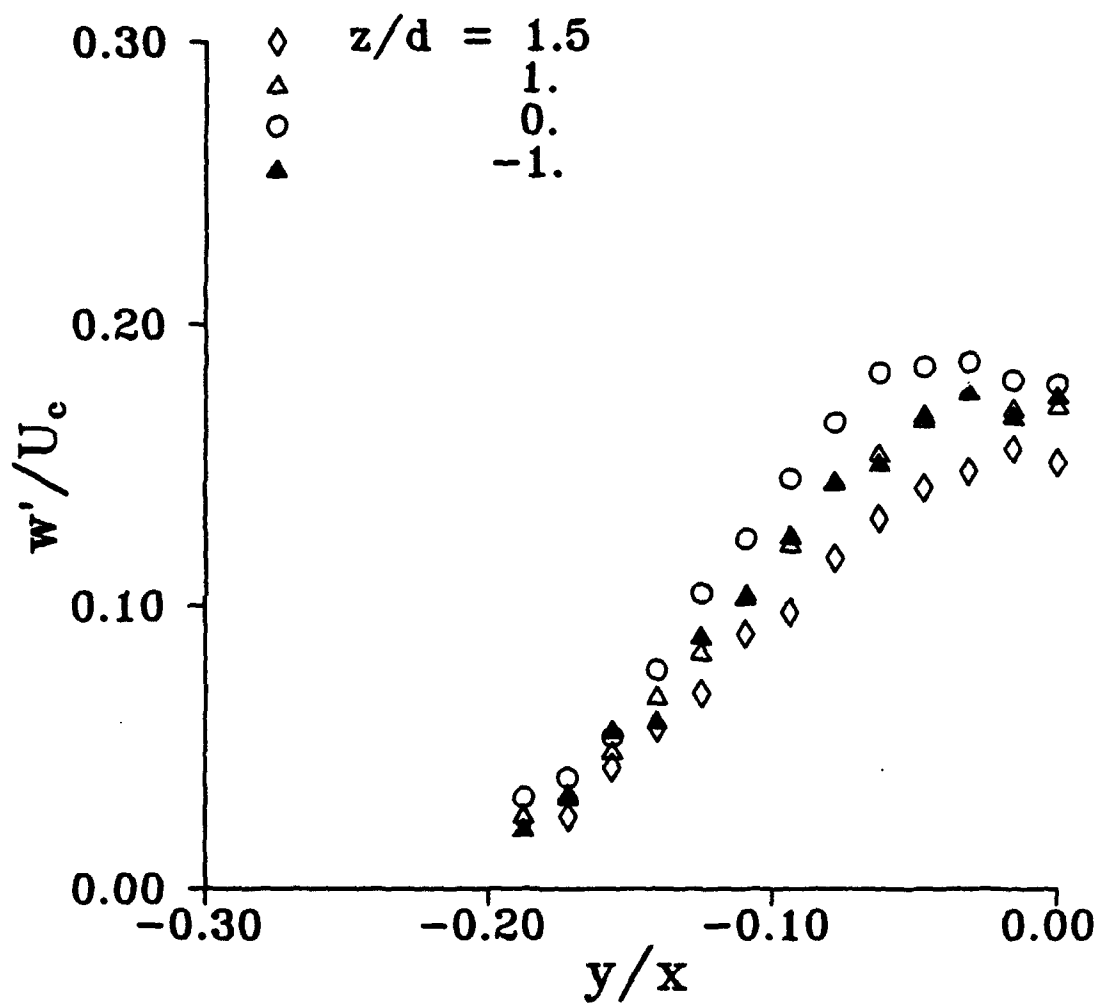


Figure 4.12f. Horizontal profiles of the vertical RMS velocity fluctuations w'/U_c at $x/d=16$ for the shallow jet, $h/d=2$.

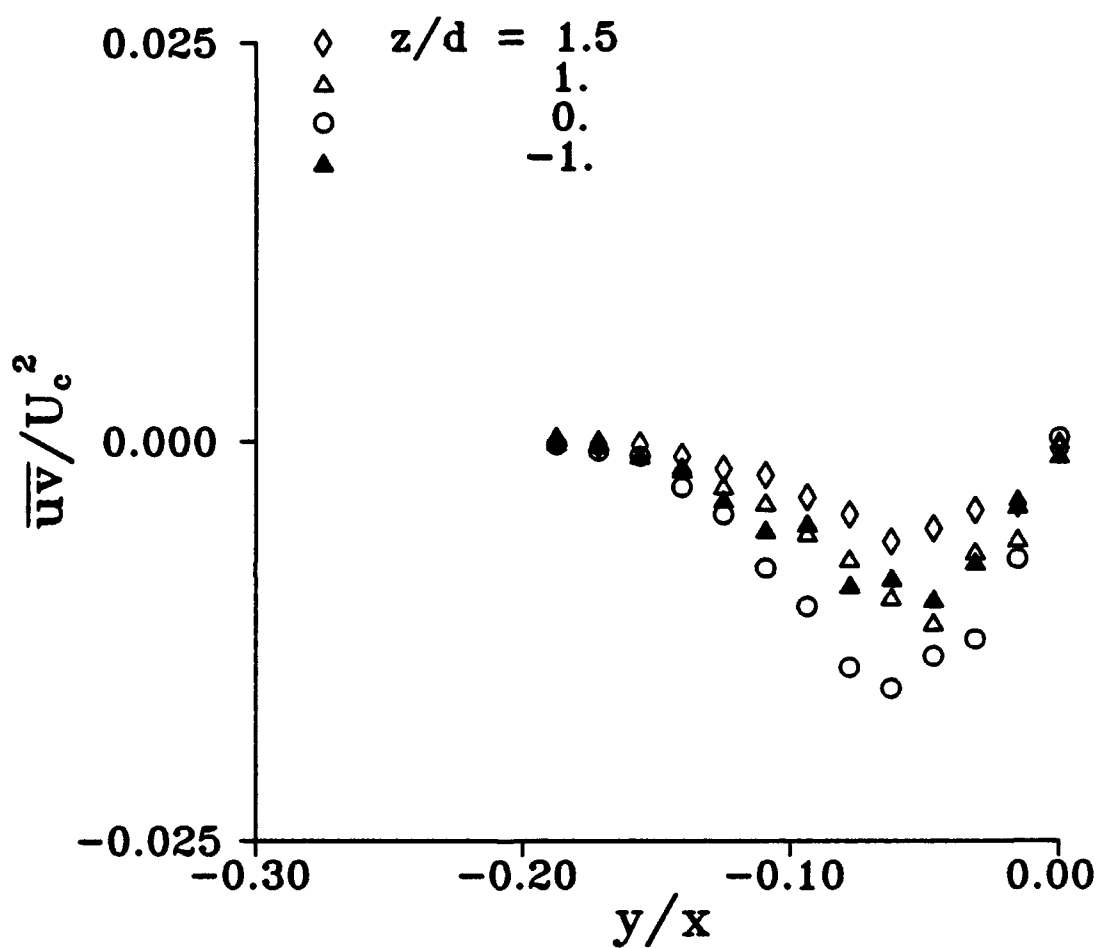


Figure 4.12g. Horizontal profiles of the Reynolds stress \overline{uv}/U_c^2 at $x/d=16$ for the shallow jet, $h/d=2$.

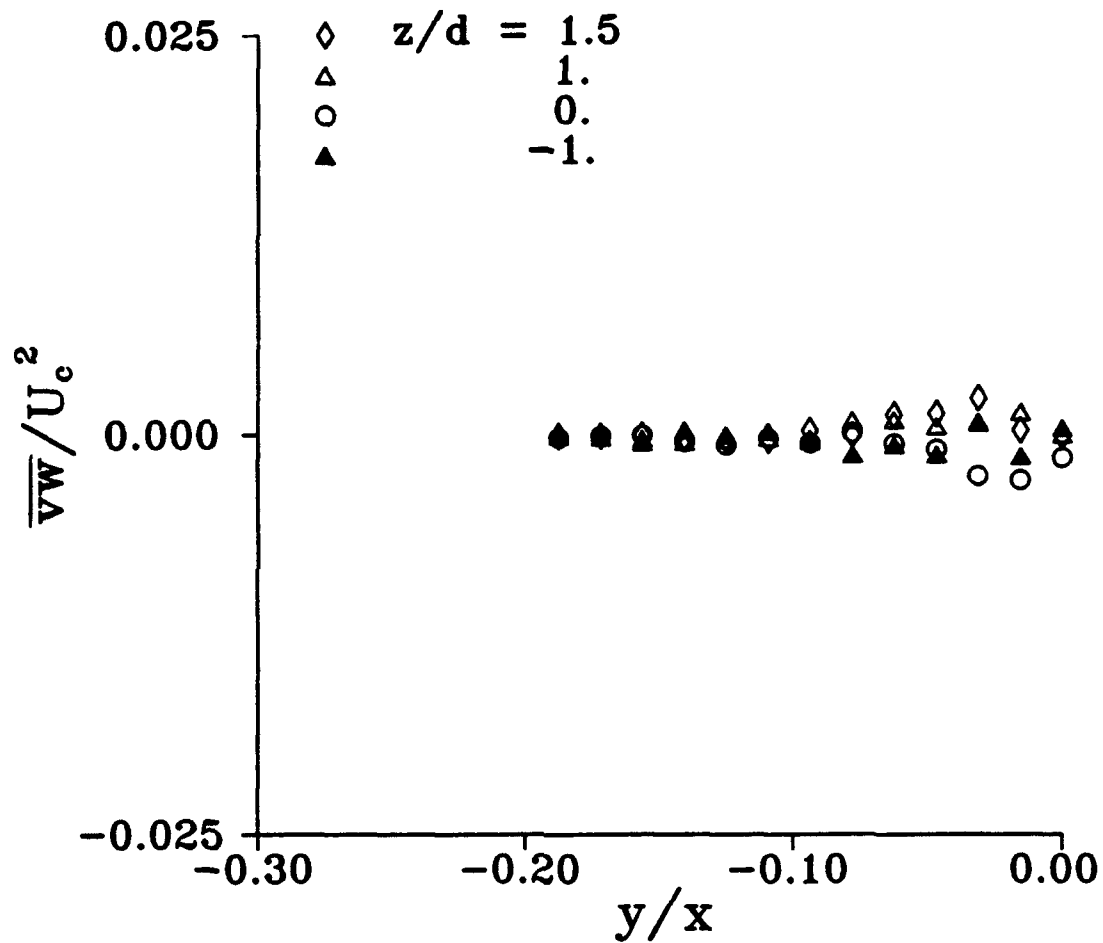


Figure 4.12h. Horizontal profiles of the Reynolds stress \overline{vw}/U_c^2 at $x/d=16$ for the shallow jet, $h/d=2$.

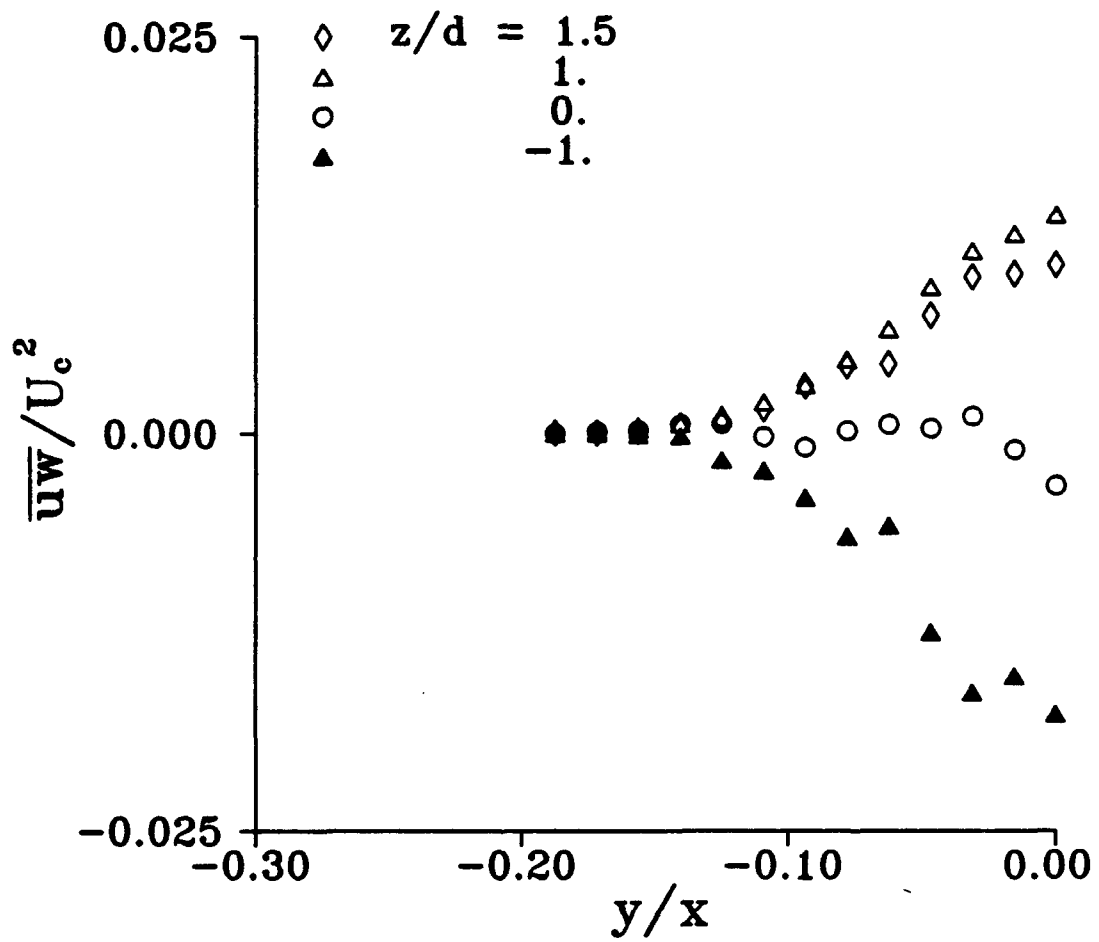


Figure 4.12i. Horizontal profiles of the Reynolds stress $\overline{u'w'}/U_c^2$ at $x/d=16$ for the shallow jet, $h/d=2$.

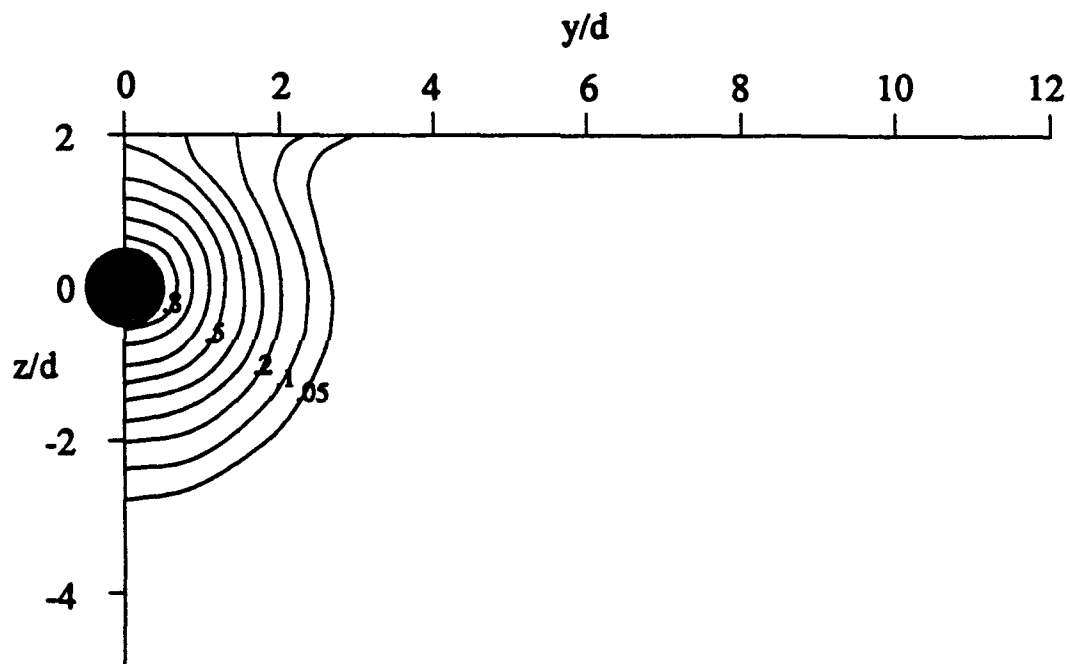


Figure 4.13a. Contours of the streamwise mean velocity U/U_c at $x/d=16$ for the shallow jet, $h/d=2$.

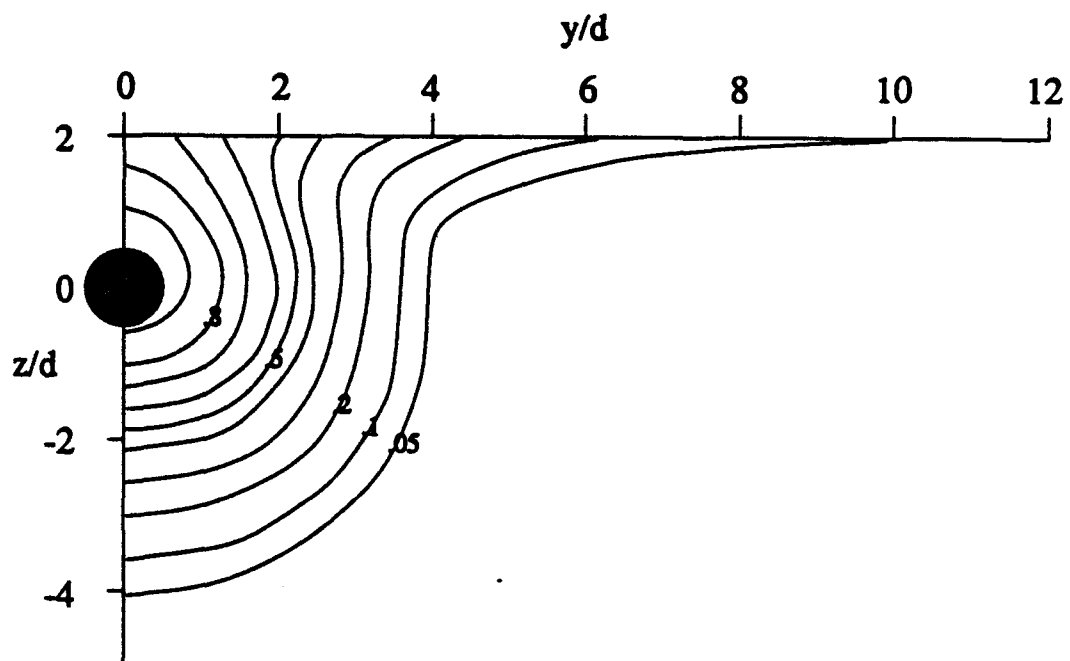


Figure 4.13b. Contours of the streamwise velocity U/U_c at $x/d=24$ for the shallow jet, $h/d=2$.

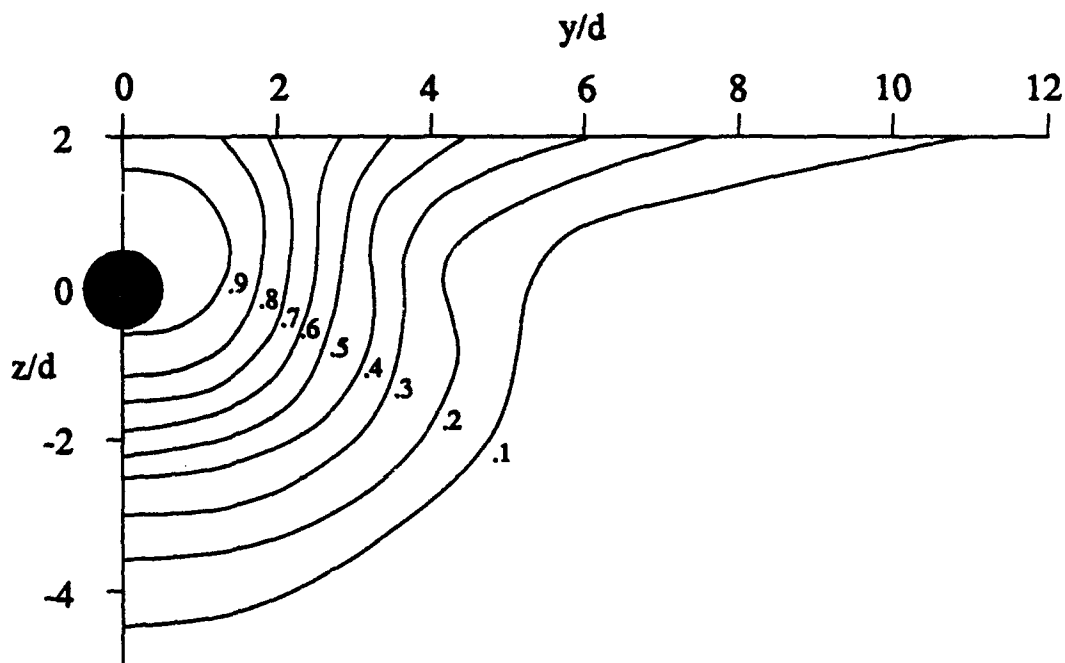


Figure 4.13c. Contours of the streamwise mean velocity U/U_c at $x/d=32$ for the shallow jet, $h/d=2$.

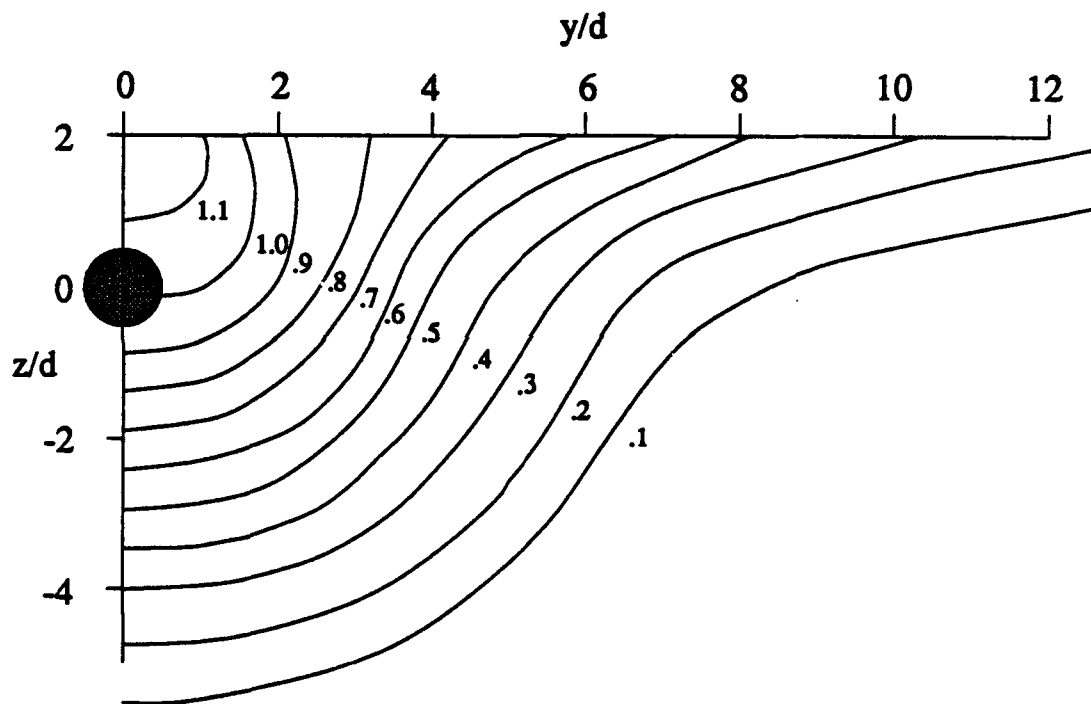


Figure 4.13d. Contours of the streamwise mean velocity U/U_c at $x/d=48$ for the shallow jet, $h/d=2$.

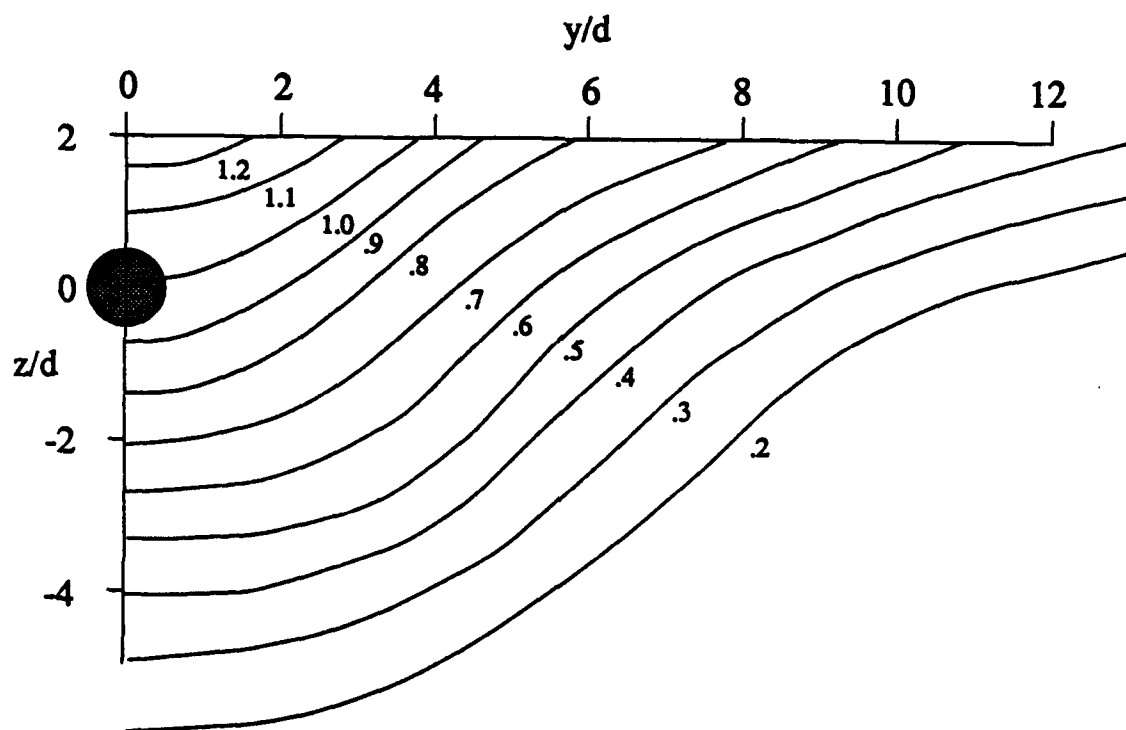


Figure 4.13e. Contours of the streamwise mean velocity U/U_c at $x/d=64$ for the shallow jet, $h/d=2$.

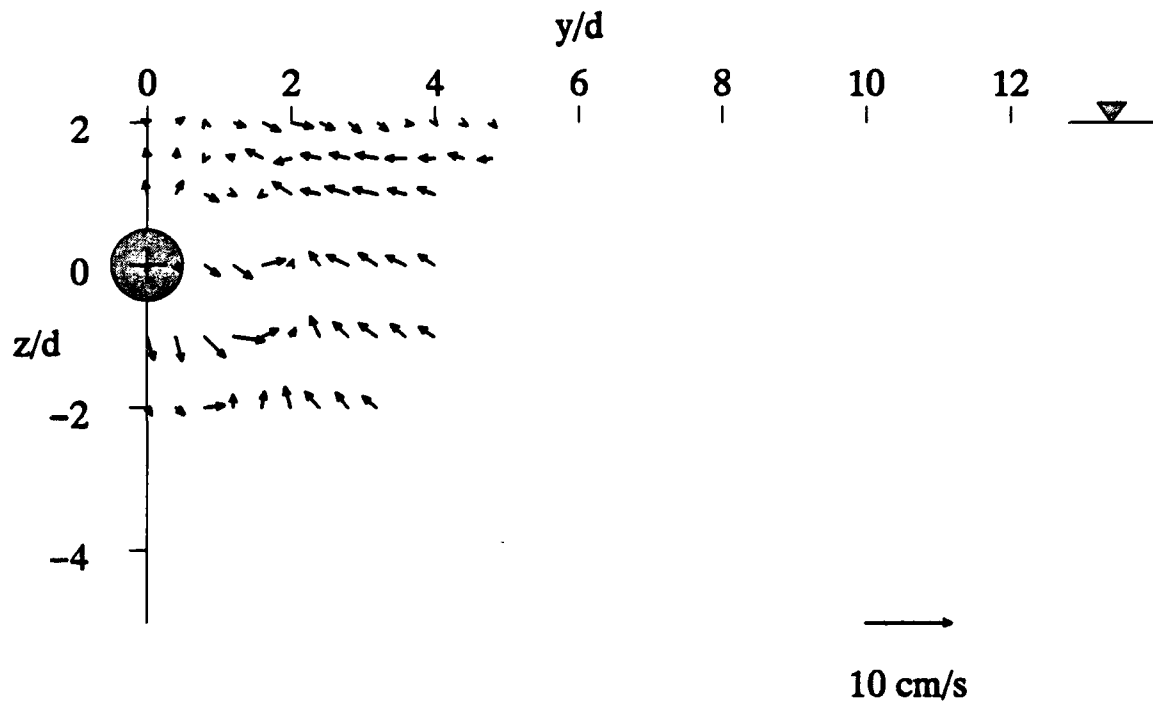


Figure 4.14a. Vector plot of the horizontal and vertical mean velocities at $x/d=16$ for the shallow jet, $h/d=2$.

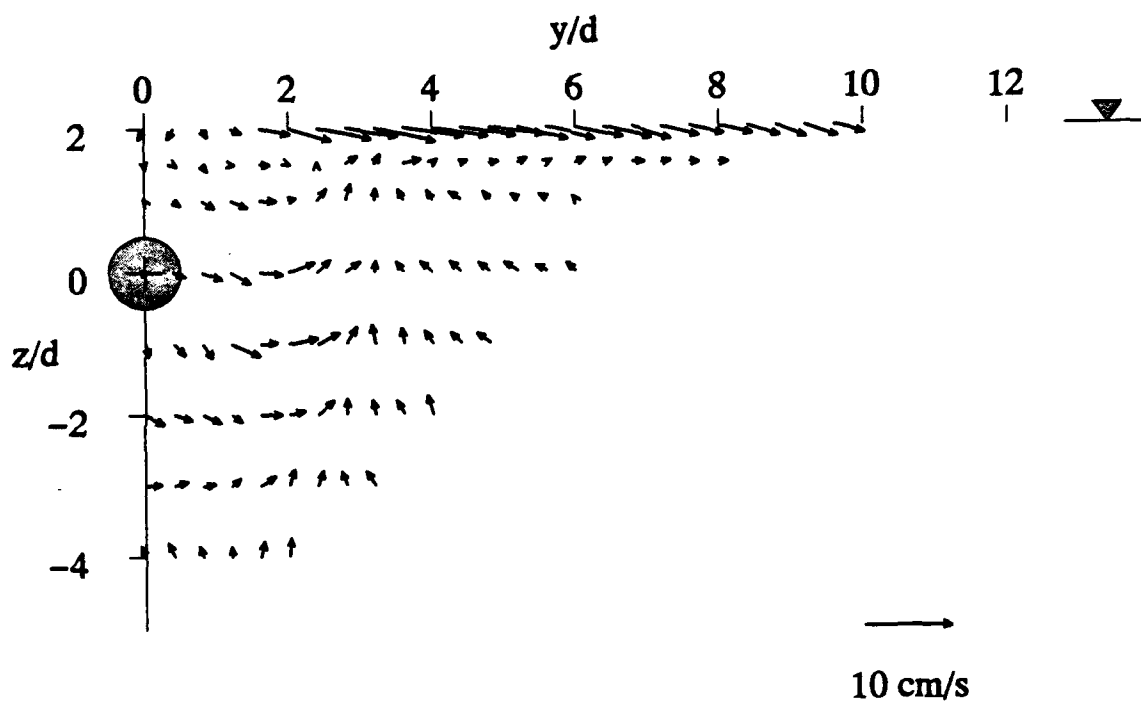


Figure 4.14b. Vector plot of the horizontal and vertical mean velocities at $x/d=24$ for the shallow jet, $h/d=2$.

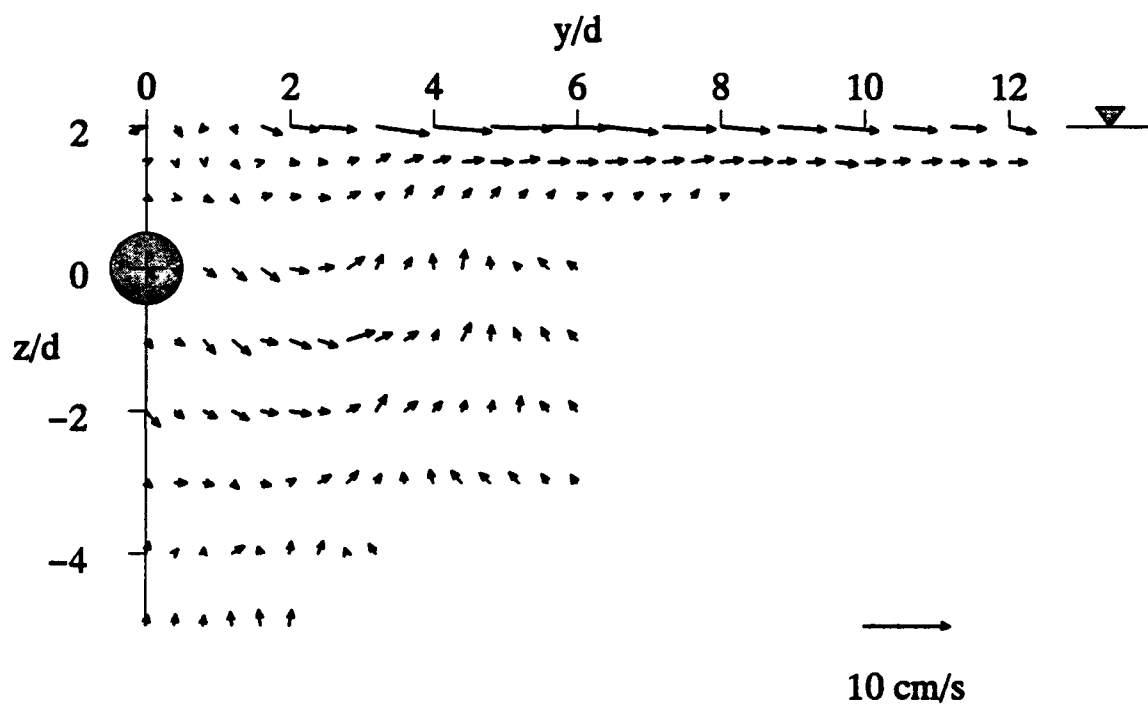


Figure 4.14c. Vector plot of the horizontal and vertical mean velocities at $x/d=32$ for the shallow jet, $h/d=2$.

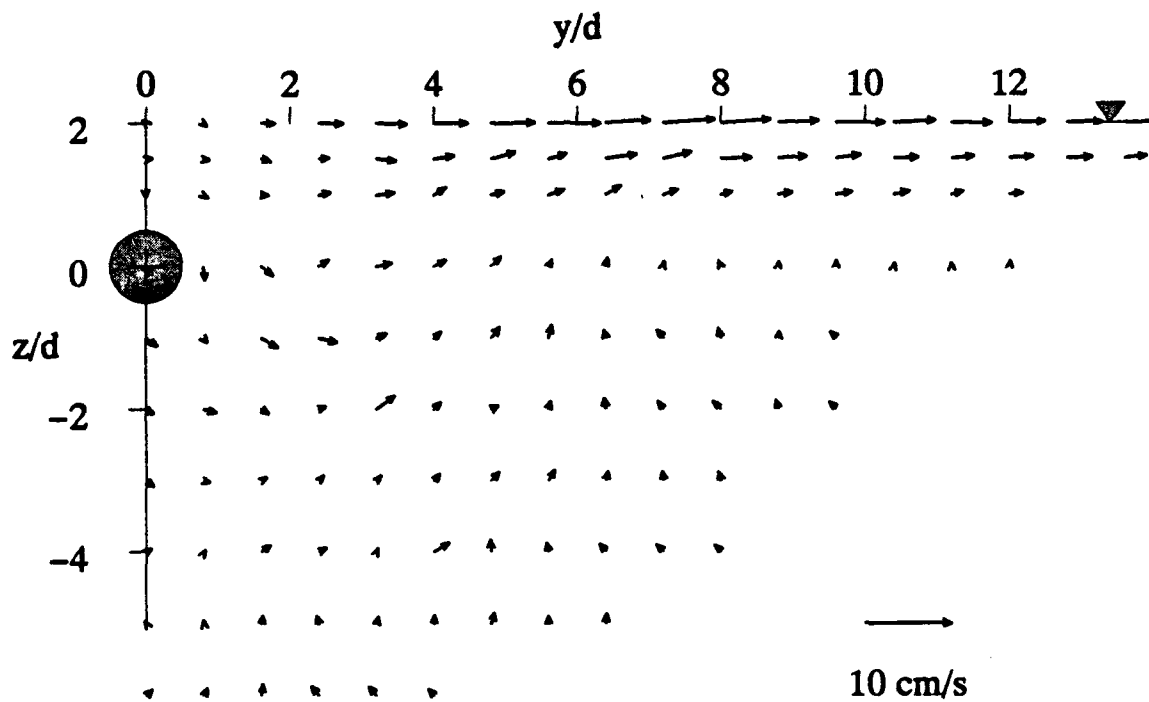


Figure 4.14d. Vector plot of the horizontal and vertical mean velocities at $x/d=48$ for the shallow jet, $h/d=2$.

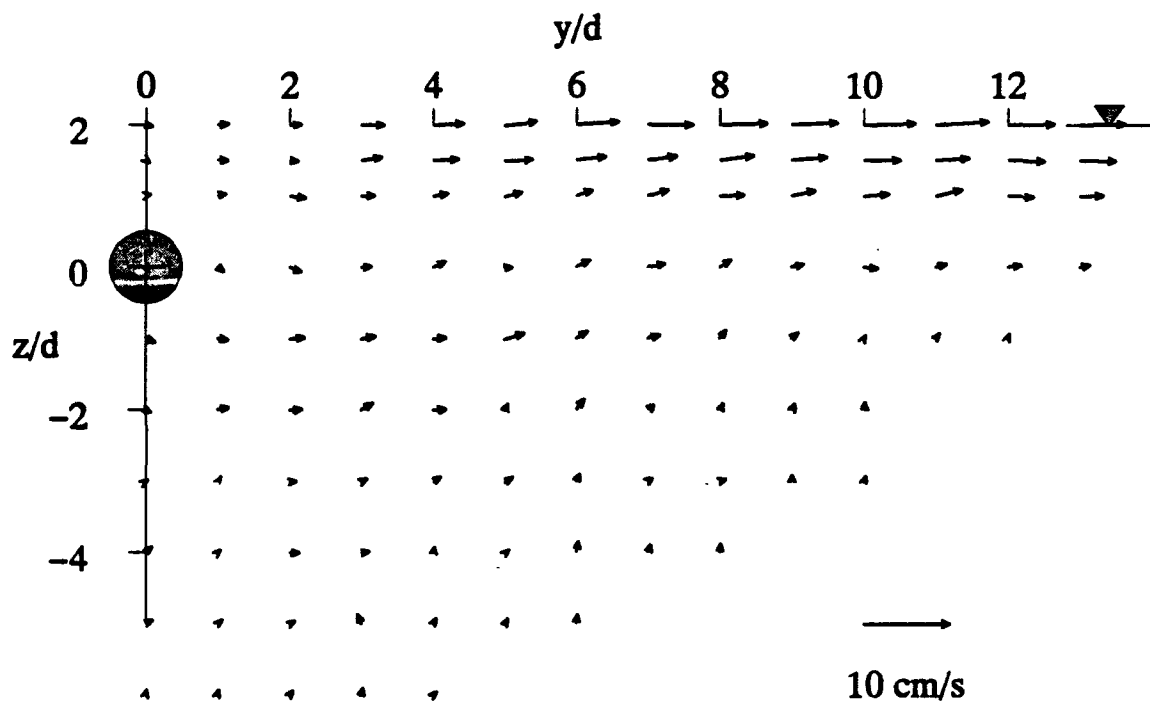


Figure 4.14e. Vector plot of the horizontal and vertical mean velocities at $x/d=64$ for the shallow jet, $h/d=2$.

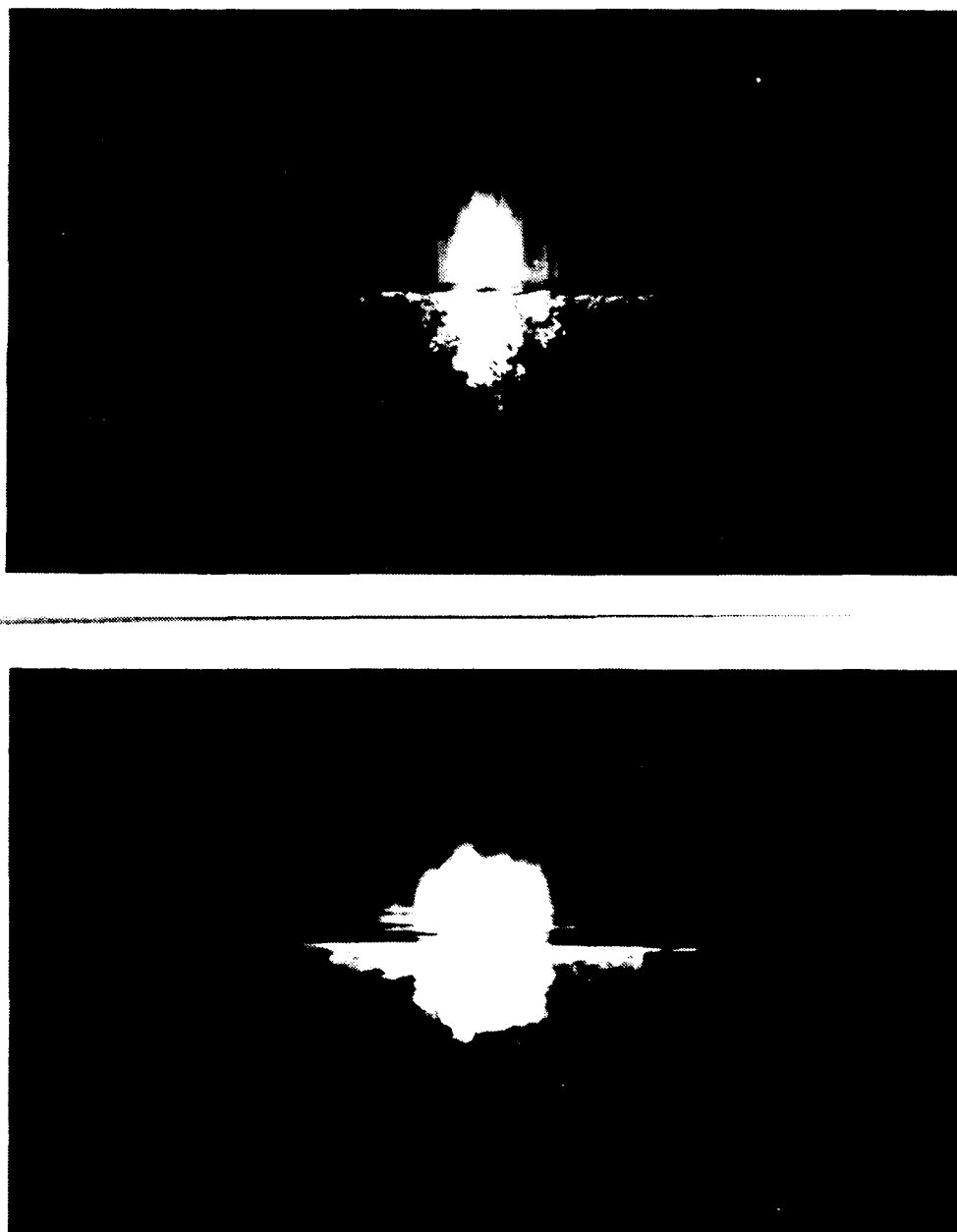


Figure 4.15a. LIF photographs of the shallow jet, $h/d=2$, issuing beneath a clean free surface. The laser light sheet was positioned in a vertical plane at $x/d=32$. Exposure times are $1/125$ s (top) and $1/2$ s (bottom).

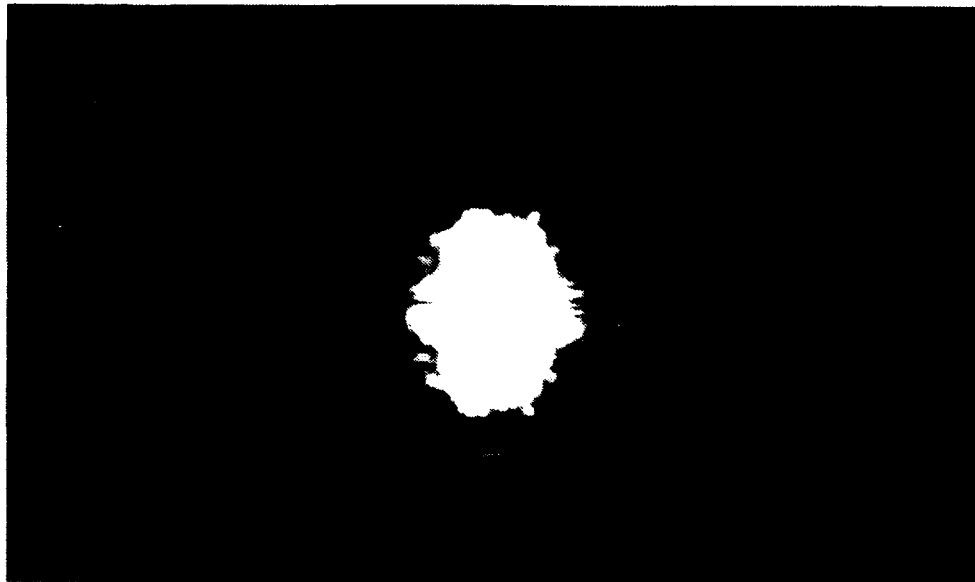


Figure 4.15b. LIF photographs of the shallow jet, $h/d=2$, issuing beneath a free surface contaminated with oleyl alcohol. The laser light sheet was positioned in a vertical plane at $x/d=32$. Exposure times are $1/125$ s (top) and $1/2$ s (bottom).

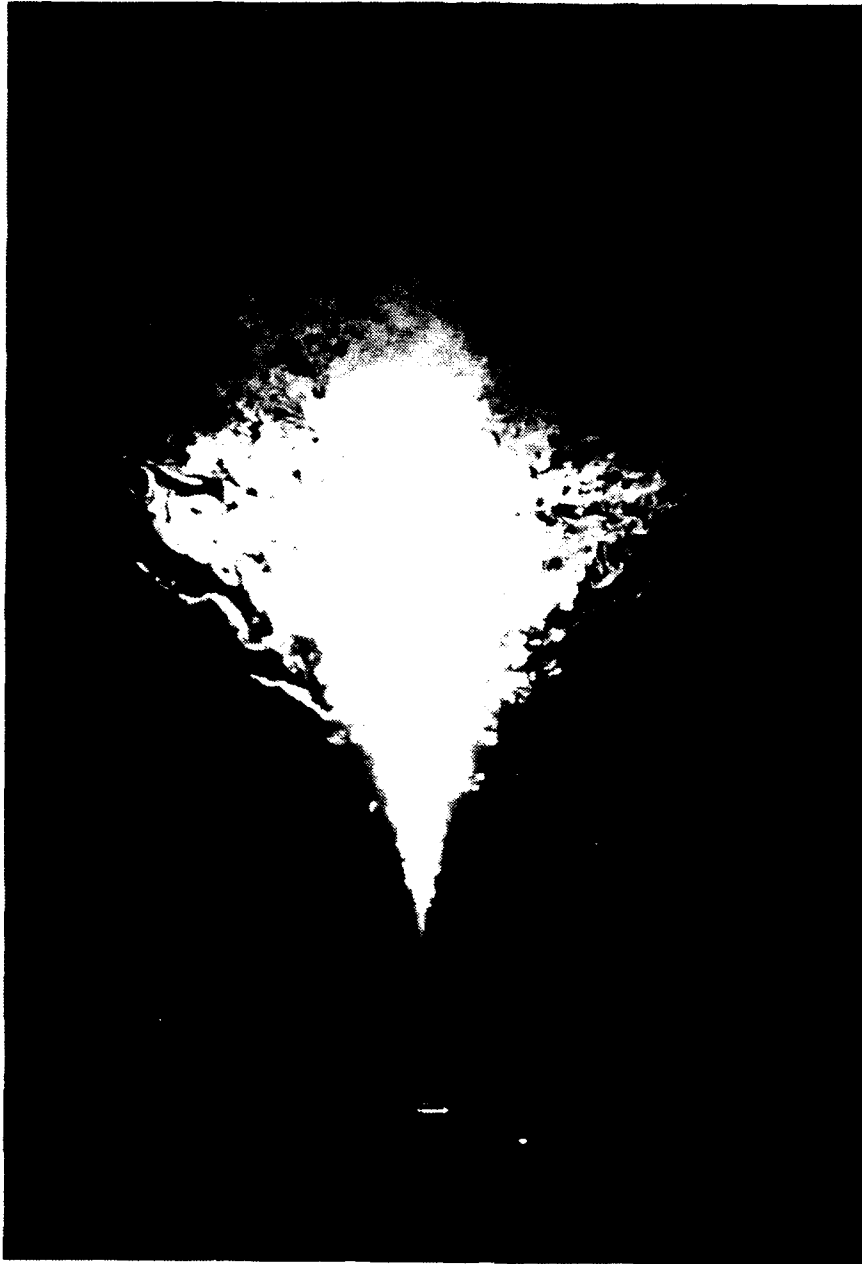


Figure 4.16a. LIF photograph of the surface current produced by the shallow jet, $h/d=2$. The laser light sheet was positioned in a horizontal plane approximately .3 cm below the free surface.



Figure 4.16b. LIF photograph of the surface current produced by the shallow jet, $h/d=2$. The laser light sheet was positioned in a horizontal plane through the jet centerline.

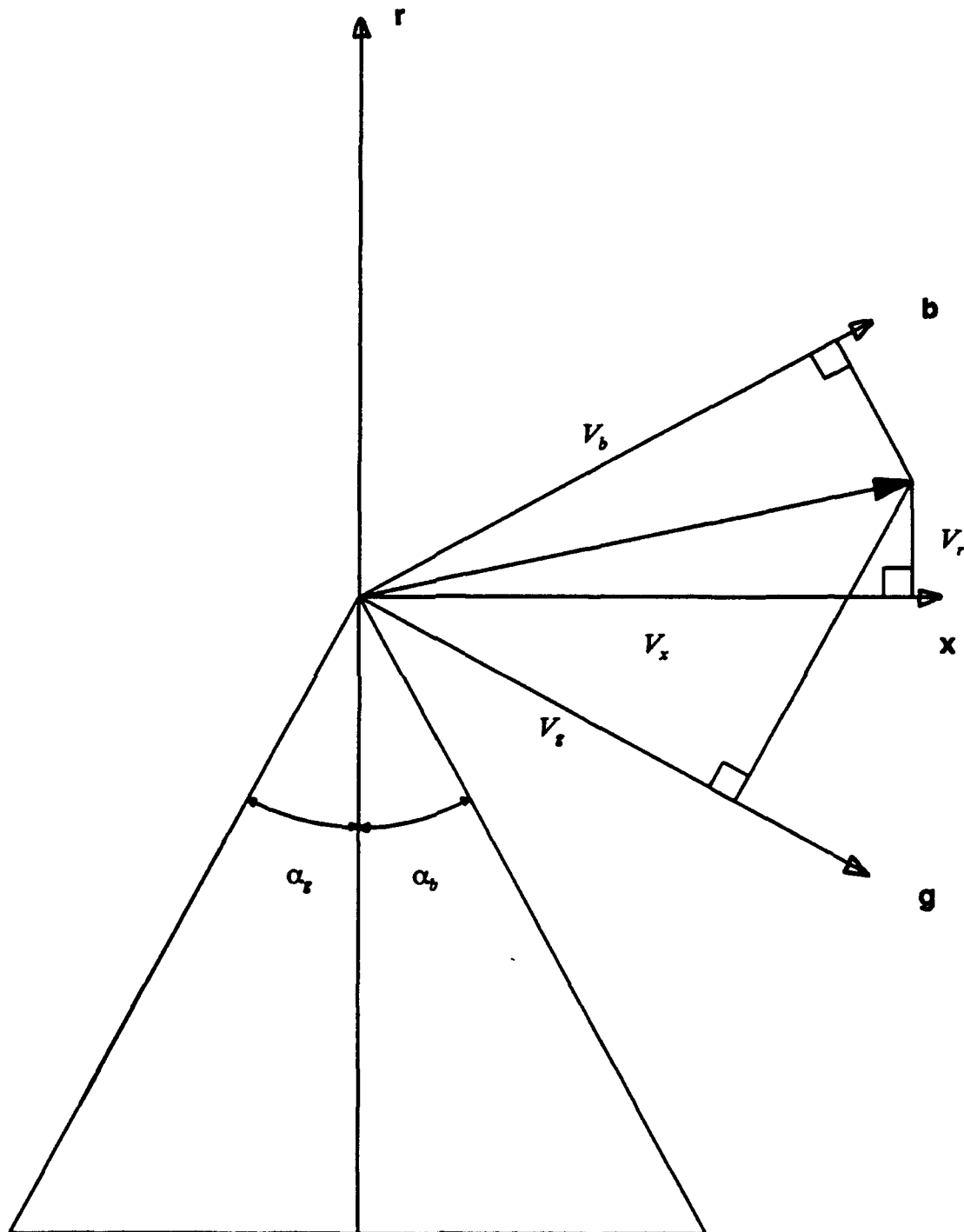


Figure A.1. Sketch showing transformation of velocity components between optical and probe coordinate systems.

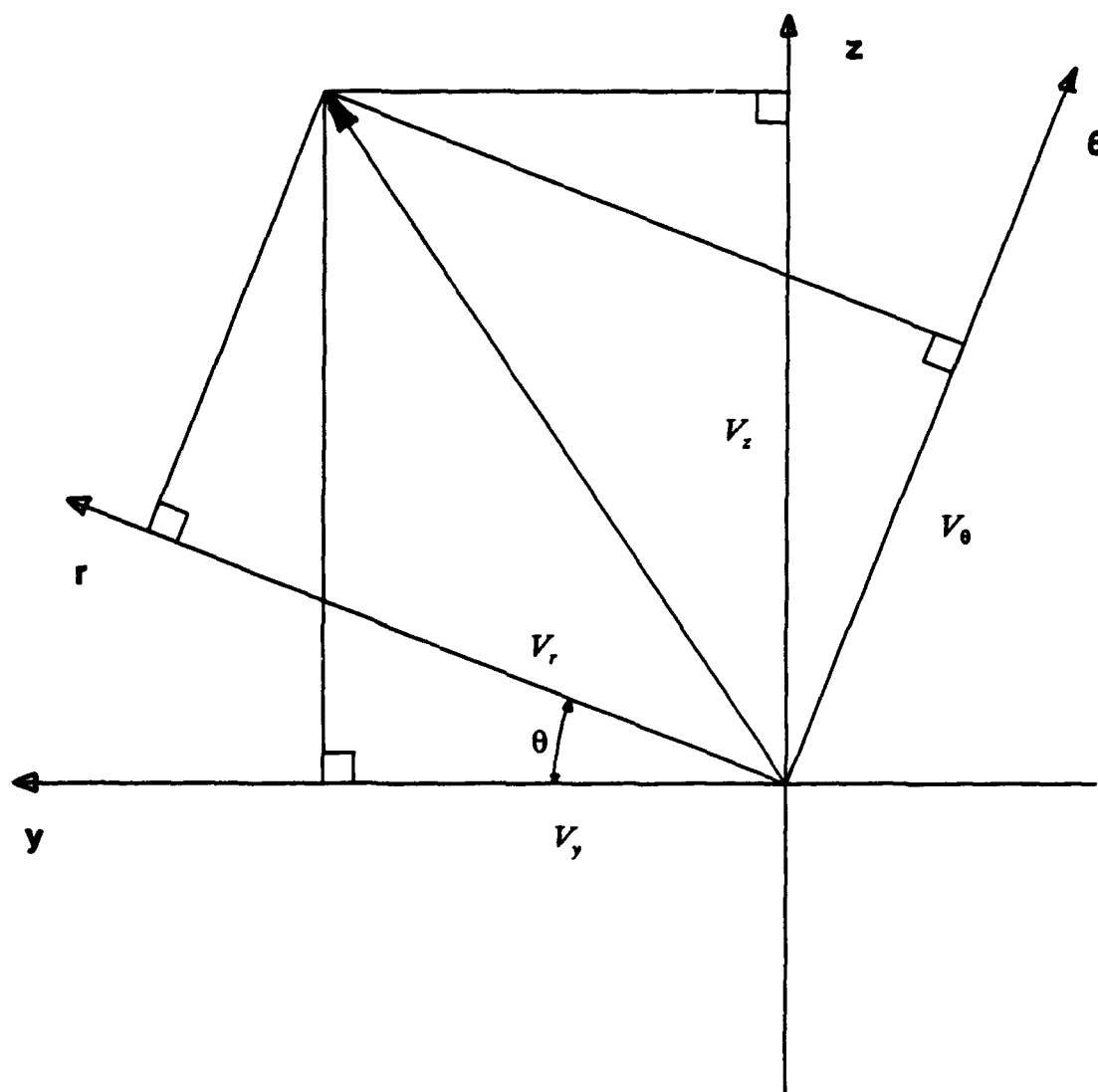


Figure A.2. Sketch showing coordinate rotation between probe and jet coordinate systems.